ADVANCING A SUPERCONDUCTING SAMPLE HOST CAVITY AND ITS APPLICATION FOR STUDYING PROXIMITY-COUPLED NORMAL LAYERS IN STRONG MICROWAVE FIELDS

A Dissertation

Presented to the Faculty of the Graduate School

of Cornell University

in Partial Fulfillment of the Requirements for the Degree of

Doctor of Philosophy

by

Thomas Edward Oseroff

December 2022

ADVANCING A SUPERCONDUCTING SAMPLE HOST CAVITY AND ITS APPLICATION FOR STUDYING PROXIMITY-COUPLED NORMAL LAYERS IN STRONG MICROWAVE FIELDS

Thomas Edward Oseroff, Ph.D.

Cornell University 2022

The study of the interaction of a microwave field with a conventional superconducting surface is a rich topic for both application and science. The basic interaction with a small signal is understood and was quantitatively described decades ago [Mattis and Bardeen, 1958, Abrikosov et al., 1959]. These descriptions rapidly break down in the presence of large amplitude microwave fields. The resulting interaction is difficult to model and depends strongly on the surface features and properties. A variety of behaviors are observed as the field amplitude is increased. The nature of the behavior changes for different materials, surface structures, and frequencies. Theoretical models describing the interaction of a large microwave signal with a superconductor have been proposed, attacking the issue from a variety of perspectives. At this time, no microscopic models exist that are able to even qualitatively explain the variety of behaviors that are observed.

Beyond the scientific intrigue of better-describing the microscopic origin of the various observed behaviors of superconductors in these extreme conditions, there exists practical motivation. Particle accelerators employ resonant cavities with superconducting surfaces as a means of transferring energy to the particles. For this application, the goal is minimizing the dissipation of the microwave energy in the superconducting surface while maximizing the applied surface field.

To engineer increasingly high performance surfaces, it is required to understand what features/properties are desirable or detrimental for obtaining the application goals.

Realizing a large microwave field on a surface is nontrivial. In this work, a driven resonant cavity was used to create the high amplitude fields. This structure was a sample host cavity, designed with an opening such that a flat sample plate could be attached to close the volume. This scheme allows for exposing a detachable flat sample to a large microwave field. It is nontrivial to measure the response of the sample to the microwave field, as it must be decoupled from that of the system as a whole. The method used for this purpose is sensitive to systematic and measurement uncertainty, especially for samples of direct interest for accelerator application. Attempts were made to modify the system to improve its measurement quality and range. The implemented changes led to a significant improvement in performance.

Using this sample host cavity, an attempt was made to improve the understanding of a common feature of superconducting surfaces, the native oxide. Specifically, the surface oxide that is present on the best materials known for accelerator application, niobium and niobium-tin. The niobium oxide contains a metallic phase that electrically couples to the superconducting bulk. This coupling, referred to as proximity-coupling, results in the normal conducting oxide layer taking on some superconducting properties. Conversely, the normal conducting layer will influence the properties of the superconductor near the surface. Models and experiments indicate that this metallic oxide may have an important role in the amplitude-dependence of the microwave dissipation in superconducting cavities used for applications [Eremeev, 2008, Gurevich and Kubo, 2017]. But it is difficult to control the relevant properties of the oxide,

and to do so without altering other surface features. This makes it difficult to study the impact of metallic surface oxide phases on the microwave interaction directly.

In this study, the choice was made to remove the oxide and replace it with an easier-to-control gold layer. This allowed for a more controlled study of the microwave response of a proximity-coupled system. Using the sample host cavity, high-field RF measurements were performed on these gold-superconductor samples for a range of gold layer thicknesses. A model describing the influence of proximity-coupling on the microwave response was implemented to assist with interpreting the measurements. The data was well-described by this model for small amplitude fields, but the agreement was lost as the field strength increased. It was found that replacing the niobium oxide with a minimal thickness gold layer enhanced the maximum field limitations of the system. This result indicates that the niobium oxide could also be a limiting factor in accelerator applications.

BIOGRAPHICAL SKETCH

Thomas Oseroff was born and grew up in Greenville, North Carolina. At this time he was most interested in playing guitar, but decided he lacked the talent to pursue music as a career. Motivated by a combination of curiosity about how electric guitar effects were made and having had relative success in high school mathematics, Thomas chose to go to North Carolina State University to study Electrical Engineering (EE). In his introductory coursework, he grew more excited about Mathematics and Physics, choosing to add both as minor fields of study. In EE he began to specialize in solid state devices and microwave engineering. As his graduation approached, Thomas felt a lack of completeness and understanding, which he attributed to inadequate understanding of the fundamental mathematics and physics that supported these specializations. Supported by his parents, he was able to stay another 1.5 years to complete majors in Physics and Applied Mathematics. Upon completing these degrees, he came to Cornell University to pursue a PhD. There he learned about and developed a passion for superconductors and their application in resonant cavities used in particle accelerators.

To my parents who have encouraged me to follow my dreams and supported me throughout.

ACKNOWLEDGEMENTS

lanjan, Gabriel, and Patrick for their help and teachings during my course-work and their continued willingness to discuss my questions and help me to this day. I want to thank Thy for everything.

TABLE OF CONTENTS

LIST OF TABLES

LIST OF FIGURES

CHAPTER 1

INTRODUCTION

Microwave applications have a long history of confusing, fascinating, and almost magical behaviors. That such a heavily studied field continues to display surprising behavior is a testament to the depth it contains. Sometimes observed phenomena are easy to explain and understand. Other times, it is virtually impossible. Fundamentally, the behavior of microwave radiation is simple to explain. Fields, obeying Maxwell's equations, propagate through vacuum and interact with their surroundings. This interaction with materials and structures is the origin of the exciting effects routinely used and discovered by using microwave devices.

The interaction of electromagnetic radiation with media varies drastically for different types of materials. In general, it is characterized by changes in the phase difference between the propagating electric and magnetic field, and attenuation of their amplitude corresponding to dissipation of the wave energy in the material. In insulating materials, the interaction with the field occurs through the polarization of constituent atoms and molecules. In conducting materials, the attenuation happens entirely in the material surface where the propagating fields induce currents that serve to screen the radiation from entering further into the material. In practice, conducting surfaces will possess complications, such as defects, impurities, or structures. The range of behaviors observed in the presence of these complications delivers extensive potential for industrial and scientific application, if they can be controlled. In this work, the primary interest will be on surfaces dominated by a superconducting response.

Independently from their microwave response, superconductors are a topic

with incredible depth and nuance. Characterized by the ability to transport charge in DC with zero dissipation and the complete expulsion of magnetic flux from their interior, they have been a topic that has fascinated scientists and captured interest for application for a century. These properties cannot be explained by classical physics, requiring quantum mechanics to adequately capture their observed behaviors. In the presence of a microwave field, the superconducting response is analogous to that of a normal conductor. In general, the dissipation and the extent of field penetration towards the material bulk are reduced when compared to the normal conducting case. While the physical mechanisms behind the superconducting response are distinct from those of the normal conductor, the qualitative behavior is similar.

To demonstrate the behaviors that arise when a superconductor interacts with a microwave field, consider the effect of field amplitude at the superconducting surface. The quantitative description of the interaction with a minimal amplitude microwave, while requiring numerical calculation, is a straightforward problem that has been solved decades ago [Mattis and Bardeen, 1958, Abrikosov et al., 1959, Nam, 1967a].

At low but nontrivial field strengths, some of the fascinating behaviors of the superconducting response become evident. Specifically, it is observed that superconductors illuminated by small amounts of microwave radiation can display enhanced superconducting properties [Tinkham, 2004]. This effect is reported for microwave radiation with a sufficiently high frequency, less than but approaching the superconducting energy gap. While surprising, the effect does have a straightforward explanation and detailed quantitative solutions have been published [Chang and Scalapino, 1978]. Qualitatively, the effect originates

from a redistribution of quasiparticle excitations to higher energy states. This redistribution allows for the electron pairing interaction to spread to the vacated lower energy states, which decreases the energy of the ground state even further below the Fermi energy [Mangin and Kahn, 2016]. This pairing interaction is the mechanism that gives rise to conventional superconductivity, so the presence of the microwave field effectively strengthens the superconducting behaviors. Even at low fields, it is evident that the microwave interaction with a superconductor can substantially influence the properties and behavior of the superconductor.

Increasing the field amplitude will further complicate the situation. The properties of the system can be influenced by the Cooper pair breaking effects of the increasingly energetic screening currents. In certain materials, this may lead to nonequilibrium states analogous to those that gave rise to the enhanced superconductivity reported at lower amplitude fields and higher frequencies. Naively this may lead one to believe that a similar enhancement could be observed. In practice, such a situation is obscured. As the field is increased, so too will spurious contributions to the system response. In multicrystaline materials, the boundaries between differently oriented grains can act as Josephson junctions, which exhibit separate behavior from the bulk material. Flux vortices that remain in the material due to defects will oscillate in the RF field and can become a dominant contribution at high enough field strengths. Any source of extra heating can cause local temperature rises changing the properties of the system. While this list is not exhaustive, it should be clear that increasing the field strength can cause extra contributions to the response of the material. In many cases, these effects lead to an increase in dissipated electromagnetic energy with respect to field amplitude. Attempts to limit and control these spu-

rious effects contain many scientific and technological problems.

Practically, the field amplitude can be increased until a quench event, defined as the point where the superconductor can no longer retain its superconducting properties and transitions into a normal conducting phase. Identifying the exact mechanism producing the quench event on a given surface and attempting to grow materials or structures that can support higher surface fields are both interesting topics with a wealth of scientific problems and technological interest.

In some cases, the dissipation of electromagnetic energy in the superconducting surface in the high-field range has been observed to decrease as the field amplitude increases [Grassellino et al., 2013, Hein, 1999]. This technologically and scientifically exciting exception to the increased dissipation observed when increasing the field amplitude raises many questions. What exactly is the mechanism of its origin? Is it related to the low-field and high-frequency enhancement of superconductivity? Can the material properties or surface features be engineered to yield further reductions of dissipation? To date, attempts to explain this high-field effect have been unable to account for the observed dependencies on frequency, material properties, and temperature. Without an adequate explanation, this phenomena remains an intriguing scientific and technological mystery.

Numerous applications for microwave superconducting devices exist or are being actively pursued [Anlage, 2021]. For low-field applications, notable work is being done on superconducting qubits coupled to superconducting resonators and their peripheral control/readout circuitry. Low-field devices are also employed as various types of detectors. Attempts have been made to uti-

lize superconducting properties combined with specialized structures to construct a variety of metamaterials [Anlage, 2010]. The only high-field application the author is aware of is resonant cavities in particle accelerators, which is the targeted application of this work.

In modern particle accelerators, charged particle beams are accelerated by passing them through a series of resonant cavities [Padamsee et al., 2008]. Accelerating cavities have been constructed with both normal conducting and superconducting surfaces. In general, a larger amplitude field can be supported on the normal conducting variety as their limitation is a physical breakdown as opposed to the loss of the superconducting phase. To avoid thermal breakdown of the normal conductor, the RF power must be pulsed, which limits the particle beam accordingly. Superconducting surfaces, on the other hand, can support significant amplitude RF fields in continuous wave operation. They must be kept at cryogenic temperatures for the superconducting state to exist, which includes substantial refrigeration costs. In general, the superconducting case results in a net improvement for operational costs. The technological goals for accelerator cavities with superconducting surfaces are to minimize dissipation and to maximize the amplitude of the RF field that it can support with relatively low dissipation.

Tremendous progress has been made towards accelerator application goals [Padamsee, 2017]. Specifically, the microwave field strength limitations in modern cavities have been substantially increased due to advancements in material processing, surface treatments, and cavity geometries. A side effect of this success is the ability to use these superconducting cavities to directly study the behavior of a quantum system in extreme conditions. As discussed earlier, the

interaction between a strong microwave and a superconductor is a rich topic with much to explore. The unique physical situation present in these cavities offers a venue for simultaneously advancing technology and science.

In this work, a sample host cavity that exposes a detachable sample to large microwave fields was utilized. The detachable sample, which has a flat surface, enables a relatively efficient and cost-effective means to explore a range of materials and structures for accelerator applications. The goal was to explore the physics of the high-field microwave-superconductor interaction in a way that was technologically useful. At the onset of the project, the inherited sample host cavity had significant issues and limitations. In chapter 4, the sample host cavity design is described, its limitations are quantified, and the systematic upgrades that were implemented in an attempt to make it into a more suitable measurement system are presented. The improvements to the system improved its reliability and measurement range significantly, but the methods employed to extract sample information are not ideal for accelerator goals. At best, careful measurements can only be carried out on samples that display high amounts of electromagnetic dissipation as compared to the standard cavity surfaces.

Accepting that the sample host cavity that was inherited for this project had limited utility for directly probing materials and structures of interest for accelerator goals, it was required to identify samples that would be acceptable for study with this system while still being scientifically and technologically relevant. It was decided to study the behavior of a thin normal conducting film deposited over a bulk superconducting substrate. Details of this study are presented in chapter 5. This structure exhibits an effect referred to as proximity coupling, where the normal conductor inherits some superconducting behav-

iors. To the author's knowledge, this study is the first to probe a proximity-coupled normal layer subjected to strong RF fields.

Examining the behavior of these systems in a strong RF field is of interest from a scientific perspective, but it also has overlap with accelerator goals. The most successful superconducting materials for accelerator applications are niobium and niobium-tin [Padamsee, 2017]. Both are thought to have a partially metallic surface oxide with normal conducting properties. The effects of this oxide on cavity goals are not precisely understood. Experiments have been carried out attempting to study this, but the complexity of the oxide structure and the difficulty of manipulating its properties in a controlled manner lead to data that is challenging to interpret. In the study discussed in chapter 5, the oxide layer is replaced with a more easily controlled normal conductor. By studying the behavior of this new sample and varying normal conductor properties, it is hoped that conclusions can be drawn about the relevance of this metallic oxide phase for accelerator application.

The results of the study were not expected. The RF field amplitude dependence of the proximity coupled layer did not follow the predictions of models that were considered. It is not clear where the discrepancy originates. In chapter 5, a detailed consideration from the experimental perspective is presented. A key result of the study was an apparent enhancement of the quench field when the native oxide of the superconductor was replaced with the thinnest normal conductor examined. While this result has yet to be reproduced, it indicates that the oxide may be playing a role in limiting the maximum microwave field amplitude that can be supported in a superconducting resonator.

CHAPTER 2

RESONANT CAVITIES AND THEIR OPERATION

The primary purpose of this text is to detail the development and results of an apparatus used to expose a superconducting sample to strong microwave fields and extract relevant information about the resulting electrodynamics of the sample. More specifically, this apparatus is a superconducting resonant cavity. In the present chapter the relevant concepts are introduced. Specifically, resonance, electromagnetic cavities, and what is required to use a superconducting cavity for the purpose of material characterization.

This chapter is not intended to be a general introduction to resonant cavities, many already exist [Pozar, 1990, Jackson, 2012], but is intended to present what is necessary for the design and operation of superconducting resonant cavities at microwave frequencies. The aim is to collect relevant information into a single chapter that imparts intuitive understanding of specific concepts upon the reader, while introducing all terminology and concepts required to comprehend the topics in the coming chapters. Cavities with superconducting interiors will possess enormous quality factors that create unique challenges for the design of peripheral systems, the design of the cavity, and its operation. As such, the discussion aims to illuminate these specific problems and provides supplementary utility to the more general introduction of similar topics given elsewhere.

First, the concept of a resonant system will be developed and its properties introduced. This is required to motivate why a cavity, a vacuum or dielectric-filled volume surrounded by a conducting barrier, acts as a resonant system. The general properties of a resonator will later be connected with the techniques used to operate, design, and extract meaning from high quality factor resonant

cavities. Second, a precise definition of resonant cavities, including explicit an-
alytical descriptions of a relevant type of resonant cavity, is presented. The dis-
cussion begins by examining an ideal situation with perfect conducting walls.
The required concepts to extend this definition to a more practical case, and
the metrics used in the design and analysis of resonant cavities in practice are
considered. A circuit model picture of a resonant cavity is justified and used to
describe the physical connection of the resonant cavity with external systems.
Third, the details of operating a high quality factor microwave cavity and mea-
suring interesting material properties are considered.

2.1   Damped Resonator with a Sinusoidal Driving Force

A resonant system is one that periodically transfers its energy from one form to
another in such a way that the energy exchange is most pronounced at a spe-
cific frequency. For example, a pendulum is a resonant system where potential
energy is converted to kinetic energy as the mass falls with gravity before being
converted back to potential energy as it swings back against gravity on the other
side of its cycle. Mathematically this is described with a differential equation

$$\ddot{x}(t) + B\dot{x}(t) + Cx(t) = F(x, t) \tag{2.1}$$

Where x is a general coordinate describing the system, B corresponds to a damp-
ing force removing energy from the system, C describes the nature of the energy
exchange, and $F(x, t)$ is an externally applied force driving the resonant sys-
tem. This section serves to motivate the description of the resonant cavities uti-
lized in this text which will be driven exclusively by a sinusoidal force. Hence
$F(x, t) = D\cos(\omega t)$, where D conveys the strength of the driving force and ω is its
angular frequency.

The solution describing the evolution of general coordinate, x, in time, t, is given by the sum of the homogeneous solution, x_h, and the particular solution, x_p. The homogeneous solution describes the response of the undriven system and can be expressed as

$$x_h(t) = e^{-\frac{B}{2}t}\left(\alpha_1 e^{i\omega_R t} + \alpha_2 e^{-i\omega_R t}\right) \tag{2.2}$$

Where $\omega_R = \sqrt{C - \left(\frac{B}{2}\right)^2}$ and α_1 and α_2 are coefficients determined by conditions that must be specified. As time increases from an arbitrarily defined zero the homogeneous solution is damped according to the factor $e^{-\frac{B}{2}t}$ that describes energy being removed from the system. For a nonzero driving force, energy can be put back into the system to offset this loss. This is described by the particular solution (for the previously specified drive force $F(x,t) = D\cos(\omega t)$):

$$x_p(t) = A\cos(\omega t - \phi) \tag{2.3}$$

With amplitude

$$A = \frac{D}{\sqrt{\left(C - \omega^2\right)^2 + (\omega B)^2}}$$

and phase

$$\phi = \tan^{-1}\left(\frac{\omega B}{C - \omega^2}\right)$$

The primary case of interest in this text is the steady state where $t \to \infty$. Here the homogeneous solution will be damped to zero and the particular solution will completely describe the behavior of the system. The amplitude and phase of equation 2.3 depend on frequency as shown in figure 2.1. The amplitude of the general coordinate oscillation under sinusoidal drive is maximized at the previously defined frequency, $\omega_R = \sqrt{C - \left(\frac{B}{2}\right)^2}$. The phase at this frequency is exactly $\pi/2$.

The quality factor is perhaps the most important metric for a resonator. It is defined as the energy stored in the resonator in steady state divided by the
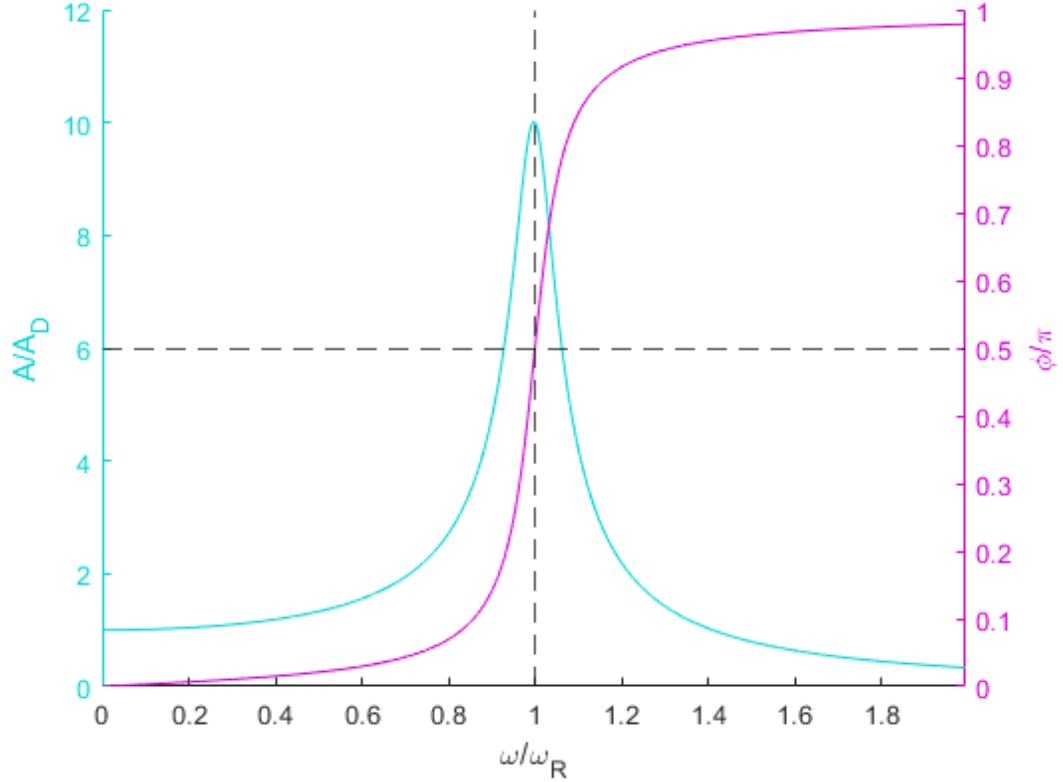
Figure 2.1: Steady state amplitude and phase of the resonant system described by equation 2.3. The amplitude and phase at the resonant frequency are signified by the dashed black lines.

energy lost per radian. Let the steady state energy stored in a closed resonator be denoted as U. The dissipated power can then be defined as $P = -\frac{dU}{dt}$. At the resonant frequency the energy lost per radian will be P/ω_R. Therefore, the quality factor is expressed as

$$Q \equiv \frac{\omega_R U}{P} \tag{2.4}$$

The choice to define this important quantity in terms of stored energy and dissipation is to better connect with readily measured quantities, as in practice the exact nature of the resonator differential equation could vary from equation 2.1.

While stored and dissipated energy are experimentally useful, it can be instructive and useful to express the quality factor in terms of the parameters of

11

equation 2.1. The amplitude of the general variable used to describe the resonator when no driving force is applied decays with characteristic time $\tau_x = 2/B$ according to equation 2.2. In general, the energy stored in a resonator obeying equation 2.1 will be proportional to the square of x. Therefore, the decay of the energy in a damped resonator will be governed by the characteristic time $\tau_U = 1/B$. The power loss of this damping can be expressed in terms of the energy: $P = -\frac{dU}{dt} = \frac{U}{\tau_U}$. Plugging this into the above definition of Q gives an equation determined entirely by the parameters of equation 2.1

$$Q = \omega_R \tau_U \approx \frac{\sqrt{C}}{B}$$

Where the approximation, following from $\omega_R = \sqrt{C - \left(\frac{B}{2}\right)^2} \approx \sqrt{C}$, assumes a lightly damped resonator. This is often the case in practice and is very much true for the entirety of the work considered later in this text. Restricting the discussion to resonators with high quality factors allows for expressing the quality factor in a form that depends on the shape of the resonance peak in figure 2.1. Specifically, on the square of this amplitude to connect with the more readily observed stored energy or power dissipation. It is straightforward to demonstrate or derive that the shape of the amplitude (and therefore energy) in figure 2.1 will change with quality factor. Specifically, as quality factor increases the height of the amplitude at resonance will increase while the width of the peak will decrease. This behavior is captured in the expression that can be derived from the amplitude of equation 2.3 assuming the high quality factor limit where the resonance peak becomes narrow.

$$Q = \frac{\omega_R}{\Delta\omega}$$

Where $\Delta\omega$ is the full width at half max of the square of the peak in figure 2.1. This form provides a different perspective on the role of the quality factor and

12

can be useful for its measurement and better understanding the behavior of a system.

The concepts developed in this section regarding the quality factor and the behaviors of resonant systems will be used throughout the remainder of the text.

2.2   Radio frequency resonant cavities

While the general description of a resonator applies to many systems, the focus of this work is on electromagnetic resonant cavities operated at radio frequencies. These are structures with a cavity region in which specific configurations of electromagnetic fields at certain frequencies can exist. The geometry of the cavity is arbitrary and can be occupied by either a vacuum or a dielectric material. A cavity consisting of a vacuum must be bounded by a conducting material. If the cavity consists of a dielectric material, then it can either bounded with a conductor or with a material with a (very) different dielectric constant.

The frequencies that support specific electromagnetic field configurations are referred to as resonant frequencies. To justify this notation, it is more efficient to view the situation qualitatively rather than attempting the complicated task of reducing the solution of Maxwell's equations to a form that resembles equation 2.1 [Liepe, 2001]. Ignoring the cavity boundary, electromagnetic radiation will propagate through the dielectric or vacuum media of the cavity according to Maxwell's equations. In the unbounded scenario without dispersion the strength of this propagation does not depend on a specific resonant frequency. When the boundaries are introduced, the electromagnetic fields will

now reflect from these surfaces. At specific frequencies the resulting reflections will interfere constructively resulting in an enhanced magnitude beyond what is possible for the individual traveling waves. That is, for specific frequencies of electromagnetic radiation in an enclosed cavity with reflecting surfaces, specific electromagnetic fields will result from constructive interference that will amplify the amplitude of the fields. The standing waves set up from the constructive interference will exchange energy between the electric and magnetic fields, reminiscent of the energy exchange in a resonant system described in section 2.1. The electromagnetic cavity behaviors qualitatively match with the verbal definition of a resonant system.
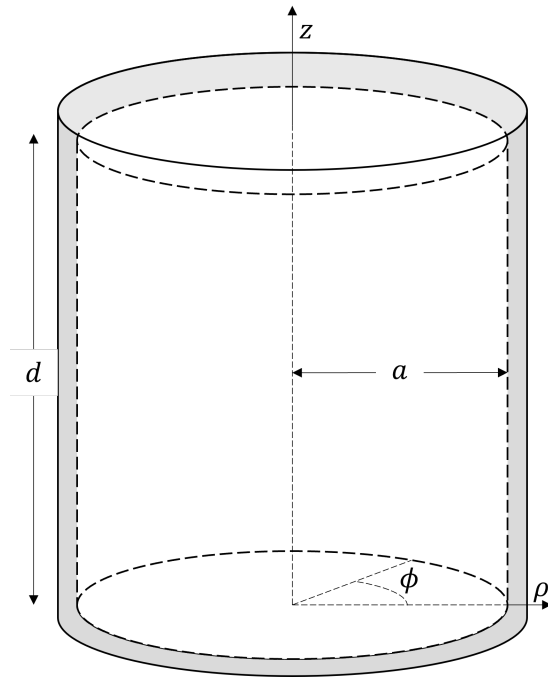
Figure 2.2: Geometry of a cylindrical cavity with definitions of coordinates and dimensions. This cavity and all those considered throughout this text will have metallic walls surrounding a vacuum region.

This section will list and develop the features of these systems that are relevant for the coming discussions. As such it focuses on an extremely narrow subset of the topic. For more complete and coherent discussions the reader should

turn to the many established resources [Jackson, 2012, Pozar, 1990]. Specifically, the focus will now be restricted to a vacuum-filled cylindrical cavity with radius a and height d pictured in figure 2.2. The resonant electromagnetic configurations of a cylindrical cavity can fall under two categories organized by restriction of the fields oriented along the axis of the cylinder. The first category, transverse electric (TE), is characterized with $H_z \neq 0$ and $E_z = 0$. The second, transverse magnetic (TM), is characterized with $H_z = 0$ and $E_z \neq 0$. The electromagnetic fields and resonant frequency that define these electromagnetic configurations are referred to as modes of the cavity. The cavity modes are obtained from the eigenfunctions and eigenvalues that solve Maxwell's equations without sources subject to the conducting boundary conditions. The results of this procedure for the TE modes are now listed without proof but detailed derivations can be found in the above-mentioned resources. These TE modes of a cylindrical cavity will be relevant in chapter 4 when discussing the design of sample host cavities.

The infinite TE modes of a cylindrical cavity are organized by three indices, $n = 0, 1, 2, ...$, $m = 1, 2, 3...$, and $l = 1, 2, 3...$. Re-emphasizing that this discussion is for a vacuum-cavity, the mode frequencies are

$$f_{nml} = \frac{c}{2\pi} \sqrt{\left(\frac{p'_{nm}}{a}\right)^2 + \left(\frac{l\pi}{d}\right)^2} \tag{2.5}$$

Where c is the speed of light and p'_{nm} is the mth root of the derivative of the nth order Bessel function of the first kind, $J_n(\rho)$. Omitting the harmonic time-dependence and accepting that the physical field is obtained from the real part of the product of the following with $e^{i\omega t}$, the TE_{nml} fields can be expressed as

15

[Pozar, 1990]

$$E_z = 0$$

$$H_z = H_0 \qquad\qquad \times \qquad J_n\left(\frac{p'_{nm}}{a}\rho\right)\cos{(n\phi)}\sin\left(\frac{\pi l}{d}z\right)$$

$$E_\rho = \frac{i\eta H_0}{2\pi c}a\frac{nf_{nml}}{\left(p'_{nm}\right)^2} \quad \times \quad \frac{a}{\rho}J_n\left(\frac{p'_{nm}}{a}\rho\right)\sin{(n\phi)}\sin\left(\frac{\pi l}{d}z\right)$$

$$H_\rho = \pi H_0 \frac{a}{d}\frac{l}{p'_{nm}} \qquad \times \qquad J'_n\left(\frac{p'_{nm}}{a}\rho\right)\cos{(n\phi)}\cos\left(\frac{\pi l}{d}z\right)$$

$$E_\phi = \frac{i\eta H_0}{2\pi c}a\frac{f_{nml}}{p'_{nm}} \qquad \times \qquad J'_n\left(\frac{p'_{nm}}{a}\rho\right)\cos{(n\phi)}\sin\left(\frac{\pi l}{d}z\right)$$

$$H_\phi = -\pi H_0 \frac{a}{d}\frac{nl}{\left(p'_{nm}\right)^2} \quad \times \quad \frac{a}{\rho}J_n\left(\frac{p'_{nm}}{a}\rho\right)\sin{(n\phi)}\cos\left(\frac{\pi l}{d}z\right)$$

$$(2.6)$$

Where H_0 is the maximum magnetic field z-component amplitude and $\eta = \sqrt{\mu/\epsilon}$ is the free-space wave impedance. The role of the indices is made clearer by equation 2.6. n, m, and l correspond to the number of nodes in the fields as they transverse the ϕ, ρ, and z coordinates specified in figure 2.2.

2.2.1 Surface impedance

An important addition must be made to the preceding discussion before utilizing equations 2.5 and 2.6 to motivate cavity features relevant for their design and operation. In the discussion of resonant cavities to this point, no information has been conveyed about the interaction of the electromagnetic radiation with the conducting boundaries. In a real cavity the field will penetrate a relatively small (though finite) distance into the material as the induced currents serve to screen it from the interior. This will result in a perturbation to the dimensions of the cavity. For the application considered in this text the field configurations specified in equation 2.6 will see a trivial change that can be ignored. The resonant frequency of equation 2.5 will change by a small, but detectable,

amount. Most importantly, the induced screening currents will produce dissipation in the material which will act as a source of damping. Including these effects changes the analysis from a cavity with walls made from a nonexistent perfect conductor to one that can describe a real system.

The response of a conducting surface to an electromagnetic plane wave is quantified with the surface impedance, Z. For simplicity, consider the interaction of an electromagnetic plane wave with a metallic surface. While this does not strictly describe the situation of a resonant cavity, it should provide a reasonable approximation. For a plane wave with electric field in the x-direction, magnetic field in the y-direction, and normally incident at $z = 0$ on a semi-infinite slab oriented with its surface normal in the z direction of conducting material the surface impedance is defined as [Turneaure et al., 1991, Walsh and Tomaselli, 1990]

$$Z \equiv \frac{E_x(0)}{H_y(0)} = \frac{E_x(0)}{\int_0^\infty J_x(z)dz} = -i\omega\mu_0 \frac{E_x(0)}{\partial E_x/\partial z|_{z=0}} = i\omega\mu_0 \frac{\int_0^\infty H_y(z)dz}{H_y(0)} \qquad (2.7)$$

The first equivalence can be shown from Ampere's law ignoring the displacement current which is valid in metals at the microwave frequencies considered in this work. The next two equalities are obtained from Faraday's law and the implicit harmonic time dependence, $e^{i\omega t}$.

The surface impedance is often expressed in terms of its real and imaginary components: $Z = R_s + iX_s$. R_s and X_s are referred to as the surface resistance and surface reactance respectively. Obtaining the surface impedance for a given material requires a combination of Maxwell's equations with a material-dependent equation quantifying the relationship between the incident field and the induced current. Developing this relation and making calculations of the surface impedance will be the focus of chapter 3. For the current purposes the

definition will suffice to demonstrate its utility.

The surface resistance and reactance can be directly linked to the dissipation and spatial extent of an electromagnetic wave incident on a conducting surface. In general, an effective penetration depth can be defined as

$$\lambda_{eff} \equiv \text{Re} \left\{ \frac{\int_0^\infty H_y(z)dz}{H_y(0)} \right\} = \text{Re} \left\{ -\frac{i}{\omega\mu_0} (R_s + iX_s) \right\} = \frac{1}{\omega\mu_0} X_s \qquad (2.8)$$

Where the expression in the definition is recognized as the last equality in equation 2.7. Therefore, the surface reactance, $X_s = \omega\mu_0\lambda_{eff}$ conveys the extent of electromagnetic penetration in a material. The surface resistance can be linked to dissipation in a material using the time-averaged Poynting vector at the material surface. The real part of this quantity conveys the power density (power P per unit area, A) flowing into the surface, which for the system currently under consideration, will completely account for energy dissipating in the bulk of the material. Consider the component of the real part of the time-averaged Poynting vector oriented parallel to the normal of the surface

$$\frac{P}{A} \equiv \text{Re} \left\{ \langle S_\perp \rangle \right\} = \text{Re} \left\{ \frac{1}{2} E_x(0) H_y^*(0) \right\} = \frac{1}{2} R_s |H(0)|^2 \qquad (2.9)$$

This expression relates the power flow density into the surface to the material surface resistance and applied field strength. The time-dependence is accounted for in the time-averaging and the E and H of the above expression are complex phasors. The relevant field is the magnetic field parallel to the material surface, which is the only component that exists in the geometry currently under consideration. The last equality in equation 2.9 was made by replacing the expression for E using the definition in equation 2.7 and taking the real part of the result.

Equation 2.9 can be used to include dissipation in the analysis of resonant cavities for an arbitrary conducting material.

2.2.2 Relevant quantities

Quantities relevant for designing, operating, and analyzing resonant cavities can be derived for the geometry defined in figure 2.2 in the TE_{nml} mode from equations 2.5 and 2.6. The energy stored in the resonator oscillates between the electric field and the magnetic field. Therefore, the time-averaged electric and magnetic energies must be equal. That is $U = 2U_e = 2U_m$ where U is the energy in the resonator and U_e and U_m are the time-averaged stored energy in the electric field and magnetic field respectively. The total energy of the TE_{nml} mode can be expressed as

$$U_{nml} = \frac{\pi}{8}\epsilon\frac{a^4 d}{c}\left(\frac{\omega_{nml}}{p'_{nm}}\right)^2\left(1 - \frac{n^2}{(p'_{nm})^2}\right)\eta^2 H_0^2 J_n^2(p'_{nm}) \tag{2.10}$$

Where $\omega_{nml} = 2\pi f_{nml}$. The other symbols are defined in the beginning of the section.

The power dissipated in the cavity walls for a given surface resistance, R_s can be expressed as [Pozar, 1990]

$$P = \frac{1}{2}R_s\pi H_0^2 J_n^2(p'_{nm})\left\{\frac{ad}{2}\left[1 + \left(\pi\frac{a}{d}\frac{nl}{(p'_{nm})^2}\right)^2\right] + \left(\pi\frac{a^2}{d}\frac{l}{p'_{nm}}\right)^2\left(1 - \frac{n^2}{(p'_{nm})^2}\right)\right\} \tag{2.11}$$

The quality factor can be found using the preceding expressions in definition 2.4 but will depend on an arbitrarily defined surface resistance. It is common to define a factor that depends only on the geometry of the cavity to describe the quality factor for a given surface resistance

$$Q = \frac{\omega U}{P} = \frac{\omega U}{\frac{1}{2}R_s\int_A\left|\hat{n}\times\vec{H}\right|^2 da} = \frac{G}{R_s}$$

Where A is the surface area of the cavity, $\hat{n}$ is the normal vector to the surface,

and G is the geometry factor. The geometry factor can therefore be defined as

$$G = \frac{\omega U}{\frac{1}{2} \int_A \left| \hat{n} \times \vec{H} \right|^2 da} = \mu_0 \omega \frac{\int_V |H|^2 dv}{\int_A \left| \hat{n} \times \vec{H} \right|^2 da} \tag{2.12}$$

Where V is the volume of the cavity. The geometry factor can be evaluated for the TE_{nml} mode from equations 2.10 and 2.11

$$G_{nml} = \frac{1}{2} \eta \left((p'_{nm})^2 + \left(\pi \frac{a}{d} l \right)^2 \right)^{3/2} \frac{1 - \frac{n^2}{(p'_{nm})^2}}{\left[(p'_{nm})^2 + \left(\pi \frac{a}{d} n l \right)^2 \right] + 2\pi^2 \left(\frac{a}{d} \right)^3 l^2 \left(1 - \frac{n^2}{(p'_{nm})^2} \right)} \tag{2.13}$$

In general, these quantities will be abstracted away or computed numerically for more complicated but technologically useful structures. Expressing them for the cylindrical cavity as is done here can be useful for building intuition since many structures useful for application will be variations of a cylindrical cavity. The fields will not exactly match those of equation 2.6 but will be visually recognizable. Further useful quantities, such as the magnetic field amplitude at the surface for a given amount of stored energy, can be readily obtained from these equations and the fields of a given mode. In general, what additional quantities are of interest depends on the application. Accordingly, definitions will be delayed for when the applications are discussed.

2.2.3 Connection between a resonant cavity and an RLC circuit

As discussed previously and as is evident from equation 2.6, the stored energy in a resonant cavity will oscillate between the electric and magnetic fields. This motivates an alternative description of a resonant cavity where it is treated as a resistor-inductor-capacitor (RLC) circuit. The connection between the two stems from inductance and capacitance being defined by a geometry and its ability to

store magnetic and electric energy respectively. In spirit this exactly matches the situation of a resonant cavity. It is straightforward to show that the characteristic resonance differential equation, of the form of equation 2.1, describes the oscillation of the current through the inductor or voltage across the capacitor. In other words, the RLC circuit describes a damped resonator that transfers its energy between an electric field and a magnetic field. From here it is a plausible that a RLC circuit could be imagined with specifically chosen values to match the properties of a resonant cavity. Specifically, to have the same resonant frequency, stored energies, and quality factor.

For different modes of a cavity, it is common to describe them with different connections (series, parallel) of the three components of the RLC circuit. This is done to best match the fields and currents present in the geometry. Consider figure 2.3, where the left image demonstrates the direction and magnitude of the screening current in the cavity walls for a TE_{011} mode. The screening current winds around the length of the cylinder and follows the $\sin(\pi z/d)$ dependence as indicated in equation 2.6. The winding current resembles the coils of an inductor in circuit analysis. A more realistic model of an inductor includes a series combination of cells consisting of a series inductance and resistance in parallel with a capacitance as demonstrated in the center image of figure 2.3. The inductance corresponds to a single coil of the winding current, the resistance represents losses in the conducting material, and the capacitance accounts for charge build up between neighboring coils. The current is changing at each of these cells so a full transmission line analysis would be needed to go further with this analysis. That is something of a trivial exercise as the physical connection between the circuit model and the cavity is loose at best. What matters is the idea that the stored electric and magnetic energies in a physical cavity can

be viewed as an equivalent circuit with some effective impedance arising from a configuration that allows a resonance using a capacitance and an inductance. The choice of RLC configuration is trivial as any combination can be chosen to match the properties of the cavity or the impedance of a more carefully considered circuit model.
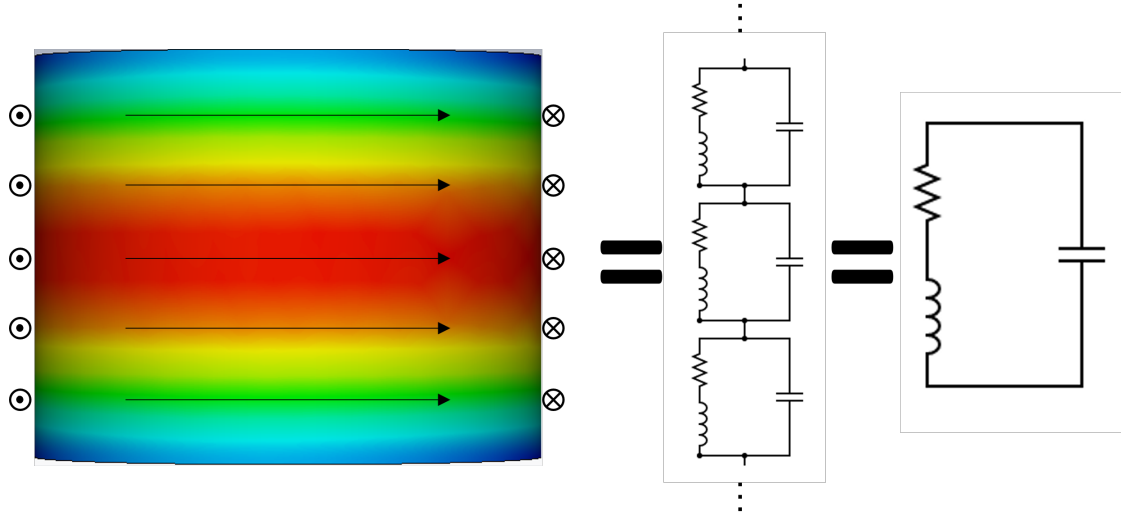
Figure 2.3: (Left) Sketch of the screening currents in the walls of a cavity containing a TE_{011} mode excitation. The colors demonstrate magnitude with blue being the lowest value and red being the highest. The arrows are intended to demonstrate the current looping around the circular portion of the cylinder. The currents in the top and bottom also follow a circular direction. (Center) "Realistic" circuit model of an inductor where each RLC cell corresponds to a wind of a coil. This is intended to model the effective "coils" of the screening currents pictured in the left image. (Right) Equivalent RLC circuit for the cavity. Its inductance, capacitance, and resistance can be chosen to match the resonant frequency, losses, and stored energy of the physical cavity. These values could also be chosen to be equivalent to the effective impedance of the center circuit.

To move forward the circuit configuration in the right image of figure 2.3 is chosen as the equivalent RLC circuit for the cavities studied in this work. Its inductance, capacitance, and resistance can be chosen to produce an equivalent impedance to the center image of figure 2.3 and can act like a resonator with the

same resonance frequency, dissipation, and time-averaged electric/magnetic energy as a real resonant cavity. If the equivalent circuit were driven with a sinusoidal current source having magnitude, I_D, and angular frequency, ω, then its dynamics can be described by the current through the inductor, I_L, by the differential equation

$$\ddot{I}_L + \frac{R}{L}\dot{I}_L + \frac{1}{LC}I_L = \frac{1}{LC}I_D \cos(\omega t)$$

It was assumed that the inductance and resistance do not vary with time. This expression is in the form of equation 2.1 so the analysis of section 2.1 can be directly applied. For the following analysis the system is assumed to be very weakly damped and it is assumed that $\omega = \omega_r$ (with ω_r being the resonant angular frequency). The quality factor will be

$$Q = \frac{1}{R}\sqrt{\frac{L}{C}} \tag{2.14}$$

The resonant angular frequency will be

$$\omega_r = \sqrt{\frac{1}{LC}} \tag{2.15}$$

The solution for the steady state inductor current is

$$I_L = QI_D \cos(\omega t - \phi) \tag{2.16}$$

The phase can be found from equation 2.3 but will not be relevant to the current analysis.

The time-averaged energies stored in the inductor and capacitor will be equal, so the total energy can be expressed as

$$U = 2 \times \frac{1}{2}L\bar{I}_L^2 = \frac{1}{2}LQ^2I_D^2 = \frac{1}{2}\frac{L^2}{R^2C}I_D^2 \tag{2.17}$$

The equivalent circuit should describe the resonant cavity independently from the drive current (input power to the cavity). The goal of this analysis is to link

the RLC parameters to those of a real cavity. Therefore, the energy must be appropriately normalized such that an analogous normalization can be made to the stored energy in a resonant cavity. Here the choice is made to normalize the energy to the square of the maximum of the oscillation variable. For the RLC circuit this is the current through the inductor (or the voltage across the capacitor) while for a cavity this would be the amplitude of the magnetic (or electric) field. According to equation 2.16 this will be $Q^2 I_D^2$. Let the energy normalized by the square of the amplitude of the oscillation be denoted as $\tilde{U}$

$$\tilde{U} = \frac{U}{Q^2 I_D^2} = \frac{1}{2}L \tag{2.18}$$

By combining equations 2.14, 2.15, and 2.18 values for the resistance, inductance, and capacitance can be found such that they produce a given normalized energy, quality factor, and resonant frequency.

$$R = \frac{2\tilde{U}\omega_r}{Q}$$
$$L = 2\tilde{U} \tag{2.19}$$
$$C = \frac{1}{2\tilde{U}\omega_r^2}$$

The choices for R, L, and C could be chosen in accordance with the TE_{nml} modes by plugging in the results of the section 2.2.2. Specifically, the resonant frequency of equation 2.5, the stored energy from equation 2.10 normalized to the amplitude of oscillation for the given mode, and $Q = G/R_s$ with the geometry factor as specified in equation 2.13. The normalization of the stored energy could in general be nontrivial, even for the simple example of the cylindrical cavity. In general, the cavity geometry is too complicated for an analytical solution, but numerical solutions can easily provide the required information in

practice. For the cylindrical cavity the normalization of the important TE_{011} mode can easily be obtained to be H_0. In this case the normalized energy would simply be divided by H_0^2.

While it is instructive to link the RLC circuit to the resonant cavity in detail, it is not particularly useful. What matters is the acceptance that the RLC circuit picture of a resonant cavity is valid. This picture allows for calculating an effective impedance of the cavity. This can be used to treat the cavity as part of an RF system in a transmission line model which will be important for the operation of resonant cavities and analyzing the resulting measurements.

2.3   Operation of high-Q cavities

There are many uses for resonant cavities. While there is overlap for many applications, there are no general operation procedures. Indeed, the range of cavity quality factors and application goals leads to a variety of methods. This work focuses on using extremely high quality factor resonators to excite large electromagnetic fields on the surface of a sample. This section will focus on the operation of these high quality factor resonators. The purpose of this operation is to measure relevant information about the surface of the cavity (or, more specifically, that of a specific surface containing the sample). Therefore, this section will describe the measurements and analysis used to produce quantities of interest.

First, the electromagnetic modes must be excited in the resonant cavity. This is done by connecting a signal generator to the cavity through a coupling structure. Second, the cavity must be continuously driven to produce a steady state

as the energy is damped by the surface resistance of the boundaries. For high quality factor cavities this can be challenging as the bandwidth of the resonance is extremely narrow. In practice the resonant frequency will drift with systematic variations so the drive frequency must be adjusted accordingly to maintain a near-resonance steady state. Lastly, relevant measurements and analysis must be performed to extract information of interest.

2.3.1 Electromagnetic coupling

So far in the discussion of resonant cavities, the geometry has been described and treated as a closed boundary surrounding a dielectric or vacuum interior. Within the cavity an electromagnetic field simply exists. In practice it is necessary to couple energy into the cavity to excite the electromagnetic mode. Typically, this is done by modifying the geometry to include a small aperture in a region of the cavity where the intended mode of operation has relatively small fields. This opening can then be attached to a waveguide to connect the cavity to a signal generator.

The focus of this work is resonant cavities, so in the preceding discussion waveguides have been omitted. Because waveguides are required to connect cavities to external drivers, a very brief introduction to waveguides is now presented. If the reader is unfamiliar with the topic, then the same references used for resonant cavities should be considered [Jackson, 2012, Pozar, 1990]. A waveguide is essentially a resonant cavity (consider, for example, a rectangular solid cavity or the cylinder of figure 2.2) with no end-plates. The lack of end plates prevents the formation of persistent standing wave excitations but can

support propagation of waves along the length of the waveguide. This propagation can exist only above a geometry-dependent cutoff frequency. Qualitatively this can be considered as the frequency corresponding to the largest wavelength that can "fit" into the waveguide. If two disjoint conducting surfaces are present in the waveguide, then transverse electromagnetic (TEM) wave propagation can be supported. A TEM mode is characterized by the electric and magnetic fields being entirely perpendicular to the direction of propagation. The cutoff frequency of a TEM mode is zero, which offers utility for applications.

To describe the electromagnetic coupling into a cavity some new quantities are defined. First is the loaded quality factor,

$$Q_L \equiv \frac{\omega U}{P_{total}} \tag{2.20}$$

This quantity is similar to the quality factor that has been considered previously but is distinguished by considering the total power. In the preceding discussions of the closed cavity the only dissipation would be in the cavity walls, denoted as P_0. With the introduction of a coupling aperture some power will leak from the cavity through the opening, denoted as P_e. The total power loss can then be described as

$$P_{total} = P_0 + P_e$$

Note that any dissipation that occurs on the coupling surfaces is included in P_0. P_e is reserved for power flowing out of the system.

The quality factor that was discussed before this section was defined in terms of P_0. In the new situation where a coupling mechanism is included, this quality factor will be referred to as the intrinsic quality factor, $Q_0 \equiv \frac{\omega U}{P_0}$. Another quality factor, denoted as the external quality factor, is defined to similarly account for the coupled power, P_e. That is $Q_e \equiv \frac{\omega U}{P_e}$. With these definitions in place the

various quality factors can be related,

$$\frac{1}{Q_L} = \frac{1}{Q_0} + \frac{1}{Q_e} \tag{2.21}$$

The external quality factor will be independent from dissipation on the cavity walls and will be ideally independent from applied power. Only changes to the geometry of the coupling structures should change Q_e for a given cavity. Ensuring the external quality factor corresponding to a series of measurements is constant for relevant parameter ranges can be used as a tool for checking the quality of the measurements.

It is often convenient to express equation 2.21 as $\frac{1}{Q_L} = \frac{1}{Q_0}\left(1 + \frac{Q_0}{Q_e}\right)$. Defining the coupling factor $\beta \equiv \frac{Q_0}{Q_e}$ this can produce an equation relating Q_0 to Q_L

$$Q_0 = Q_L\left(1 + \beta\right) \tag{2.22}$$

This expression will be useful for the measurement method employed in this work since the Q_L and β will be directly measured but Q_0 is the value of interest. The coupling factor can be expressed in a useful form by using the definitions of Q_0 and Q_e to eliminate the frequency and stored energy dependence.

$$\beta = \frac{Q_0}{Q_e} = \frac{P_e}{P_0} \tag{2.23}$$

For a given intrinsic quality factor the coupling factor and external quality factor can be used interchangeably to describe the coupling of energy into and out of a cavity. The value of the coupling factor will directly describe the qualitative nature of the coupling. More specifically, the reflections resulting from impedance mismatch between the coupling system and the resonant cavity. The external quality factor is related to the physical configuration that can produce a desired coupling factor for a given intrinsic quality factor. For the high intrinsic

quality factor resonators considered in this work, the external quality factor is typically designed to exist in a similar range. This reduces the amount of power reflected from the cavity. In general, to efficiently produce a target external quality factor, the shape of the waveguide must be altered to better transition the field configuration of the propagating waveguide mode to those of the resonant cavity. A typical method of connection to a signal generator would be a coaxial cable (coaxial waveguide operated below the cutoff frequencies of the TM and TE modes so that it operates purely in the TEM mode) with $50\,\Omega$ wave impedance. The field configuration of the coaxial TEM mode looks very different from many cavity modes. The geometry of the coaxial waveguide at its end can be adjusted to force the fields into a more similar form to the desired modes. This adjusted form will be referred to as the coupler. To raise and lower the external quality factor, the coupler can be moved further from and closer to the cavity aperture. For some coupler shapes, rotating the coupler relative to the fields of the cavity can also be effective. The design of couplers for different applications is a challenging topic and the interested reader should find a more complete source such as [Padamsee et al., 2008].

The coupling system is typically referred to as the forward power coupler (FPC). While bringing power into the cavity is one of its functions, it is important to note that power also travels in the opposite direction as well. In steady state operation the reverse signal traveling on the FPC will be the sum of the reflections from the cavity due to impedance mismatch and the waves leaking from the cavity that produce the emitted power, P_e.

In addition to the FPC it is often useful to include a second independent coupling antenna, denoted as the transmitted power coupler (TPC) or field probe.

The TPC will be designed to have an external quality factor, Q_T, that is greater than the target Q_0 and Q_e by several orders of magnitude. This ensures the power leakage through the transmitted power probe does not meaningfully impact the measurement while providing enough of a signal to give information about the energy stored in the cavity. The utility of the TPC is that it probes the energy stored in the cavity without becoming convoluted with reflected power or the mechanical stress resulting from high power that would be observed on the FPC and its signal path. This clean signal is useful for both measurement and control of the cavity.

The region labeled as "cavity drive & readouts" in figure 2.4 demonstrates the implementation of a cavity with FPC and TPC ports at the block level. A signal generator is employed to produce a sinusoidal waveform. Portions of the signal are removed for frequency measurement and control purposes to be discussed later, but the bulk of the signal goes on to be amplified and made incident on the FPC. Note that a circulator and a matched load are positioned at the amplifier output to protect the amplifier from high-power reflections from the cavity. In addition, directional couplers remove portions of the forward and reverse power signals for measurement. The clean TPC signal is split for measurement and control purposes.

2.3.2 Frequency control

In practice, driving a high quality factor resonator to a near-resonance steady state is nontrivial. The bandwidth of the resonance peak, as seen in figure 2.1, can become so narrow that systematic perturbations to the geometry of the cav-

ity can change the resonant frequency enough to greatly reduce the amplitude of the fields in the resonator. The resonator that will be discussed in this work routinely observes quality factors of $Q_L = 10^{10}$ at 4.0 GHz. From the definitions of the quality factor in section 2.1, this leads to a bandwidth of only 0.4 Hz. If the cavity were driven at a static frequency, then the resonance frequency must only shift by an order of one ten-billionth of its magnitude to produce a major reduction of the field amplitude. In practice the resonance frequency drifts by more than this amount due to slight oscillations in the cryostat pressure, systematic vibrations, and electromagnetic pressure from strong fields inside the cavity.

To account for the drifting resonant frequency, a phase-locked loop (PLL) is implemented to continuously modify the frequency output of the signal generator to ensure the cavity is driven as close to resonance as possible. The PLL compares the phase of two signals, the input and the output of the resonant cavity. The output of the cavity is defined here to mean the signal produced on the transmitted power coupler (TPC) discussed in section 2.3.1. The phase difference between the two signals is used as a frequency modulation input for the signal generator driving the cavity. As will be explained, this scheme allows for continuously shifting the frequency as to "lock" onto a desired phase difference between the two signals. Recall from section 2.1 that the phase difference between the input and output of a resonator depends on the frequency and will take a value of $\pi/2$ when driven exactly on resonance. Therefore, the goal will be to configure the PLL such that it locks onto this on-resonance phase difference.

The portion of figure 2.4 labeled "frequency control" demonstrates the implementation of the PLL. The cavity input (coupled away from the output of the
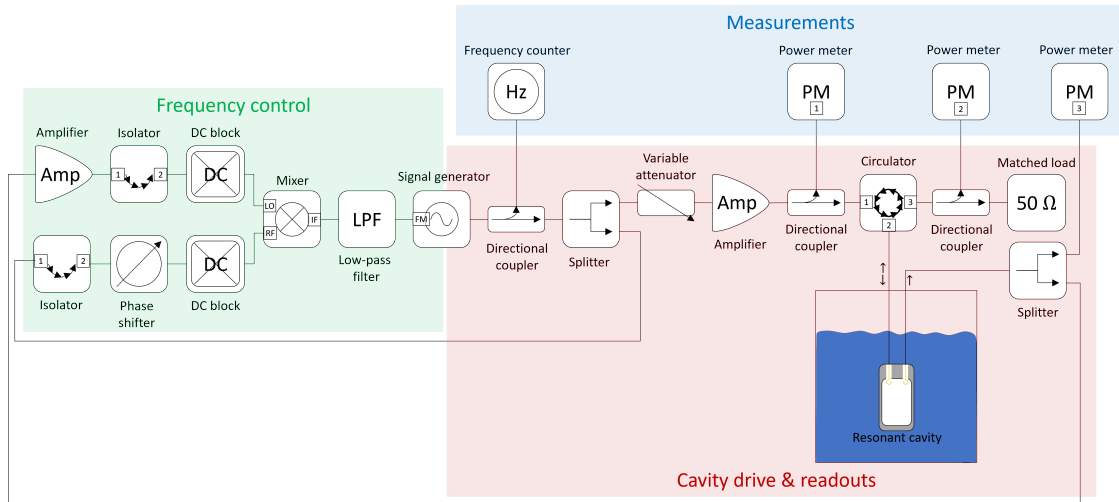
Figure 2.4: Block diagram demonstrating the operation of a two-port high quality factor resonant cavity. The elements are divided to convey their role in frequency control, cavity drive, and measurement. The frequency control area consists of an analog phase-locked loop. The measurements section uses devices capable of detecting signal frequency and power. The cavity drive & readouts section indicates how the signal is propagated to the cavity and where signals are divided or coupled away from in order to connect to the other sections.

signal generator) and the cavity output (from the TPC) are passed through an isolator and a DC block to prevent spurious effects in the mixer. A mixer is a three-port device with many applications beyond the scope of this text [Pozar, 1990]. Here a very specific and simple configuration is employed. The inputs will be the local oscillator (LO) and radio frequency (RF) ports. For the purposes of this discussion the two will be treated as identical although there are differences which can be important if their input magnitudes are small. In the setup used for the experiments of this text, the transmitted power signal is passed through an amplifier so that it is sufficiently large for all cavity drive powers considered. The signal generator output travels a relatively short distance to the mixer so its amplitude is sufficient without amplification. For demonstra-

tion let the input signals of the mixer be expressed as

$$v_{RF} = v_1 \cos(\omega t + \phi_1 + \theta)$$

$$v_{LO} = v_2 \cos(\omega t + \phi_2 - \phi_R)$$

(2.24)

Here ω is the angular frequency produced by the signal generator, t is time. ϕ_1 and ϕ_2 are the phase differences induced by propagation between the signal generator output and the RF input and the transmitted power coupler and LO input respectively. θ will be the added phase from the phase shifter pictured in figure 2.4. ϕ_R is the change in phase between the resonator input and output described in equation 2.3. The output of the mixer will be the intermediate frequency (IF) port of the mixer. This will produce what is essentially the product of the signals on the LO and RF ports.

$$v_{IF} = v_{rf} \times v_{LO} = \frac{v_1 v_2}{2} \left[\cos(\phi_1 - \phi_2 + \theta + \phi_R) + \cos(2\omega t + \phi_1 + \phi_2 + \theta - \phi_R) \right]$$

The arguments of the sinusoids in the final equality are the sum (up-converted portion) and difference (down-converted portion) of the arguments of equation 2.24. The frequency of the cavity output is identical to its input so the down-converted portion is a DC signal while the up-converted portion is in the GHz range. Applying a low-pass filter (LPF) will produce a DC signal dependent upon the phase difference between the inputs to the RF and LO ports.

$$v_{LPF} = \frac{v_1 v_2}{2} \cos(\phi_1 - \phi_2 + \theta + \phi_R)$$

(2.25)

This is used for frequency modulation (FM) of the signal generator output. The resulting output angular frequency of the signal generator can be expressed as

$$\omega = \omega_0 + \alpha \cos(\phi_1 - \phi_2 + \theta + \phi_R)$$

(2.26)

Where ω_0 is a chosen center frequency and α is the combination of a chosen FM multiplier with the amplitude of equation 2.25.

While the resonant frequency will change with time, the changes are numerically small. The PLL is needed to continuously track these changes. To demonstrate this, equation 2.26 can be rearranged as

$$\phi_R = \cos^{-1}\left(\frac{\omega - \omega_0}{\alpha}\right) - \theta - (\phi_1 - \phi_2) \tag{2.27}$$

Assume the system starts with the drive frequency close to resonance. This is typically manageable in practice. The resonant frequency can be measured using a network analyzer and the center frequency can be chosen such that $\omega \approx \omega_R$. If it is assumed that the FM gain is chosen such that $\alpha \gg \omega_R - \omega_0$, then the argument of the inverse cosine in equation 2.27 will approach zero. This results in an expression that relates the resonance phase shift to RF system values.

$$\phi_R = n\frac{\pi}{2} - \theta - (\phi_1 - \phi_2)$$

With $n = 1$ or $n = 3$. This equation indicates that the PLL will constantly adjust the drive frequency to maintain a constant ϕ_R. This constant phase difference is determined by the system-dependent path lengths, encoded in ϕ_1 and ϕ_2, and a manually controlled phase shifter value, θ. By adjusting θ to maximize the magnitude of the transmitted power, the PLL will produce a steady state drive frequency producing the on-resonance phase difference of $\phi_R = \pi/2$. Specifically, resonance would occur when $\theta = \frac{\pi}{2}(n - 1) - (\phi_1 - \phi_2)$.

To find the value of n, consider the time derivative of equation 2.26 assuming the system is driven on resonance

$$\dot{\omega} = -\alpha\dot{\phi}_R \sin\left(\phi_1 - \phi_2 + \theta + \frac{\pi}{2}\right)$$

With the assumption that $\omega = \omega_R$ initially, any change to the resonant frequency will have the same sign as the corresponding change to the resonant phase. That is, $\text{sign}(\dot{\omega}_R) = \text{sign}(\dot{\phi}_R)$. For the the drive frequency to track the change

in resonance, the sine must produce a negative value. This will be the case for $n = 3$, so the desired phase shifter setting is $\theta = \pi - (\phi_1 - \phi_2)$.

The simple explanation of PLL operation presented here is incomplete and does not convey important properties such as the bandwidth and rate of approaching the steady state drive frequency. Moreover, mixers do not truly multiply the two signals, although it is a reasonable description. The above description hopefully conveys an intuition about what the "phase-locked" portion of the PLL means and how it is accomplished by the block diagram in figure 2.4. This diagram completely describes the implementation that will be used in the experiments of this work.

2.3.3 Measurements and analysis

Ultimately, the goal is to use the driven cavity resonator to produce high amplitude RF fields on the surface in order to probe the response of the cavity wall material in the extreme conditions. Using the PLL discussed in the previous subsection, the cavity can be reliably driven to a steady state near its resonance frequency. At resonance, the desired high amplitude fields can be realized for a relatively modest drive power. The focus of this subsection will be the measurements carried out in this steady state situation and the analysis required to produce relevant information. Specifically, the desired information is the surface impedance of the cavity wall material and the amplitude of the surface magnetic field in the steady state. The details of the transient case are not required for understanding the measurement procedure and the acquisition of important quantities and will be omitted from this discussion. It can be essen-

tial for interpreting the observed measurements during cavity operation and, in some cases, the subsequent analysis. For details on the transient analysis refer to a more complete resource [Padamsee et al., 2008].

The measurements that will result in the data used for analysis and their location in the cavity drive path are indicated in the "measurements" portion of figure 2.4. These "raw" measurements consist of the output frequency of the signal generator using a frequency counter, the power of the amplified signal traveling towards the cavity (power meter 1), the reverse power traveling away from the cavity (power meter 2), and the transmitted power carried out of the cavity by the TPC discussed in section 2.3.1 (power meter 3). The procedure for operation involves turning on power and adjusting the added PLL phase until either the transmitted power (P_t) is maximized or the reverse power (P_r) is minimized. For a properly designed system these events happen simultaneously. Spurious effects, such as reflections or resonances in the coupling path, can lead to a discrepancy between the extrema. Once the optimized phase is set the values of the forward power, P_f, and reverse power in the steady state are recorded. The signal generator is then turned off. The falling edge of P_f measured on power meter 1 is used as a trigger to record traces of P_r and P_t from the trigger time to a user-defined value dependent upon the decay time of the cavity.

Loaded quality factor

The loaded quality factor is obtained from the power traces. Both P_r and P_t could be employed for this purpose. In this work P_t is used as there is less threat of spurious effects from cable heating or line damage from the relatively

high powers carried on the line to the FPC. From the definition of the loaded quality factor in equation 2.20,

$$P_{total} = -\frac{dU}{dt} = \frac{\omega}{Q_L}U \tag{2.28}$$

Solving this gives the stored energy in the undriven cavity can be expressed as

$$U = U_0 \exp\left(-\frac{\omega}{Q_L}t\right)$$

Where U_0 indicates the stored energy in the cavity at steady state. By definition of the transmitted quality factor, $U \propto P_t$. Therefore, measuring the transmitted power shortly after turning off the signal generator directly probes the steady state stored energy in the resonator. The characteristic time scale of the energy decay observed on the transmitted power will be $\tau = \frac{Q_L}{\omega}$. This decay time should be considered when choosing what time range to use on the power meter trace after the triggering event. More importantly, extracting the characteristic decay time from the measured power yields the loaded quality factor.

The solution to equation 2.28 considered so far assumed that the loaded quality factor does not depend on time. In general, this is not the case as the surface resistance of a material can change with the strength of the applied field. The desired $Q_L(t)$ will be that which corresponds to the maximum stored energy in the cavity. Recall that the amplitude of the RF fields in the cavity is proportional to the square root of the stored energy and therefore to the square root of the measured transmitted power. Therefore, it is of interest to obtain the characteristic decay time close to the time of the signal generator being shut off.

To obtain the characteristic decay time, the $P_t(t)$ trace can simply be fit with a single exponential (or equivalently, by fitting a line to $log(P_t(t))$). The fit requires a finite domain so it is necessary to consider the evolution of the decay

to larger times. If the loaded quality factor has nontrivial dependence on time, then issues may be apparent. First, the exponential solution does not exactly describe the experimental situation. Second, even if the exponential does approximate the situation, fitting to the single exponential will combine a range of values for the loaded quality factors. In either case the reported value will deviate from the desired one at maximum field amplitude. The working solution to both issues is to consider a narrow time domain for the fit. For a small enough portion of the decay, the exponential solution approximates the situation in a reasonable manner for practical forms of the decaying $Q_L(t)$. If the lower bound of the fit is chosen to be close to the trigger event, then the loaded quality factor will not change substantially in a small time and can be treated as the value at max amplitude. It is important to be aware that this procedure has limitations. Depending on the form of $Q_L(t)$ and how strong of a dependence it has on time, the error introduced for a given time domain may need to be considered.

For the measurements presented in this work, the time scale of the power meters is chosen to maximize the number of data points that can be stored in the trace for the desired narrow fit domain. The time domain included in the trace begins a small amount before the trigger and extends to the time where the power was $50\% - 80\%$ of its value after the trigger. This time domain could have been more carefully controlled, but the variation is not expected to have detrimental effects on measurement quality. For the fit domain, the lower bound was a few data points after the trigger and extended to an upper bound corresponding to when the power had decayed to 81% of its value at the lower bound. Here 81% is chosen since it corresponds to a field at 90% of its value at steady state. The reported measurement uncertainty on the measured fields will be roughly $\sim 10\%$, so this was chosen as an acceptable amount of variation on the quality

factor. The choice of lower bound being a few data points after the trigger event was made to reduce measurement noise. Note that for the large quality factors considered in this work, all residual reflections after shutting off the signal generator will have decayed before the power meter begins the trace due to the large cavity decay times (4 ms – 400 ms). Waiting a few extra data points also helps ensure this is the case for lower quality factor measurements.

Reflection coefficient and the coupling factor

At this point in the analysis the loaded quality factor has been obtained. A value for β must be obtained to convert the loaded quality factor to the intrinsic quality factor as in equation 2.22. In order to understand how β can be obtained from the power meters and frequency counter of figure 2.4, it is necessary to consider the coupled cavity and its connection to the signal generator through a transmission line. This configuration is visualized in figure 2.5. The amplified signal is incident on a matched transmission line (coaxial cable), that is in turn incident upon the coupler and cavity. The cavity will be modeled by the RLC circuit discussed in section 2.2.3. The coupler is modeled in transmission line theory as a transformer. Here the ratio of coils, n, is not required to be an integer. The role of the transformer will be to modify voltages defined on the generator (cavity) side by a factor of n ($1/n$) when they are used to obtain a quantity on the opposite side. The relevant effect is that the transmission line model expressions for coupler-dependent quantities such as P_e, β, and Q_e will be dependent on n^2. The value of n can therefore encode the systematic effects of the coupler geometry. If the reader is not comfortable with the transformer, then it can be omitted with no change to the results relevant for this work.
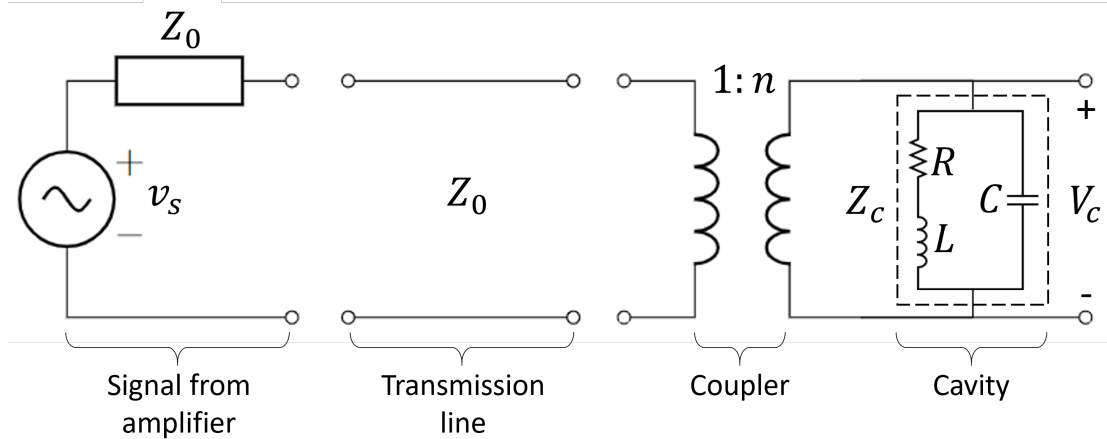
Figure 2.5: Transmission line model of the connection between the signal generator and the cavity through its forward power coupler (FPC). The impedance of the cavity is modeled as an RLC circuit following the discussion of section 2.2.3. The FPC is modeled as a transformer. The signal generator, and its internal impedance, are assumed to be made visible to the coupler over a matched transmission line.

From basic transmission line theory, the reflection coefficient of a load connected to a transmission line with forward and reverse voltage waves v^+ and v^- will be [Pozar, 1990]

$$\Gamma \equiv \frac{v^+}{v^-} = \frac{1 - Z_0/Z_L}{1 + Z_0/Z_L}$$

In the case of figure 2.5 the load impedance, Z_L, will be the impedance of the transformer and cavity looking in from the Z_0 transmission line. Defining a voltage across the cavity, V_c, and a current flowing into it (directed out from the top terminal of the transformer), I_c, then the cavity impedance will be $Z_c = \frac{V_c}{I_c}$. On the generator side of the transformer the voltage and current (flowing into the top terminal of the transformer) will be $V = V_c/n$ and $I = nI_c$. The impedance looking into the transformer from the transmission line is then $Z_L = \frac{V}{I} = \frac{1}{n^2}Z_c$. Using this in the expression for the reflection coefficient produces a form that is in terms of cavity parameters:

$$\Gamma = \frac{1 - n^2 \frac{Z_0}{Z_c}}{1 + n^2 \frac{Z_0}{Z_c}} \tag{2.29}$$

40

This reflection coefficient will manifest experimentally in measurements of the reflected power and will control how much of the supplied power enters the cavity. Further, it can be linked to the β and Q_e of the coupled cavity system. To see this the impedance of the cavity must be expressed in terms of RLC components of its equivalent circuit

$$\frac{1}{Z_c} = \frac{1}{R + i\omega L} + i\omega C = \frac{R}{R^2 + \omega^2 L^2} + i\left(\omega C - \frac{\omega L}{R^2 + \omega^2 L^2}\right)$$

In this work it is assumed the cavity has a very high quality factor ($Q \gg 1$). From equation 2.14 this indicates that $Q_0 = \frac{1}{R}\sqrt{\frac{L}{C}} \gg 1$. Further assume the cavity is driven near its resonance frequency (equation 2.15), $\omega \approx \frac{1}{\sqrt{LC}}$. These assumptions can be used to simplify the denominator term in the cavity impedance since $\omega^2 L^2 \approx \frac{L}{C} \gg R$. Using these approximations to eliminate the R^2 term in the denominators and factorizing the imaginary term, the impedance is expressed as

$$\frac{1}{Z_c} = \frac{RC}{L} + i\sqrt{\frac{C}{L}}\delta$$

The term δ used here conveys the deviation of the drive frequency from the true resonance frequency of the cavity, ω_r

$$\delta = \frac{\omega}{\omega_r} - \frac{\omega_r}{\omega}$$

Finally, this impedance is used in the impedance ratio term in equation 2.29 to produce

$$n^2\frac{Z_0}{Z_c} = \frac{n^2 R_0 RC}{L} + in^2 R_0 \sqrt{\frac{C}{L}}\delta \tag{2.30}$$

Note that in practice $Z_0 = 50\,\Omega$ so in the above expression it has been replaced with R_0.

With the impedance ratio expressed in this form, it can now be readily linked to the relevant quantities, β and Q_e. These quantities must be derived in terms

41

of the transmission line model parameters. To begin this portion of the analysis, recall from section 2.2.3 that the total stored energy in the cavity can be expressed as either twice that of that of the time-averaged energy of the inductor or capacitor. Consider the energy stored in the capacitance in terms of the voltage across the cavity

$$U = C\bar{V}_c^2$$

The time-averaged power emitted from the cavity in the circuit model can be expressed in terms of V_c as

$$\bar{P}_e = \frac{\bar{V}_c^2}{n^2 R_0}$$

To understand this, consider the case where the signal generator is off. The "signal from amplifier" portion of figure 2.5 will then appear to the coupler-cavity system as a matched load at the end of the transmission line. The entirety of the signal being emitted from the cavity in this model, represented here as V_c/n, will dissipate on this matched load, Z_0. The magnitude of this dissipation depends only on the stored energy in the cavity. So, for a given $\bar{V}_c^2$, this expression will also be valid when the cavity is driven in steady state.

An expression for the external quality factor can be found from the previous two results:

$$Q_e = \frac{\omega U}{\bar{P}_e} = \omega n^2 R_0 C = n^2 R_0 \sqrt{\frac{C}{L}} \tag{2.31}$$

For the last equality, the previously specified assumption that the drive frequency is near the resonance frequency is applied. The coupling factor, $\beta = \frac{Q_0}{Q_e}$, can now be obtained in terms of circuit parameters by combining the quality factor for the RLC circuit given in equation 2.14, $Q_0 = \frac{1}{R}\sqrt{\frac{L}{C}}$, with the external quality factor

$$\beta = \frac{L}{n^2 R_0 R C} \tag{2.32}$$

Finally, the reflection coefficient (equation 2.29) can be expressed in terms of the experimentally relevant β and Q_e. Comparing the expression of $n^2 \frac{Z_0}{Z_c}$ in equation 2.30 with equations 2.31 and 2.32, it is clear that

$$n^2 \frac{Z_0}{Z_c} = \frac{1}{\beta} + iQ_e\delta$$

The reflection coefficient becomes

$$\Gamma = \frac{\beta - 1 - iQ_0\delta}{\beta + 1 + iQ_0\delta} \tag{2.33}$$

In this form the reflection coefficient, which can be measured by information from the power meters indicated in figure 2.4, can be connected to the desired quantity, β.

Connection to measurement

The reflection coefficient can be directly measured by comparing the steady state forward and reverse powers

$$P_r = |\Gamma|^2 P_f = \frac{(\beta - 1)^2 + Q_0^2\delta^2}{(\beta + 1)^2 + Q_0^2\delta^2} P_f \tag{2.34}$$

The last equality follows from equation 2.33. Here P_f and P_r are related to the measured values captured by power meters 1 and 2 in figure 2.4. In addition to the power meter measurement, the cable attenuation between the cavity and the power meter must be obtained. Using these attenuations, the measured power meter value can be adjusted to give the value at the cavity. An important but subtle point to emphasize is that the reflection coefficient calculated in equation 2.33 corresponds to the total reverse power flowing away from the coupler-cavity system. It is a combination of a signal corresponding to the reflection due to the impedance mismatch between the transmission line and the cavity with a

signal emitted from the cavity through the coupler (corresponding to P_e of section 2.3.1). As it is produced by a "reflection" coefficient, it is common to refer to P_r as the "reflected" power. To avoid confusion, P_r will be denoted here only as the reverse power.

The portion of power that enters the cavity will be the difference between the power supplied at the coupler and the reverse power

$$P_{in} = P_f - P_r = \left(1 - |\Gamma|^2\right) P_f = \frac{4\beta}{(\beta + 1)^2 + Q_0^2 \delta^2} P_f$$

The last equality follows from equation 2.33. In the steady state the energy in the cavity is static so all of the power entering will be dissipated in the cavity walls. That is, $P_{in} = P_0 = \frac{\omega U_0}{Q_0}$ in the notation of section 2.3.1. Here U_0 is total stored energy in the steady state. This energy can be expressed in terms of the reflection coefficient and the measured forward power

$$U_0 = \frac{Q_0}{\omega} \left(1 - |\Gamma|^2\right) P_f = \frac{Q_0}{\omega} \frac{4\beta}{(\beta + 1)^2 + Q_0^2 \delta^2} P_f \qquad (2.35)$$

The last equality follows from equation 2.33. U_0 can be employed to extract the field amplitudes in the cavity when combined with geometry-dependent information determined numerically or from the expressions in section 2.2.2. It can also be used to provide a second relation between β and measurable powers. Consider the measurement of the loaded quality factor discussed earlier. Here the signal generator was abruptly shut off after driving the cavity at steady state. A short time after turning off the power, the contribution to the total reverse power due to the impedance-mismatch induced reflected signal will go to zero (practically instantaneous on the scales of high quality factor decay times for microwave frequencies). In this situation, the measured reverse power is determined entirely by that emitted from the cavity, $P_r = P_e$. To obtain the loaded

quality factor, the full decay trace was considered. Here it will be useful to consider only a time shortly after the signal generator is turned off. At this instant, the stored energy will still be approximately U_0. By using the definition of external quality factor, the measured reverse power in this instant can be related to the steady state energy

$$P_e = \frac{\omega}{Q_e} U_0 = \beta \left(1 - |\Gamma|^2 \right) P_f \qquad (2.36)$$

With the understanding that P_e is now considered a measured quantity by utilizing the measurement of reverse power after turning off power.

At this point, β can finally be obtained from measured values.

Extracting β

The phase-locked loop described in section 2.3.2 ensures the cavity is driven close to its resonance frequency. For many situations, the analysis can be simplified by assuming $\omega = \omega_r$. In this case, $\delta = 0$ and equation 2.33 becomes

$$\Gamma = \frac{\beta - 1}{\beta + 1} \qquad (2.37)$$

Using this expression for the reflection coefficient and the previously defined relations between it and measured powers it is possible to extract two independent measurements of β. The agreement of these two β measurements is necessary but not sufficient for indicating a high quality measurement. If the experimental situation is not well-described by figure 2.5, then the derivations that have led to this point could break down and it is possible that the two measurements will coincidentally agree. For a well-designed coupling antenna, this will not be the case and agreement can be a powerful indication of measurement quality.

The first measurement of β will be denoted β_r as it comes from the total reverse power measurement at steady state. This will be derived by combining equation 2.37 with equation 2.34 and solving for β

$$\beta_r = \frac{1 \pm \sqrt{P_r/P_f}}{1 \mp \sqrt{P_r/P_f}} \tag{2.38}$$

The positive and negative roots correspond to the over-coupled ($\beta > 1$) and under-coupled ($\beta < 1$) cases. The type of coupling cannot be determined from the derivation of β_r. To resolve the choice of sign the measurement must be combined from either knowledge from the measurement in the transient case [Padamsee et al., 2008] or by using the second method to more completely obtain β and then choosing the proper case.

The second measurement of β will be denoted as β_e as it comes from the emitted power measured as described in the discussion preceding equation 2.36. Combining this equation with equation 2.37 and solving for β

$$\beta_e = \frac{1}{2\sqrt{P_e/P_f} - 1} \tag{2.39}$$

From this expression, a condition for determining if the system is in the over-coupled or under-coupled case can be found. Specifically, if $P_e/P_f < 1$ then the system is over-coupled and if $P_e/P_f > 1$, then the system is under-coupled.

The preceding expressions for β are often applicable, but in practice there are situations where the assumption that $\delta \approx 0$ cannot be made. By combining equations 2.33, 2.34, and 2.36 it is possible to solve for β and δ in terms of measured values:

$$\beta_\delta = \frac{P_e}{P_f - P_r} \tag{2.40}$$

$$|\delta| = \frac{1}{\omega\tau}\sqrt{\frac{4\beta^2}{(\beta+1)^2}\frac{P_f}{P_e} - 1} \tag{2.41}$$

Here τ is the measured characteristic decay time from the earlier discussion on measuring the loaded quality factor. The β calculated here is given a subscript of δ to remind the reader that it is taken with $\delta \neq 0$. In practice, the main relevance of the β_δ has been producing more reliable high-power data. In this range the quality of the lock can sometimes become less effective, observed as an increase in δ. If the on-resonance assumption is employed in this case, it can lead to reporting unrealistically high RF fields in the cavity. Using β_δ will keep the measured field at a more realistic value. With the exception of the high-power case, the three forms of β given here agree well for the data reported in this text. Due to its more reasonable high-power behavior, β_δ is used for all data presented in this work.

Note that the symbols, P_f, P_r, and P_e, are all denoting the power flow at the junction between the coupler and transmission line in figure 2.5. The power meters report the power after it has attenuated along the cable joining them to the relevant position. As mentioned previously, these attenuations should all be measured and used to adjust the power meter values to their magnitudes at the location of the cavity. These attenuation measurements can be prone to error. Noticing that all of the expressions for β presented here involve ratios of powers, it would be possible to eliminate the attenuation adjustments if all measurements shared the same power meter and RF path. P_r and P_e were explicitly made using power meter 2 in figure 2.4, however, P_f has been indicated to come from power meter 1. If the cavity is driven off resonance, then all of the power is reflected from the cavity. This reverse-traveling signal will be equivalent to the forward power and would be picked up by power meter 2. This measurement is performed after turning off the signal generator to acquire the loaded quality factor. After the signal generator has been off long enough that the stored energy

approaches zero, the signal generator is turned back on with the same power. The generated frequency is set to be satisfactorily far from resonance with the PLL turned off. Recall from section 2.3.2 that modest shifts in frequency are all that is required for the high quality factor cavities to not display any resonant behaviors. Therefore, the required shift in frequency is not large enough to produce significant changes in the frequency-dependent cable attenuation. The resulting measurement will be referred to as the incident power, P_i. At the location of the cavity, it is expected to be equivalent to the forward power, $P_i = P_f$. Because it is measured on the same power meter as P_e and P_r, the attenuated signal that reaches the power meter can be used in the expressions for β in the place of P_f in order to remove the uncertainty from introduced by adjusting the power meter values with measured attenuations.

Surface resistance and magnetic field amplitude

The measurement discussed involves driving the cavity to steady state and then monitoring its decay after turning off the signal generator. The steady state frequency, forward power, reverse power, and transmitted power are collected. The power is then shut off and the decaying reverse and transmitted powers are recorded. From this, the loaded quality factor and coupling factor are extracted. Now the desired results; that is, the surface resistance of the walls of the cavity and the strength of the corresponding surface magnetic field, can finally be found.

The intrinsic quality factor follows immediately from the extracted Q_L and β, using equation 2.22

$$Q_0 = (1 + \beta) Q_L$$

The surface resistance can then be obtained for a given cavity, provided the geometry factor, G (equation 2.12), has been obtained either analytically or by numerical simulation.

$$R_s = \frac{G}{Q_0}$$

Note that this is the average surface resistance relating to the total dissipation over the entire structure. It is possible to obtain rough local surface resistance measurements, but it is an exceedingly difficult task [Knobloch, 1997, Porter, 2021].

The surface field can be obtained for a given cavity energy. In general, the field will be nonuniform over the surface. Typically, the highest field on the structure is of the most interest. The ratio $\frac{B_{peak}}{\sqrt{U}}$ can be obtained either analytically or from numerical simulation. This geometry-dependent value can be combined with the measured steady state energy from equation 2.35

$$B_{peak} = \frac{B_{peak}}{\sqrt{U}}\bigg|_{const} \sqrt{U_0} = \frac{B_{peak}}{\sqrt{U}}\bigg|_{const} \sqrt{\frac{Q_0}{\omega} \frac{4\beta}{(\beta+1)^2 + Q_0^2 \delta^2} P_f}$$

Here P_f is the forward power flowing into the cavity. As was just mentioned in the discussion of extracting β, the measured value at the power meter must be adjusted to account for attenuation between the power meter and the cavity entrance. Unlike the situation for extracting β, there are no ratios of powers that can be used to cancel these attenuations. The room temperature cables and components in the RF path are rated to sufficient powers, so their attenuations are not expected to vary. The portion of the cable that is submerged in liquid helium with the cavity could be of issue, as it is not rated for use in this condition. To account for possible variations in the power attenuation of the submerged cable, the values of P_i and P_f are compared. The attenuation of the submerged

portion of the cable can be extracted from the two measurements by demanding their equality and choosing the attenuation to satisfy this condition. This procedure assumes all room temperature path attenuations are unchanged and that no changes occur in the nature of the cables between the steady state on resonance and off-resonance.

Penetration depth and the surface reactance

The surface resistance and its dependence on surface field magnitude will be the primary interest of this work, but relevant information will also be contained in the surface reactance. Recall from equation 2.8 that the surface reactance is directly proportional to an effective penetration depth that indicates the length scale over which an electromagnetic field will penetrate into the metal surface. This effective penetration depth will change the relevant geometry of the cavity to a volume slightly greater than that of the physical walls. If the effective penetration depth changes, then the resonance frequency will be altered. Information about changes to the penetration depth resulting from material conditions can be obtained by measuring changes to the resonance frequency. These measurements must be supplemented with an analysis attempting to eliminate extrinsic effects such as changes to resonant frequency due to changes in system pressure.

The magnitude of the change of resonant frequency corresponding to a general perturbation of the cavity geometry can be expressed as [Pozar, 1990]

$$\frac{\omega_r' - \omega_r}{\omega_r} \approx \frac{\epsilon_0 \int_{\Delta V} |E|^2 dv - \mu_0 \int_{\Delta V} |H|^2 dv}{4U}$$

Where all quantities represent their average over the RF time period. ω_r and ω_r'

are the resonance frequencies before and after the perturbation and $\Delta V = V' - V$ is the difference between the altered and unaltered volumes. The expression is approximate as the fields are assumed to be unchanged by the perturbation.

The ΔV of interest for this work corresponds to changes in penetration depth. The electric field can be expressed in terms of the magnetic field using the surface impedance: $|E|^2 = |ZH|^2$. For systems with $|Z| \ll 1$, and noting that numerically $\epsilon_0 \ll \mu_0$, the integration of the electric field above can be neglected.

$$\frac{\omega_r' - \omega_r}{\omega_r} \approx -\frac{\mu_0 \int_{\Delta V} |H|^2 dv}{4U}$$

What is meant by the integration of the field magnitude squared over change of effective volume corresponding to a changing penetration depth must be defined. The situation involves changing penetration depths, which are only a characteristic length scale indicating the rate at which the field decays as it enters the surface. The integration over the effective volume including the field in the cavity walls, V_{eff}, will be defined as

$$\int_{V_{eff}} |H|^2 dv = \int_{V_{cav}} |H|^2 dv + \int_A da \int_0^\infty |H_0(z)|^2 \, dz$$

Here V_{cav} is the volume of the cavity determined by the physical barrier, A is the cavity surface area, da is a differential area element, $H_0(z)$ is a function describing the field at the cavity surface and its decay as it progresses into the material, and z is the direction normal to the cavity surface facing away from the cavity interior.

With this definition of the integration over an effective volume, the integration over a resulting change to volume, ΔV, from a perturbation to the penetra-

tion depth (from λ to λ') can be obtained.

$$\int_{\Delta V} |H|^2 dv = \int_{V_{eff'}} |H|^2 dv - \int_{V_{eff}} |H|^2 dv$$

$$= \int_A da \int_0^\infty \left|H'_0(z)\right|^2 dz - \int_A da \int_0^\infty |H_0(z)|^2 dz$$

Here the same notation with a prime denoting the case of the perturbed penetration depth in the material is used.

At this stage literature apparently diverges. Some researchers take a position of minimal information and assume that the field is constant until abruptly vanishing at the penetration depth [Junginger, 2012, Ciovati, 2004]. With this assumption the integration over ΔV yields

$$\int_{\Delta V} |H|^2 dv = (\lambda' - \lambda) \int_A da |H_0(z = 0)|^2 \tag{2.42}$$

Others assume an exponential decay with the characteristic length scale equal to the penetration depth. This would, perhaps, better explain typical superconducting and normal conducting behavior [Gonnella, 2016]. This approach yields

$$\int_{\Delta V} |H|^2 dv = \frac{\lambda' - \lambda}{2} \int_A da |H_0(z = 0)|^2$$

The resulting relation between changes to resonant frequency resulting from penetration depth thus differs in literature by a factor of two. Depending on use, this can lead to significant differences in reported information. In general, the nature of the field decay into the material is not trivial and is not known. For this reason, in the remainder of the text the first case will be employed. In both cases the situation is approximate and based on a perturbation approach and may contain some error regardless of this confusion. Without further effort and information, the error will have to be tolerated.

Proceeding with the integration calculated as in equation 2.42 the relationship between the change in penetration depth and the change in resonance frequency can be combined with the definition of the cavity geometry factor (equation 2.12) and expressed in the final form

$$\lambda' - \lambda = -\frac{G}{\pi \mu f_r^2} (f_r' - f_r) \tag{2.43}$$

This form indicates that if the penetration depth increases, the resonance frequency of the cavity should decrease by an amount dependent upon its geometry.

In practice this method is most commonly applied to study the temperature-dependent changes to the penetration depth near the critical temperature of a superconductor at very low field amplitudes. While the resonance frequency is seen to change systematically as field amplitude is increased, this dependence is not a measurement that is typically considered. The change is thought to be dominated by electromagnetic pressures physically deforming the cavity instead of field-induced changes to the nature of the physical state [Padamsee et al., 2008].

2.4 Summary

In this section the concepts of resonance, electromagnetic cavities, and the use of high quality factor cavities were developed. Each topic was developed in a way that aimed to provide intuition and to highlight subsets of these broad topics that are most relevant for the coming chapters.

The development of the cylindrical TE_{nml} modes and the subsequent defi-

nitions and metrics used to describe resonant cavities will be used in chapter 4 when discussing the design of sample host cavities. The description of the experimental operation of high quality factor resonators for material characterization is that which was used for the measurements and analysis that produce all reported data in chapters 4 and 5.

CHAPTER 3

CALCULATION OF THE SURFACE IMPEDANCE

In section 2.2.1 the concept of surface impedance was defined as a quantity describing the response of a material to an incident electromagnetic plane wave. No information was given about how to calculate the surface impedance for a given material. The purpose of this section will be to demonstrate the calculation of microwave surface impedance for relevant materials.

In this work, the primary focus is microwave resonators with superconducting walls. In general, obtaining the surface impedance of a superconductor is nontrivial and requires input from microscopic models. The process often leads to results that are not intuitive. In this section, a derivation of surface impedance using a simple two-fluid model to describe the electrodynamics of the system will be developed and compared to more robust models in appropriate situations. It will be shown that this relatively intuitive two-fluid model, with appropriate inputs and modifications, agrees well with the more sophisticated models. It is hoped that this demonstration of the superconducting surface impedance will provide some intuition that is lost in most resources.

The cartoon picture of a microwave electromagnetic wave incident on a metallic surface that has been asserted previously in this chapter is presented in figure 3.1. Here an electromagnetic field is traveling along the axis normal to a semi-infinite metallic surface filling the $z > 0$ region. In general, screening currents will be induced at the surface, configuring themselves to prevent the fields from entering into the bulk of the material. The screening currents and fields inside of the material will decay with distance from the surface over some characteristic length scale. As drawn, the fields are in phase with each

other. In general the phase difference will be more complicated and depends on the material properties. The purpose of figure 3.1 is simply to indicate notation and demonstrate the basic nature of the screening currents causing the fields to decay.
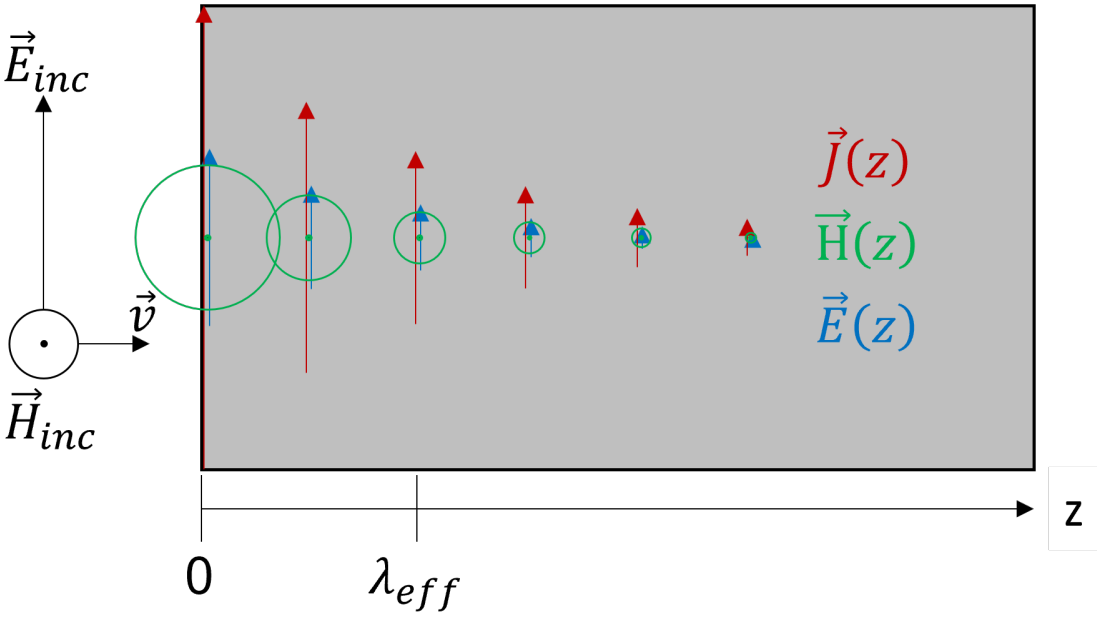
Figure 3.1: Cartoon demonstrating the effect of a microwave electromagnetic field on a metallic surface. Screening currents are induced at the surface that screen the fields from entering into the bulk of the material. The phase difference between the fields is ignored here and depends on the nature of the material.

To calculate the surface impedance, recall its definition given in equation 2.7. To utilize any of the equivalent forms, it is clear that sufficient information about the electric and magnetic fields must be obtained. By combining Maxwell's equations inside the metallic surface, given with SI units, one can obtain a relationship between the electric field and the current density [Walsh and Tomaselli, 1990]

$$E''(z) + \left(\frac{\omega}{c}\right)^2 E(z) = i\omega\mu J(z) \tag{3.1}$$

The displacement current was ignored, which is valid for microwave frequen-

cies in conventional metals. The plane wave is assumed to propagate entirely along the axis normal to the metallic surface and has a time dependence given by $e^{i\omega t}$. If a material-dependent relationship between the current density, J, and the electric field, E, can be obtained, then this equation can be solved to obtain $E(z)$. With the electric field known, the third relationship in equation 2.7 can be used to find the surface impedance as

$$Z = -i\omega\mu_0 \frac{E(0)}{\partial E/\left.\partial z\right|_{z=0}} \tag{3.2}$$

The remainder of this chapter will focus on obtaining $J(E)$ for the case of a normal conductor and a superconductor.

3.1 Surface impedance of a normal conductor

Before discussing the more complicated case of a superconductor, the microwave surface impedance of a normal conducting material is considered. The process used in the normal conducting case, and the obtained results, will readily extend to the calculation for a superconductor. Throughout this section, the microwave frequency range will be considered and approximations, such as neglecting the displacement current, will be used when appropriate.

The most basic relationship between current density and field is that of Ohm's law

$$J(z) = \sigma E(z) \tag{3.3}$$

The conductivity, σ, is a material-dependent quantity describing the electric behavior. Here it will be given by the Drude model, $\sigma = \frac{ne^2\tau}{m}$. n is the density of electrons contributing to the flow of current, e is the electron charge, m is the

mass of the electron, and $\tau = l/v_f$ is the average elastic scattering time. The scattering time will often be expressed in terms of l, the electron mean free path, and the Fermi velocity, v_f [Ashcroft and Mermin, 2021].

Using equation 3.3 in equation 3.1 yields an electric field [Walsh and Tomaselli, 1990]

$$E(z) = E(0) \exp\left(-i\frac{z}{\delta}\right) \exp\left(-\frac{z}{\delta}\right)$$

Here $\delta = \sqrt{\frac{2}{\omega\mu\sigma}}$ is referred to as the skin depth. In this case, the exponential decay demonstrated in figure 3.1 will have characteristic length equal to δ. The phase of the field will vary with z over the same characteristic length. The time-dependence, given by $e^{i\omega t}$, is suppressed.

With the electric field known, it can be used with equation 3.2 to find

$$Z = \sqrt{\frac{\omega\mu}{2\sigma}} \, (1 + i) \tag{3.4}$$

For a normal conductor described by Ohm's law, the microwave surface resistance and reactance are equal. With this relation, the current density at a location is determined entirely by the value of the electric field at that same location. This is referred to as a local current-field relation and will only be valid when the electric field is static over the mean free path of the electron. For very pure materials, where $l > \delta$, this will not be the case and the current-field relation must be refined for accurate surface impedance calculation.

The nonlocal current-field relation, also referred to as the anomalous skin effect, is most intuitively viewed in the form of Chambers/Pippard [Tinkham, 2004]. Here it is expressed following a different notation [Walsh and Tomaselli, 1990]

$$J(z) = \frac{3}{4\pi L} \int_V \sigma E(z) \left(\frac{\exp\left[-\frac{R}{L}\right]}{R^2}\right) \times (\sin\theta \cos\phi)^2 \, d^3\vec{R}$$

L is a length scale indicating the range of influence (for a normal conductor, this will be the electron mean free path). $\vec{R} = \vec{z} - \vec{r}'$, where $\vec{r}'$ points to an arbitrary point in the metal interior. The important piece of this relation is the exponential decay with characteristic length L. This indicates that, when $E(z)$ varies meaningfully on the scale of L, the resulting current-field relation can be different from Ohm's law. Directly using this expression for the nonlocal current-field relation is challenging. To calculate surface impedance including the effects of a nonlocal current-field relation, the procedure of Pippard is followed [Pippard, 1960, Kittel, 1963]. It can be expressed as [Hein et al., 2001]

$$ Z = \frac{i\mu\omega}{\pi} \int_{-\infty}^{\infty} \frac{dq}{q^2 + i\mu\omega\sigma_{NL}(q)} \tag{3.5} $$

With the nonlocal conductivity, σ_{NL}, given by

$$ \sigma_{NL}(q) = \frac{3}{2}\sigma \frac{\left(q'^2 + 1\right)\tan^{-1}(q') - q'}{q'^3} \tag{3.6} $$

With $q' = ql$. q is the wavenumber associated with the Fourier transform of equation 3.1 and l will be the electron mean free path calculated above. The conductivity, σ, is that used to describe the local response. For a typical normal conductor, it would be that given by the Drude model. The calculation is performed assuming specular electron reflection from the surface. The surface impedance calculated with this method offers a decent approximation of the nonlocal electrodynamics observed in a clean system. It will be compared to more sophisticated models later in this chapter when considering the surface impedance of a superconductor.

3.2 Surface impedance of a superconductor

Before calculating the surface impedance of a superconductor, it is required to discuss some details of the superconducting state. The primary application of this work focuses on minimizing dissipation and maximizing obtainable microwave field amplitudes. At the time of this writing, the only materials that are satisfactory for this purpose are referred to as s-wave or conventional superconductors. The discussion here only considers this class of material, though there is some overlap with other types of superconductivity. This discussion is intended only to motivate relevant properties and information required to understand the calculation of surface impedance. Specifically, developing a conductivity that adequately describes the superconducting response. For more careful and complete descriptions of the superconducting state, its properties, and phenomena, the reader should consider more established resources [Mangin and Kahn, 2016, Tinkham, 2004, Kopnin, 2001].

The superconducting state has two major deviations from a normal conducting material. First, it will have a DC resistance identical to zero. That is, it can support a time-invariant flow of charge with no dissipation. Second, it will expel all magnetic flux from its interior. Persistent screening currents will conspire both to remove any magnetic fields present when the material transitions into the superconducting phase and to repel any magnetic fields that may be brought in contact with the superconductor. At a glance, a superconductor appears similar to a "perfect" conductor (one with zero resistivity). Specifically both will possess zero DC resistance and repel magnetic flux. But only a superconductor will remove magnetic flux present in is interior (applied from before its transition into the superconducting state). These effects are abruptly realized

60

when a material is cooled below a certain temperature, referred to as its critical temperature.

The microscopic origin of these superconducting effects is a weak attractive interaction between electrons [Bardeen et al., 1957]. Physically this can be thought of as the attractive interaction between an electron and the positive lattice ions displacing the lattice and causing an effective attraction to the second electron through the lattice. This mechanism of superconductivity is referred to as "phonon-mediated". This attractive interaction can lead to a paired state consisting two electrons of opposite momenta and spin, referred to as Cooper pairs. It turns out that the paired state has lower energy than the Fermi level. At absolute zero and in the absence of other stimuli, the ground state of a system with this weak attractive electron interaction will consist entirely of paired electrons. It can be shown that these Coopers pairs can account for the noted superconducting effects.

In practice, the superconducting ground state cannot be realized due to pair-breaking effects originating from a wide range of sources. Most commonly considered are the effects of thermal excitations from a finite temperature and collisions from a finite current. Electrons from a broken pair, or excitations from the ground state, are referred to as quasiparticles. A superconductor in a practical setting, such as at a finite temperature, will consist of a mixture of paired electrons in the ground state (Cooper pairs) and unpaired electrons (quasiparticles). Making quantitative predictions about the electrical and thermal behaviors of superconductors requires calculating the density of quasiparticles and their energy spectra.

3.2.1 The BCS Hamiltonian

To describe a superconducting system, the Bardeen, Cooper, and Schrieffer (BCS) Hamiltonian is used [Bardeen et al., 1957]. This is a Hamiltonian of a free particle with an extra term accounting for the weak attractive electron interaction (a negative potential). To make this problem solvable it is assumed that the electron-electron attractive interaction is not only weak, but also is independent of the electron momenta, and abruptly drops to zero above a maximum electron energy (the Debye energy is typically used). The BCS Hamiltonian can be used to calculate the properties of a superconductor and its behavior when exposed to various stimuli.

The original solution by BCS is limited to pure superconductors and was not implemented in a modern form [Tinkham, 2004]. Other solution methods have been proposed using different mathematical frameworks and extending the results for practical utility. Anderson extended the BCS results from pure superconductors to include the effects of alloys [Anderson, 1959]. The Bogoliubov-de Gennes method allows for describing superconductors with properties varying on a larger scale than point-like impurities [de Gennes and Pincus, 1966]. The solutions produced by these methods result in two wave functions describing the particle-like and hole-like quasiparticle excitations. Together these wave functions describe the superconducting state. Alternatively, the BCS Hamiltonian can also be solved in terms of Green functions describing the propagation of an electron in time (energy) and space (momentum) [Kopnin, 2001, Belzig et al., 1999]. This approach was used by Gor'kov to provide a powerful framework capable of including both the effects of impurities and inhomogeneous properties [Gor'kov, 1958].

The superconducting energy scales are much smaller than those of the normal conducting phase. This is especially true for the conventional superconductors considered in this work. In the limiting case corresponding to very small superconducting energy scales, an approximate form for the equations of motion of the BCS Hamiltonian can be formulated. This is referred to as the quasiclassical approximation and it can be used to reduce the above methods into more tractable forms [Kopnin, 2001]. The quasiclassical approximation of the Bogoliubov-de Gennes equations is usually referred to as the Andreev equations [Andreev, 1964], though it is sometimes called the WKB approximation [Bardeen et al., 1969]. It reduces the problem from solving two coupled, second-order differential equations with a self-consistency relation to one with only first-order differential equations. Applying the quasiclassical approximation to the Gor'kov approach results in the Eilenberger equations [Eilenberger, 1968]. This can be further approximated to the diffusion-like Usadel equation for systems in the dirty limit (small mean free path compared to the length scale of the electron pairing interaction) [Usadel, 1970].

3.2.2 Quasiparticle excitation spectrum

The properties of a superconductor are now considered deep in the interior of a homogeneous superconductor with no external perturbations other than a finite temperature. The energy of quasiparticle excitations from the ground state, E, relative to the Fermi level, E_f, for a given momentum, p, will be

$$\epsilon = E - E_f = \pm \sqrt{\left(\frac{p^2}{2m} - E_f\right)^2 + |\Delta|^2} \tag{3.7}$$

Where *m* is the effective electron mass and Δ is referred to as the pairing potential. The pairing potential depends on the strength of the attractive force between electrons and will be discussed in the next subsection. In figure 3.2 the form of the excitation spectrum (normalized to the Fermi energy) is presented as a function of the electron momentum normalized to the Fermi momentum. There is a clear gap between the available quasiparticle energies in the superconducting state which results from the pairing interaction. This is referred to as the energy gap. In this case, it will be equal to twice the pairing potential. Note that, while the two are often related, this will not always be the case. The normal conducting (free particle) excitation spectrum is found by setting $\Delta = 0$ in equation 3.7. In this case the energy gap is closed and excitations can take any energy.

3.2.3 The self-consistency equation

The pairing potential, Δ, is obtained in all formalisms by solving for it in a self-consistency equation. In general, this self-consistency equation will take the following form for a homogeneous superconductor with no external or internal stimuli, other than a finite temperature, T.

$$\frac{1}{g} = \int_{|\Delta|}^{E_d} \frac{1}{\sqrt{\epsilon^2 - |\Delta|^2}} \tanh\left(\frac{\epsilon}{2k_B T}\right) d\epsilon \tag{3.8}$$

Here E_d is the Debye energy representing an approximate cut-off energy for the attractive interaction used in the BCS Hamiltonian. $g = N(E_f)V$ is called the interaction constant and is proportional to the strength of the attractive electron interaction in the BCS Hamiltonian, V, and the normal conducting state density of states per spin at the Fermi level, $N(E_f) = \frac{mp_f}{2\pi^2\hbar^3}$.

64
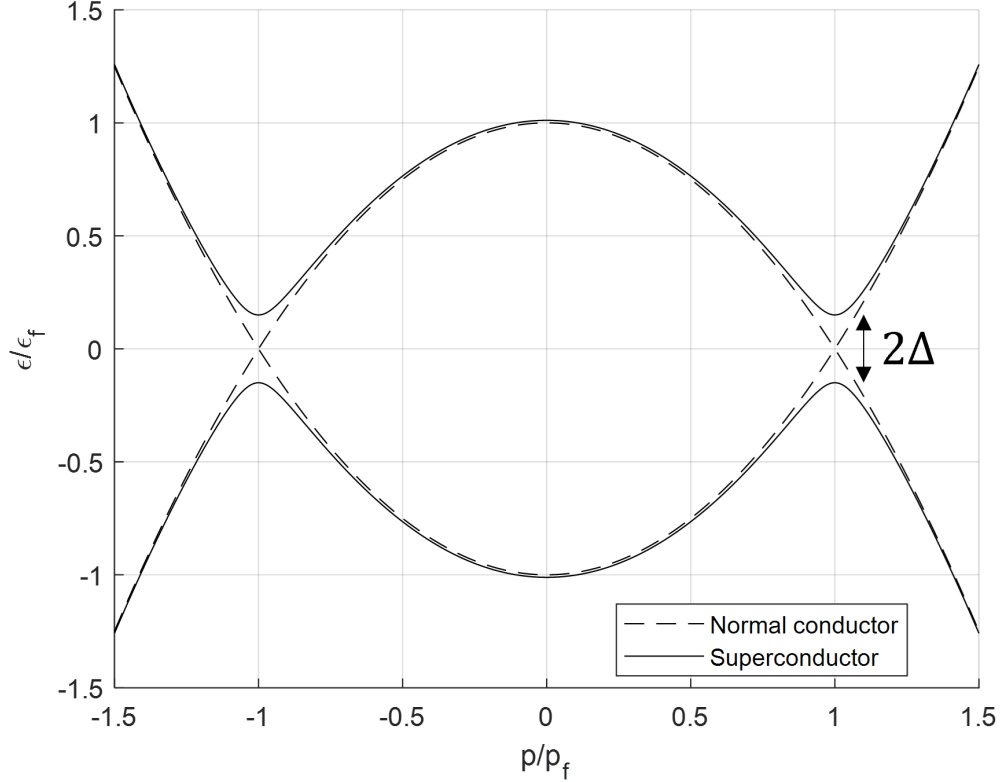
Figure 3.2: Excitation spectra of a normal conductor (dashed) and super con-
ductor (solid) with no intrinsic or extrinsic complications. The su-
perconducting spectrum has a gap of width 2Δ where there are no
available states for unpaired electrons. The superconducting pair
potential is chosen to be $0.15E_f$, which is much higher than typical
s-wave superconductors, in order to visibly demonstrate the energy
gap.

The critical temperature, T_c, that determines the phase transition between
the normal conducting and superconducting states can be estimated from equa-
tion 3.8. The normal conducting limit will be $\Delta = 0$. Plugging this into equation
3.8 and solving for the temperature satisfying the relation yields an estimate for
T_c.

$$T_c \approx 1.13 E_d e^{-1/g}$$

In most situations the critical temperature is readily obtained experimentally,
while the interaction constant is not. Therefore, this expression is often inverted

to use known critical temperatures to estimate the strength of the attractive electron interaction. A major result, referred to as Anderson's theory, is that disorder (introduced from impurities) does not change the superconducting pair potential or critical temperature. At least, to lowest order approximation and in the absence of other effects [de Gennes and Pincus, 1966].

The temperature-dependence of the pair potential is shown in figure 3.3. It moves up from 0 at T_c to a finite value that is relatively constant for temperatures less than approximately half of the critical temperature. This value can be found from equation 3.8 by solving with $T = 0$ and is found to be $\Delta(0) = 1.76 k_B T_c$. For typical s-wave superconductors the critical temperatures are between $1\,\mathrm{K} - 20\,\mathrm{K}$ resulting in $\Delta(0)$ on the order of $1\,\mathrm{meV}$. Compare this to the Fermi energy for typical metals, which is on the order of $1\,\mathrm{eV}$. This is one form of the justification for the quasiclassical approximation discussed previously.

An excellent approximate analytical form for the pair potential temperature dependence is [Linden et al., 1994]

$$\Delta = \Delta(0)\sqrt{\cos\left[\frac{\pi}{2}\left(\frac{T}{T_c}\right)^2\right]}$$

The agreement between this expression and the result from numerically solving the self-consistency equation is shown in figure 3.3.

3.2.4   Quasiparticle and Cooper pair densities

The flux expulsion and zero DC resistance properties of a superconductor require a nonzero density of paired electrons. The Cooper pairs can be broken by events containing energy greater than the energy gap. The absence of a Cooper

pair would result in a quasiparticle excitation from the ground state. At finite temperatures thermal fluctuations become sufficient for breaking pairs. As the temperature increases the number of states occupied by electron pairs will decrease and the number of quasiparticle excitations will increase. This occurs until the critical temperature, T_c, is reached. Here the states available for electron pairing are entirely suppressed by thermal energy and the material becomes a normal conductor.

The flux expulsion property of superconductors involves the creation of screening currents in the material that conspire to eliminate flux from the interior. The strength of the currents must be proportional to that of the applied magnetic fields. Similar to thermal effects, the effect of increasing current will break more Cooper pairs, through collisions. This indicates that at a critical field (current), the superconducting state can no longer exist. From an energy perspective, the superconducting state will exist until it becomes energetically favorable for magnetic fields to enter. For type 1 superconductors, this point marks the transition into the normal conducting phase. For type 2 superconductors, it will be energetically favorable for the material to create domains of normal conducting and superconducting regions. This will be referred to as the mixed state. The normal conducting domains will carry quantized magnetic flux in a normal conducting core. This will be surrounded by a swirling current in the superconducting region [Tinkham, 2004]. As the magnetic field is further increased, the density of these flux vortex regions will increase until the material is entirely normal conducting. In what follows, unless otherwise specified, the superconductor will be assumed to exist in the flux-free Meissner state where no vortices have entered the material.

Ultimately the intent of this discussion is to describe the microwave surface impedance of a superconductor in the Meissner state. As such, describing the number of electrons occupying paired states and quasiparticle states is of interest. Of even greater interest, will be the number of these quasiparticles and paired electrons that directly contribute to the flow of current in the material (analogous to n in the Drude model conductivity). The density of excited quasiparticles that contribute to the flow of electrical current can be obtained as [Deyo et al., 2022, Leggett, 1965]

$$n_q = n \int_{-\infty}^{\infty} \left(-\frac{df(\epsilon)}{d\epsilon} \right) d\xi \qquad (3.9)$$

Where $n = \frac{p_f^3}{3\pi^2 \hbar^3}$ is the total free electron density in the system, f is the energy distribution function of the quasiparticles (it is assumed that the system is in equilibrium and this will be the Fermi distribution), ϵ is the quasiparticle excitation energy relative to the Fermi energy defined in equation 3.7, and $\xi = \frac{p^2}{2m} - E_f = \pm \sqrt{\epsilon^2 - |\Delta|^2}$. This does not describe the total number of quasiparticle excitations in the system. It quantifies only those which contribute to a (small) current. In general, the integral of equation 3.9 must be evaluated numerically. At low temperatures it can be approximated as

$$n_q \approx 8n \exp\left(-\frac{\Delta}{k_B T} \right)$$

In literature, this is often expressed without the numerical factor of 8, which leads to a fairly bad estimate when comparing to experiment or more sophisticated calculations. The author has not derived the factor of 8, but has found this approximates the numerical solution well. The temperature-dependence of the quasiparticle density calculated numerically and with the approximate form are shown in figure 3.3.

Naively, the number density of paired electrons should be $n_p = n - n_q$. In
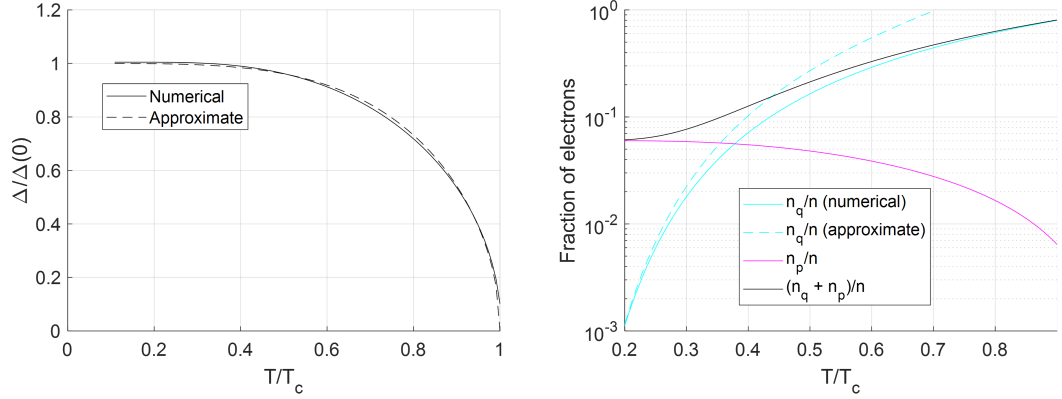
Figure 3.3: (Left) Pairing potential as a function of temperature showing the numerical solution to equation 3.8 and its analytical approximation. (Right) Fraction of electrons occupying quasiparticle and pairing states, $\frac{n_q}{n}$ and $\frac{n_p}{n}$. $n = \frac{p_f^3}{3\pi^2\hbar^3}$. n_q is obtained by preforming the integration in equation 3.9 and is shown next to its analytical low-temperature approximation. n_p is found from equation 3.10. Calculations were performed for a clean system with $l = 1000\,\text{nm}$ and parameters of niobium. $T_c = 9.2\,\text{K}$, $\Delta(0) = 1.76k_BT_c$, $\xi = 40\,\text{nm}$, $E_f = 5.3\,\text{eV}$, and $E_d = (276\,\text{K}) \times k_B$.

the presence of disorder, such as that introduced by impurities in the superconductor, the paired electron density will be further suppressed. The magnitude of this suppression depends on an effective length, $L = \left(\frac{1}{\xi} + \frac{1}{l}\right)^{-1}$ [de Gennes and Pincus, 1966]. l is the electron mean free path which quantifies the range of disorder. ξ is the superconducting coherence length which describes the range of the attractive electron interaction in a clean system. The number of paired electrons contributing to charge transport will be [Lee, 2009]

$$n_p = \left(n - n_q\right) \frac{L}{\hbar v_f} \Delta \qquad (3.10)$$

Here the temperature-dependence of the paired electron density will be determined by the pair potential, Δ, and is demonstrated in figure 3.3. For a more sophisticated consideration of higher temperatures, L should also depend on temperature through the coherence length. Note that L is often referred to as the effective coherence length for a system with impurities, and is the coher-

ence length used in the Pippard form for the nonlocal electromagnetic response
[Tinkham, 2004].

3.2.5 The two-fluid model

The first satisfactory, though phenomenological, explanation of superconduc-
tivity was the London model [London et al., 1935, Mangin and Kahn, 2016].
The London model predicts that the current density of a superconductor in
its ground state (at $T = 0\,\mathrm{K}$) in the presence of an electric field with time-
dependence $e^{i\omega t}$ can be described as

$$J = -i\frac{n_p e^2}{m\omega}E$$

Here e and m are the electron charge and mass. n_p is the number of paired elec-
trons in the system. Note that for a clean superconductor in its ground state all
electrons will be paired, so this could equivalently be thought of as the current
density due to paired electron transport. Notice that this relation is Ohm's law
with a conductivity

$$\sigma_p = -i\frac{n_p e^2}{m\omega}$$

Comparing σ_p to that of the Drude model, $\sigma = \frac{ne^2\tau}{m}$, it is evident that the two
share a similar form. Other than the nature of the states the relevant electrons oc-
cupy, the differences are that the superconducting case is purely imaginary and
the elastic scattering time is replaced with the radiation period. Both changes
are related to the zero DC resistance property observed in superconductors. In
the presence of a time-varying field, the Cooper pairs are not limited by scat-
tering but by the change of inertia induced by the changes to the electric field.
The imaginary conductivity follows from the lossless transport, as will become

evident when calculating the resulting surface impedance.

Proceeding similarly to the normal conducting case, the current-field relation due to the paired electrons from the London model is used in equation 3.1 to obtain the electric field. This will result in

$$E(z) = E(0) \exp\left(-\frac{z}{\lambda_L}\right) \tag{3.11}$$

Where the characteristic length scale, referred to as the London penetration depth, is $\lambda_L = \sqrt{\frac{m}{\mu n_p e^2}}$. Comparing this to the normal conducting case, it is observed that the superconducting case decays purely exponentially without phase oscillation.

Combining this form of the electric field with the surface impedance definition in equation 3.2 results in

$$Z = i\omega\mu\lambda_L$$

The surface impedance of a superconductor where all electrons occupy pairing states is therefore purely imaginary. Recalling from section 2.2.1, the surface resistance corresponds to dissipation. Therefore, the imaginary conductivity results in an electromagnetic response that screens the interior of the material over a length, λ_L, without dissipation.

As was discussed in the preceding subsection, a superconductor will never be in its ground state since finite temperatures will break Cooper pairs. This results in a system where some electrons occupy quasiparticle states and others occupy paired electron states. The two-fluid model approximation treats the system as being comprised of two non-interacting fluids. One occupied by quasiparticles and the other by paired electrons. In the presence of an electric field, the quasiparticle fluid will behave according to equation 3.3 with a similar

conductivity to that of the Drude model, $\sigma = \frac{n_q e^2 \tau}{m}$. Here the modification $n \to n_q$ has been made to indicate that the number of conducting electrons will correspond to the number of quasiparticle excitations. The response of the paired electron fluid will be governed by equation 3.11. The two fluids do not interact, but can carry charge in independent channels. In terms of electromagnetic response, this can be considered as the two being electrically in parallel. The resulting total conductivity will be the sum of the two parallel elements,

$$\sigma = \sigma_q + \sigma_p = \frac{n_q e^2 \tau}{m} - i\frac{n_p e^2}{m\omega} \tag{3.12}$$

This conductivity can be evaluated using the previous results for n_q and n_p from equations 3.9 and 3.10 respectively. The surface impedance with local electrodynamics can be calculated using the same form as before in equation 3.4, but using this complex conductivity.

As given, this expression does not include the nonlocal effects described in the previous section. Correctly including these effects in the superconducting state is possible but leads to complicated and non-intuitive expressions [Mattis and Bardeen, 1958, Abrikosov et al., 1959]. To incorporate nonlocal behavior in this simple model, the approach of Hein is followed [Hein et al., 2001]. In this method it is assumed that the paired electrons obey local electrodynamics while the quasiparticle contribution to the conductivity will be modified according to equation 3.6. The resulting modified conductivity will be used in equation 3.5, noting this was derived for a normal conducting system. While not perfect, this approach approximates the results of more sophisticated models without losing the simple explanations of each contribution and modification. The resulting surface impedance of the two-fluid model with nonlocal effects is expressed as

$$Z = \frac{i\mu\omega}{\pi} \int_{-\infty}^{\infty} \frac{dq}{q^2 + i\mu\omega\sigma(q)} \tag{3.13}$$

With the nonlocal conductivity, $\sigma(q)$ given by

$$\sigma(q) = \frac{3}{2}\sigma_q \frac{\left(q'^2 + 1\right)\tan^{-1}(q') - q'}{q'^3} + i\sigma_p \tag{3.14}$$

σ_q and σ_p are those defined in equation 3.12. As before, $q' = ql$ where q is the Fourier transform variable of z in figure 3.1. Note again, this expression for Z does assume specular electron diffraction from the surface.

The expression for surface resistance in equation 3.13 has lost some of its intuitive advantage, but it should be clear where each of the inputs came from. The form of the integration can be derived from a similar approach used in justifying the local case of equation 3.4 and can be elucidated by examining the resources given in its initial discussion. The details of the superconductor are entirely contained in the conductivity term, $\sigma(q)$. In the form of equation 3.14, the term with q' is another artifact of including nonlocal effects. Other than this, it is simply the intuitive two-fluid model combination which was justified in the discussion leading to equation 3.12. Comparatively, this calculation is easier to compute and more intuitive than the more sophisticated models commonly employed in practice.

Common methods for calculating surface impedance [Mattis and Bardeen, 1958, Abrikosov et al., 1959] are difficult to derive, modify, compute, and the resulting forms lack a clear intuitive understanding. The numerical solutions of these models [Halbritter, 1970, Zimmermann et al., 1991] provide powerful predictions for comparing models and data over a wide parameter-space, but are computationally demanding. Approximate analytical forms do exist in certain parameter ranges, but these forms are not intuitive.

In practice, the metallic surfaces often have inhomogeneities and external

factors which cause them to deviate from the assumptions of these models. A key advantage of a two-fluid model solution is that it presents a relatively basic way of including effects of interest for a given experiment. A common difficulty for the application explored in this work is the need to describe the electromagnetic response of a superconductor to a strong microwave field. This is explicitly outside of the intended range of all existing surface impedance models. Notable attempts to include the effects of large microwave fields have been made for the two-fluid model [Deyo et al., 2022], the Mattis-Bardeen model [Xiao et al., 2013], and, to some extent, the model of Nam [Kubo and Gurevich, 2019]. The interested reader can examine these resources and would see that the inclusion of extra effects is much easier for the two-fluid model. Of course, the more advanced calculations of surface impedance are more robust and accurate than the simple calculation presented here. Exploring to what extent and for what parameter spaces the two-fluid model agrees with these more powerful calculations is of interest.

The low-field surface impedance from the two-fluid model is now compared to the more sophisticated model [Abrikosov et al., 1959] calculated by the numerical routine known as SRIMP (surface resistance with impurities) [Halbritter, 1970]. Calculating the surface impedance requires a large parameter space, independently of model complexity. To reduce the parameter space, this discussion will attempt to compare the two calculations considering parameters that are relatively easily explored in experiments. The easiest inputs to alter are the radiation frequency and the material temperature. The temperature is controlled independently and can be varied continuously. The frequency, depending on measurement method, can be more challenging. In many situations of interest, the measurement of surface resistance requires a resonant cavity. In

this case, obtainable frequencies for a given structure will be discrete. To study frequency dependence, different cavity modes must be used or, if a particular mode is desired, to construct cavities of different shapes and sizes with a given material. The temperature and frequency dependencies of the surface resistance predicted by the two models are presented in figure 3.4. Material parameters are typical values for niobium. The explored ranges are those currently used for particle accelerator cavities, which is the primary interest of this work. Qualitatively, the predicted forms over the explored ranges are in agreement for both frequency and temperature. Good agreement is found for low temperatures across the frequency range explored.
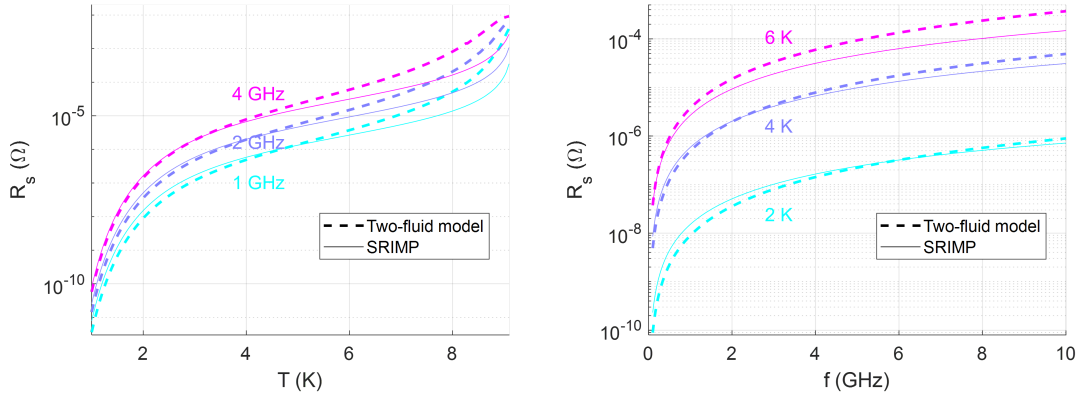
Figure 3.4: Surface resistance calculated from equation 3.13 (dashed line) showing the temperature dependence (left) for a given frequency and frequency dependence (right) for a given temperature. For comparison, the corresponding surface resistance prediction from SRIMP [Halbritter, 1970] is given (solid line). For both models, input parameters corresponding to niobium with a mean free path of 100 nm were used. $T_c = 9.2$ K, $\Delta(0) = 1.76 k_B T_c$, $\xi = 40$ nm, $E_f = 5.3$ eV, and $E_d = (276$ K$) \times k_B$. For the SRIMP calculation, the London penetration depth was specified as 40 nm.

Of the material parameters that contribute to the surface impedance calculation, perhaps the easiest to tune is the electron mean free path. This can be accomplished through alloying the surface with atomic impurities. The com-

parison between the mean-free path dependence of Halbritter's SRIMP and the two-fluid model calculation of surface resistance from equation 3.13 is presented in figure 3.5. The characteristic minimum surface resistance is observed for both calculations. This is due to the effective length used in the paired electron density suppression factor of equation 3.10. For small mean free paths, agreement is seen that is in line with expectations specified previously based on temperature and frequency. The approximations made to extend the two-fluid model to include nonlocal effects lead to discrepancies at very large mean free paths. Comparing the case of the local two-fluid model to the nonlocal calculation, the correction does improve the qualitative behavior, in terms of agreement with SRIMP, and extends what mean free paths can be considered.
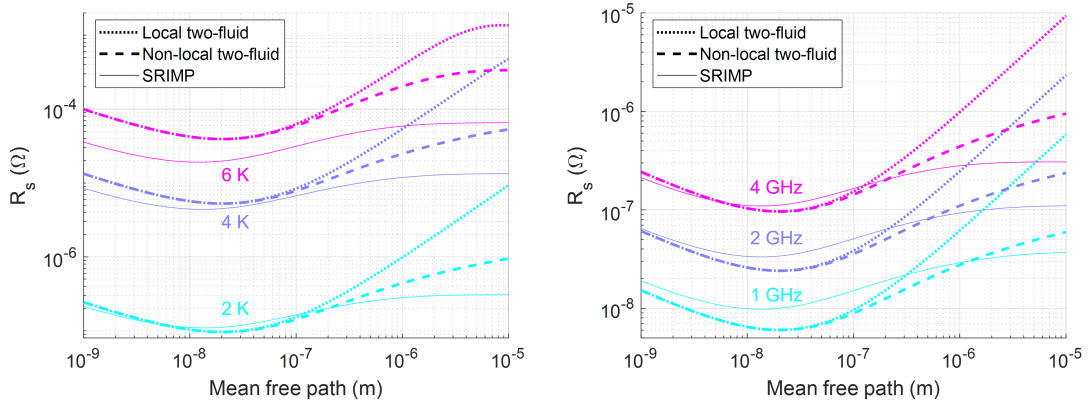
Figure 3.5: Surface resistance dependence on electron mean free path comparing predictions by the two-fluid model with local electrodynamics from equation 3.12 (dotted line), the two-fluid model with nonlocal electrodynamics calculated from equation 3.13 (dashed line), and SRIMP (solid line) [Halbritter, 1970]. Calculations were performed for varying temperature at 4 GHz (left) and frequency at 2 K (right). For all models, input parameters corresponding to niobium were used. T_c = 9.2 K, $\Delta(0)$ = $1.76 k_B T_c$, ξ = 40 nm, E_f = 5.3 eV, and E_d = (276 K)$\times k_B$. For the SRIMP calculation, the London penetration depth was specified as 40 nm.

The surface reactance is more commonly expressed as an effective penetration depth through the relation of equation 2.8. The predictions of penetration

depth from the two-fluid model are compared with those of SRIMP [Halbritter, 1970] in figure 3.6. A common experiment is measuring the change in effective penetration depth while varying temperature. Accordingly, it was chosen to demonstrate the temperature-dependence of the model. For microwave frequencies corresponding to photon energies much less than the gap energy, the penetration depth is not expected to vary significantly. Therefore, it was decided to consider the effect of mean free path over the temperature range, and several curves indicating the effect of varying electron mean free path are included. A rather significant offset exists between the two models. Further adjustment to the result of the two-fluid model may be needed for better agreement. Qualitatively there is a clear difference between the predictions, especially near the critical temperature of 9.2 K. The predictions from the two-fluid model, both in the local and nonlocal cases, approach a maximum value before the critical temperature. The shape and location of this maximum vary with mean free path (and also with frequency). This behavior is often observed in experiments [Bafia et al., 2021, Ormeno et al., 2006]. It is interesting that this qualitative behavior is captured by the two-fluid model, but not with the more sophisticated calculation of SRIMP.

3.3 Further considerations of surface impedance

The surface impedance considered so far has been determined exclusively from the response of a material to an applied field. This does not always provide the full picture for real materials. In practice both the dissipation of electromagnetic energy in the conducting material, as well as the effective penetration depth, can be altered significantly by a variety of effects. As discussed earlier, the incorpo-
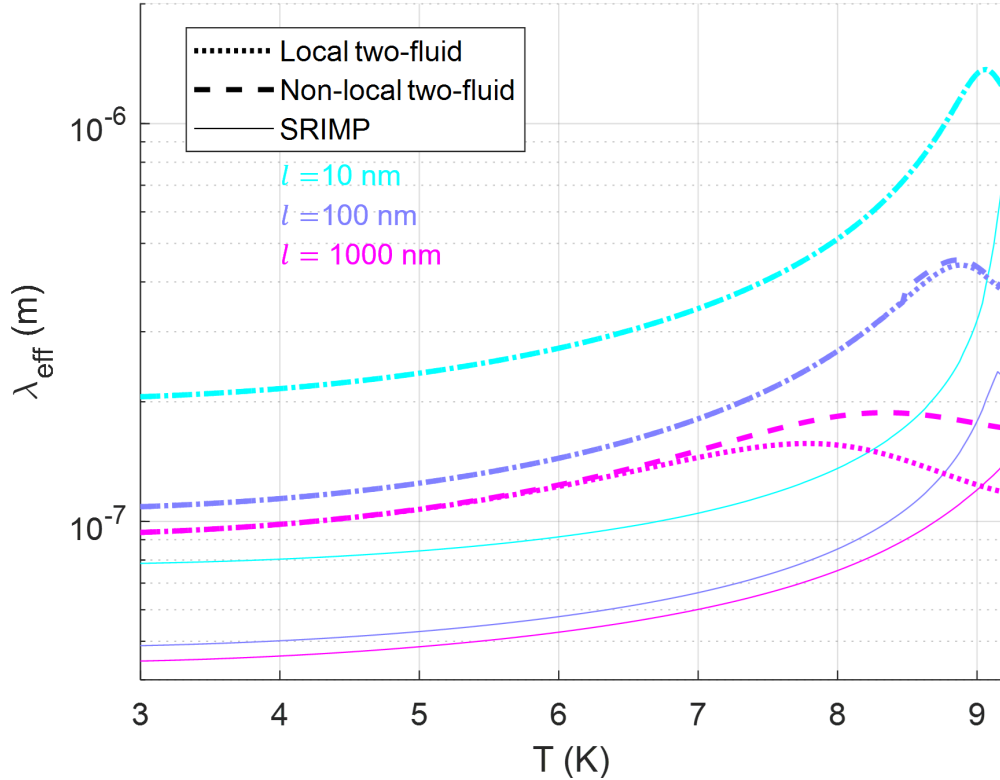
Figure 3.6: Effective penetration depth dependence on temperature comparing predictions by the two-fluid model with local electrodynamics from equation 3.12 (dotted line), the two-fluid model with nonlocal electrodynamics calculated from equation 3.13 (dashed line), and SRIMP (solid line) [Halbritter, 1970]. The effective penetration depth is related to the surface reactance according to equation 2.8. Calculations were performed at 4 GHz. For all models, input parameters corresponding to niobium were used. T_c = 9.2 K, $\Delta(0)$ = $1.76k_B T_c$, ξ = 40 nm, E_f = 5.3 eV, and E_d = (276 K) × k_B. For the SRIMP calculation the London penetration depth was specified as 40 nm.

ration of large field amplitudes can cause a response in the material different from that which has been assumed. Here, collisions from the electrons taking part in the large screening currents with electrons involved in pairing states contain enough energy to break Cooper pairs [Kubo and Gurevich, 2019]. This can lead to a nonequilibrium situation that is difficult to describe efficiently [Kopnin, 2001] and may cause meaningful departure from the surface impedance

calculations of the previous subsections. Regardless of the mechanism, the surface resistance has been found to vary with field amplitude [Padamsee, 2017]. In most cases the variation involves an increase in surface resistance as field increases until an eventual breakdown, referred to as a quench, when the entire surface overheats and transitions into its normal conducting state. In some cases, the surface resistance has been observed to decrease with applied field strength, at least over some field range [Grassellino et al., 2013, Hein, 1999]. This phenomena is referred to as anti-Q-slope within accelerator physics communities and the anomalous field-effect in other fields.

Intrinsic material effects may also be of issue. The models discussed previously, while capable of including point-like impurities, cannot handle larger scales of inhomogeneity. For example, the effects of a native surface oxide can have meaningful impact on measured surface resistance. For relatively high temperature situations it is attributed to normal conducting phases of the surface oxide [Eremeev, 2008]. At lower temperatures it has been proposed that dielectric effects may be relevant [Chiaro et al., 2016]. For multicrystaline surfaces, the grain boundaries can act as Josephson junction weak links causing significant dissipation [Lehner et al., 1999, Sheikhzada and Gurevich, 2017].

The last contribution to surface resistance that will be discussed is that due to trapped flux vortices. Ideally, all flux is expelled from the interior of a superconductor when it is cooled below its critical temperature. In practice, magnetic flux can be pinned by defects in the material and remain inside the superconductor as a flux vortex. It is straightforward to see this structure would be of issue as the normal conducting core would dissipate far more energy than the surrounding superconducting media [Padamsee et al., 2008]. Predictions of dis-

sipation due to trapped flux vortices are often more sophisticated and consider the loss in energy associated with vortices oscillating due to their interaction with time-varying screening currents [Liarte et al., 2018, Gurevich and Ciovati, 2013, Checchin et al., 2018, Checchin and Grassellino, 2020]. This form of dissipation is usually considered to be independent from temperature, which allows it to be distinguished from that of the previous subsection. While trapped flux vortices are often a dominant source, there can be many contributions to the temperature-independent resistance [Padamsee et al., 2008]. A common approximation to assist with analysis is to consider the total resistance of a measurement as being composed of a temperature-dependent part added to a temperature-independent part, $R_{tot} = R_T + R_0$. The temperature-independent contribution, R_0, is referred to as the residual resistance. The temperature-dependent component, R_T, is often dominated by the contribution described in the previous section.

3.4 Summary

In this chapter, a relatively intuitive calculation of surface resistance based on the two-fluid model has been presented. Despite its simplicity, it displays reasonable agreement with more sophisticated models. While this two-fluid model is not rooted in microscopic theories, it may provide a starting point for adding additional features.

Modeling the microwave surface impedance from its various sources is challenging but tractable. The most problematic aspect is comparing these calculations to experiments due to the convoluted effects of many contributing factors

that can be difficult to control. This makes studying surface impedance a difficult task.

In the remainder of this text, attempts are made to aid in the study surface resistance. First, through improving a sample host cavity, it is hoped that a more diverse field of samples can be efficiently examined. By studying a wide range of material properties and features, understanding may be advanced. Second, a surface feature (a native oxide) is replaced with another feature having different properties (gold layer) on a sample that is measured with the sample host cavity. By studying the resulting differences and changing the properties of the gold layer, it makes isolating the role of that specific feature more possible. In other words, this study attempts to decouple one of the many possibly relevant sources of dissipation.

CHAPTER 4

THE CORNELL SAMPLE HOST CAVITY

For decades studies have been carried out exploring the response of super-conductors to strong RF fields. Primarily the goal of these studies has been to improve the technology for accelerator applications. Equally as important, though perhaps taking a secondary role, was to improve the understanding of the fundamental mechanisms and material surface features driving limita-tions and advancements within this field. For metals, this is mathematically described by the surface impedance, which was discussed in chapter 3. This is a complex quantity with the real part describing dissipation of electromagnetic energy in the material and the imaginary part corresponding to the effective-ness of the screening currents in preventing the RF field from entering the bulk of the material. Collecting information about the surface impedance as a func-tion of relevant variables (temperature, frequency, RF field magnitude, DC field strength) for a particular material is known as RF characterization. For accel-erator applications, the most important metrics are the real part of the surface impedance, or surface resistance, and how this quantity depends on the RF field amplitude.

Specifically, the ultimate goal is minimizing the surface resistance to reduce required cooling power (operating cost) at the highest RF field that can be sup-ported in the resonator to reduce the accelerating length required to reach a desired particle energy (cost of construction). The most dramatic feature of the field-dependence is the quench field, defined as the magnetic field ampli-tude at the material surface at which the surface resistance increases sharply. The quench field corresponds to a significant portion of the surface experienc-

ing a phase transition from the superconducting state to the normal conducting state. The purpose of this chapter is to describe an experimental apparatus designed to perform RF characterization for accelerator applications, specifically, to find/improve materials and surface structures for application and probe others to increase scientific understanding.

Niobium has been the standard for superconducting RF (SRF) cavities for accelerators [Padamsee, 2017]. Significant motivation to explore other materials and/or engineer surface features currently exists, as there is reasonable doubt regarding the suitability of niobium for meeting the requirements of future accelerators. The best niobium cavities studied have quench fields near the expected fundamental limits [Grassellino et al., 2018] and it is unclear how much further improvement will be seen. The surface resistance appears to still be improving, especially due to anti-Q-slope effects allowing for tuning the minimum resistance at a given RF field amplitude [Dhakal, 2020, Posen et al., 2020]. While the continued improvement of niobium remains an active field [Valente-Feliciano et al., 2022], it is clear that its ultimate replacement will be required if SRF cavities are to continue to be used for accelerating charged particles.

Even with the discovery of superconductors possessing properties expected to produce lower surface resistances and higher quench fields, niobium has persisted. This is due, in part, to decades of development and optimization of surface preparation processes specifically for niobium [Padamsee, 2017]. However, one can argue that the properties of niobium are very strong for high field application. In general, materials with higher critical temperatures are thought to be desirable. But these materials will also have lower coherence lengths and are therefore possibly more sensitive to smaller and more challenging to control

defects such as grain boundaries [Halbritter, 1995, Sheikhzada and Gurevich, 2017, Kelley et al., 2020, Carlson et al., 2021, Lehner et al., 1999].

Studies of all non-niobium materials, while mostly limited in quantity, support this hypothesis with anomalously high residual resistances and low quench fields compared to niobium [Valente-Feliciano, 2016]. The most successful non-niobium material has been Nb_3Sn, which has shown favorable surface resistance at 4 K but the quench field is limited to less than half of that of niobium [Posen and Hall, 2017]. With the exception of possibly NbTiN and NbN [Keckert et al., 2021], no other candidate materials have been studied extensively. Efficiently and economically growing high quality candidate materials is greatly assisted if one can make use of flat samples. Only a limited number of institutions and systems, including the sample host cavity presented in this chapter, are capable of high RF characterization on flat samples. The lack of systems capable of probing the RF properties of flat samples contributes to the difficulty of understanding and identifying the limiting material features and physical mechanisms required for advancing these materials.

Cylindrical accelerating cavity geometries are an effective test-bed for the RF characterization of niobium and its iterative improvement through trial and error. But this scheme has many drawbacks. The creation of these cavities requires specialized machining tools and expertise, uses excessive amounts of expensive raw material, and reduces accessibility of commercially available material growth tools/techniques. While great technological and scientific progress has been made with these accelerating cavities, it remains that their design and optimization was not for this purpose. It was for accelerating charged particles. While this led to improvements for reaching high field, such as developing ge-

ometries that limit the risk of multipacting [Padamsee et al., 2008], it raises the question: If a system is designed with the specific purpose of performing high field RF characterization can improvements be realized?

It turns out that constructing a system to perform RF characterization on an interchangeable sample (especially a sample with a flat surface) is challenging. Some improvements have been realized such as larger sample temperature ranges, easier thermal cycling, and the option of measuring several frequencies. However, the sample host cavity described in this chapter and other more sophisticated systems all suffer, most notably, from low quench fields as well as questionable measurements. Despite these shortcomings compared to the accelerator cavity measurements, the ability to measure flat interchangeable samples allows for making important and novel measurements using these systems.

This chapter will begin by motivating the design choices made for the Cornell sample host cavity. This involves considering the challenges of high field RF characterization on flat samples, introducing relevant performance metrics for sample host cavities, and then demonstrating the advantages gained from the specific structure of the sample host cavity. Next, a discussion of how sample data is extracted is presented along with a detailed discussion of the uncertainty introduced in this process. This uncertainty will lead to statements about measurement resolution and what limits should be considered when choosing samples suitable for measurement with this system. Improvements made to the system are then presented along with examples of reliable baseline data gathered using the sample host cavity.

4.1 Challenges and methods of flat sample RF characterization

A system capable of performing high-field RF characterization on flat samples with the range and measurement quality of single-material cylindrical resonators has been desired for decades. Unfortunately, there are major barriers at the conceptual, design, and implementation levels preventing many facilities from working with such systems and casting doubt on the results of existing systems. The first major challenge is exposing the sample to sufficiently large amplitude microwave fields. The second is separating the response of the sample of interest from the system as a whole.

For studies supporting accelerator application, the first challenge comes from the large microwave fields produced in accelerator cavities. In niobium cavities continuous wave surface magnetic field amplitudes (as opposed to pulsing the RF signal to let the material cool) above $100\,\text{mT}$ in the GHz range are routinely observed. Therefore, at a minimum flat surface RF characterization systems should be able to produce a field of this order on the flat surface. To the author's knowledge, the only methods by which these surface field magnitudes can be realized with reasonable power supplies are resonators or extremely near-field antennas. The typical approach is a niobium host resonator that produces a strong field at the location of the sample. Using niobium allows for high quality factors which can produce high fields for reasonable input powers, but creates a limitation as the field on the niobium surfaces will eventually exceed its quench field.

Only the sample host cavity discussed in this chapter and one other superconducting resonator-based sample measurement system have reached this

value [Keckert et al., 2021], though both are expected to be limited to a field range lower than typical accelerating cavities. The issue largely results from the necessity of attaching a sample to an overall resonator structure. The disruption, caused by the flange to the overall resonator structure, typically leads to enhancement elsewhere on the host structure. The sample-to-host structure flange must also be designed in a way that the RF fields do not drive currents through the flange and must shield any edges from the RF fields to prevent spurious dissipation or issues with field-enhancement causing quench. Currently the limited maximum field capability is not a huge issue since no material other than niobium has reached a quench field exceeding $100\,\text{mT}$ (except for Nb_3Sn recently Posen et al. [2021]), but this could pose a major challenge in the future. Some systems have been developed that bypass this issue, such as a copper host cavity developed at SLAC [Guo et al., 2013] and a non-resonant microwave microscope that essentially positions a current carrying loop $\sim 100\,\text{nm}$ from the sample surface [Tai, 2013, Oripov et al., 2019].

The second challenge is separating relevant metrics from the rest of the system. For the typical niobium host resonators described in the previous paragraph, the goal is to measure the sample surface resistance which corresponds to dissipation of the RF fields on the sample. It is easy to obtain the total dissipation in a resonator as a whole, but this includes the losses in the host structure. The simplest method to extract sample resistance is to perform this total dissipation measurement for a sample of interest and then compare it to a separate calibration measurement in order to eliminate the contribution from the host structure. The calibration measurement uses a sample where the surface resistance is assumed to be known. This method will be referred to as a calibrated quality factor measurement for the rest of this text.

In practice this imposes severe limitations on measurement accuracy especially for samples desired for accelerator applications aiming for lower surface resistance than niobium. A more sophisticated approach is a calorimetric measurement in which the heating of the sample is directly measured. This has been demonstrated to be effective for accelerator interests, allowing for probing higher temperatures and providing high resolution measurement, but is difficult to design and implement successfully [Keckert et al., 2021]. Further, it typically limits users to pulsed operation. Most troubling is that the measurements produced by this method have not agreed with standard accelerator cavity measurements [Keckert et al., 2017].

The discussion of high-field RF characterization systems for flat samples presented here is intended only to motivate and present concepts required for later in the text. For more details see general reviews [Oseroff et al., 2021, Goudket et al., 2016] and specific texts on near-field antenna - resonator hybrids (quadrupole resonators) using calorimetric measurements [Keckert et al., 2021, Junginger, 2012, Kleindienst, 2017, Keckert, 2019].

4.2 Design parameters of sample host systems

In this section a list is presented defining parameters and explaining their relevance to the Cornell sample host cavity. In the language of the previous section this is a sample RF characterization system that utilizes a niobium sample host resonator for reaching high RF fields on the sample and employs a calibrated quality factor measurement to obtain sample surface resistance.

<u>Peak field ratio</u>: $\frac{B_{pk,plate}}{B_{pk,host}}$. As described in the previous section the maximum

field that can be realized on the sample is one of the key measures by which a sample host system is judged. For a niobium host cavity, the highest field that can be reached on the sample will ultimately be limited by when a quench field is reached somewhere on the niobium host structure. This parameter describes the ratio of the maximum field on the sample surface to the maximum field on the host structure. Increasing this ratio allows for higher possible fields on the sample and it is therefore a key design feature of any sample host cavity.

Focusing factor: $\alpha = \frac{\int_{\text{plate}} |\mathbf{H}|^2 d\mathbf{S}}{\int_{\text{plate}} |\mathbf{H}|^2 d\mathbf{S} + \int_{\text{host}} |\mathbf{H}|^2 d\mathbf{S}}$. This parameter describes how much of the total surface field is focused onto the sample as opposed to the host structure. As will be seen in the following sections, this parameter is essential for minimizing the uncertainty of the reported sample surface resistance for a calibrated quality factor measurement. The impact of measurement uncertainty on the extracted sample surface resistance from a calibrated quality factor measurement can be extremely problematic for many samples of interest. Therefore, a design that maximizes the focusing factor (that is, focusing more of the field on to the sample) is desirable and will allow for measurement of samples with lower surface resistances.

Filling factor: $\frac{B_{pk,host}}{\sqrt{U}}$. The electromagnetic fields in a resonator are proportional to the square root of the stored energy, U. This parameter conveys the magnitude of a surface magnetic field for a given amount of stored energy. Because the energy stored in a driven resonator is determined by the input power, this parameter can be used to calculate expected amplifier power requirements for the system.

Geometry factor: G. The geometry factor, similar in this context to the filling factor, is relevant for understanding amplifier power requirements. A higher

geometry factor will lead to a higher quality factor for a given surface resistance. The higher the quality factor the more stored energy can be reached for a given input power.

Sample size & operating frequencies. The sample should be kept at a size that allows for utilizing commercially available systems and facilities for material depositions and alternative surface characterization. In general, this means a smaller sample is desirable. The operating frequencies should be close to those used in accelerators (0.1 GHz – 1.5 GHz ideally). Depending on the excitation method, this can be problematic in different ways. For TE_{01n} mode resonators, samples can be made as thin disks but the sample diameter for typical end-plate replacement configurations (see figure 4.1) will determine the frequency. Thus, keeping a frequency near the desired range would require a prohibitively large sample and often systems using this excitation method operate at somewhat increased frequencies.

Other important considerations include the range of operating temperature and frequencies. For resonant systems, at best only a discrete range of frequencies will be available.

4.3   Design of the Cornell Sample host cavity

The current iteration of the Cornell sample host cavity is a fine grain niobium structure designed to operate in TE_{011}-like and TE_{012}-like modes at 4 GHz and 5.2 GHz respectively. A 5″ diameter sample disk is affixed to the top of the host structure to close the volume and complete the resonant structure demonstrated in figure 4.1. The frequencies and sample size are inversely related and

were chosen as a compromise between reasonably low frequencies (similar to accelerator application) and maintaining a somewhat manageable sample size. The small port at the bottom of the cavity is for the coupling antenna and connection to vacuum systems. The port coming out of the side is for a transmitted power probe. The TE_{01n} mode is advantageous for sample studies for a number of reasons. The component of surface electric fields normal to the surface is very small, which reduces the threat of field emission. The screening currents induced are not expected to be driven through the sample-host flange, which can be a spurious source of dissipation. The magnetic field on the sample is essentially unchanged for small values of n, which allows for probing the same features of a given sample at different frequencies. Notice that the field is not uniform over the area of the sample. In the results following in this chapter and the remainder of this text, any results referencing the RF field strength on a sample will do so from its maximum value.

The host cavity shape is designed to achieve the highest possible magnetic field on the sample compared to the host structure. The original design and implementation were done by Daniel Hall [Hall et al., 2013, 2014a,b], improving its performance beyond the preceding versions [Xie, 2012]. A conceptual explanation of how an end-plate replacement sample host cavity geometry designed for calibrated quality factor measurement is optimized is given in figure 4.2. Here in what is essentially an exact TE_{011} mode of a cylindrical cavity, the energy is mostly stored far from the top (location of the sample plate) in the center of the volume. If the top half of the cylinder is altered to have a larger diameter than the lower half, then this electromagnetic energy will be forced upward towards the sample location. This effect is beneficial for key metrics of a sample host cavity. Specifically, the ratio of peak sample field to peak host field and the
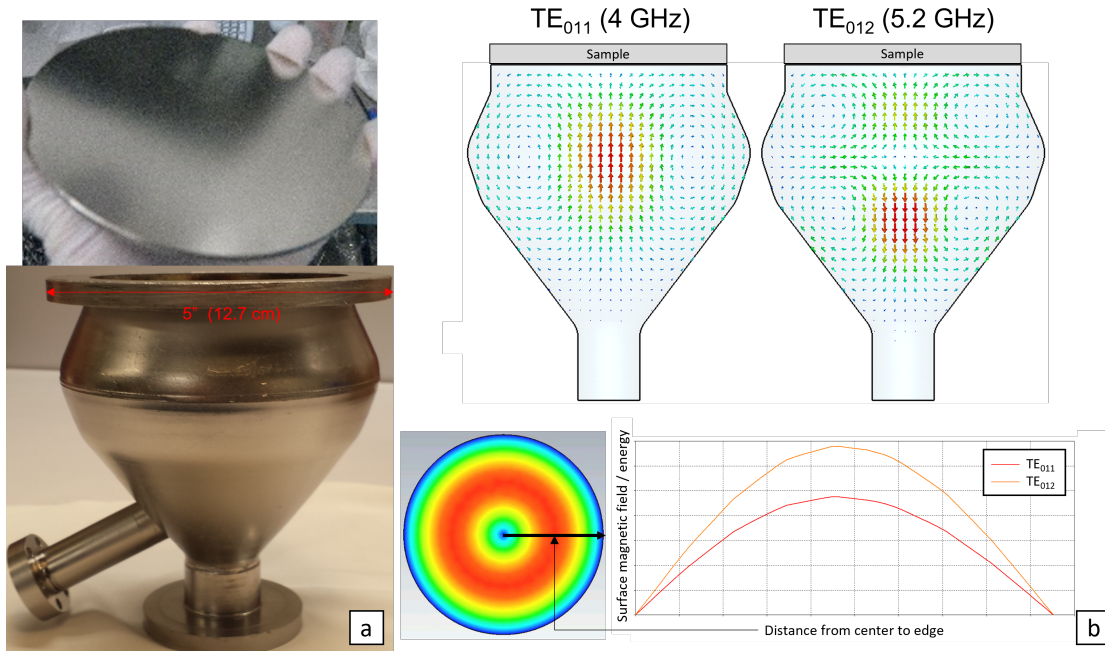
Figure 4.1: (a) Cornell sample host cavity with a niobium calibration plate. Both are made from fine grain niobium, electropolished, and baked at $800°$ C for 5 hours in vacuum. (b) Top: cross-sectional magnetic field configurations for the operating modes. Bottom: Magnetic field amplitude projected on sample plate demonstrating the uniform sample excitation between the two modes. The right figure corresponds to the projection onto the black line to demonstrate identical profiles.

focusing factor, described in section 4.1, will benefit since the energy is more focused onto the sample. The improvement occurs until a maximum value is reached. The onset of the detrimental effects is caused by enhancement of the field at the strong bend in the host structure mirroring the position of the plate. While the energy is more focused to the upper segment, this bend-induced enhancement of the field means the contributions of the field to the host surface become more significant than those on the sample.

The first version and second version of this sample host cavity were essentially a cylinder and a mushroom-shape, corresponding to either end of the non-optimal extremes of the parameter x in figure 4.2. With this third version, the
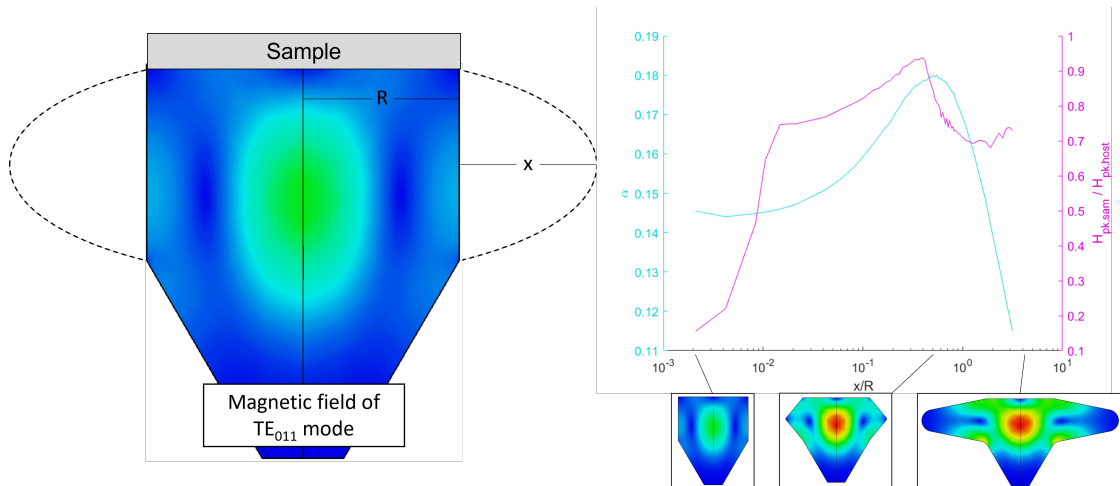
Figure 4.2: Demonstration of sample host cavity design parameter optimization for an end-plate replacement style TE_{011} mode resonator. The figure on the left shows the magnetic field magnitude of a TE_{011} mode pill-box cavity (ignoring the tapered bottom). Extending the radius of the upper portion of the resonator near the sample by an amount, x, pushes the electromagnetic energy upward towards the sample. The plot on the right demonstrates the impact of changing x normalized to the original cylinder radius, R, on the focusing factor, α, and the peak sample to peak host field ratio.

field limit is improved over its predecessors as expected. The result ideally allows for exploring as wide a range of field magnitudes as possible before being limited by the niobium quench field of the host structure. In practice, the quench field is lower than expected from standard accelerating cavity tests. The highest sample fields observed are $105\,\mathrm{mT}$ and $65\,\mathrm{mT}$ for $4.0\,\mathrm{GHz}$ and $5.2\,\mathrm{GHz}$ respectively. Compare this to standard accelerating niobium cavities which can routinely reach surface fields far exceeding $100\,\mathrm{mT}$. It should be noted that this sample host cavity operates at a higher frequency than typical accelerating cavities, and surface heating will become problematic at lower fields [Xie, 2012].

The parameters of the sample host cavity were calculated using CST Microwave Studios and are given in table 4.1.

	TE_{011}	TE_{012}
$\frac{B_{pk,plate}}{B_{pk,host}}$	0.91	0.96
α	0.13	0.25
$B_{pk,host}/\sqrt{U}$ $\left[mT/\sqrt{J}\right]$	69.3	94.2
G [Ω]	801	993
frequency [GHz]	3.99	5.27
Maximum sample field [mT]	105	65
sample size [cm]	12.7	

Table 4.1: Cornell sample host cavity parameters calculated from results of a CST Microwave Studios simulation. Parameters are defined and described in section 4.2. Note that in practice the TE_{012} mode is typically measured to be 5.23 GHz. The maximum sample field is obtained from measurement not simulation.

4.4   System resolution and limitations

The Cornell sample host cavity employs a calibrated quality factor to extract the desired sample surface resistance from the total dissipation measured. In this section, the procedure used for this process is derived. The propagated systematic and statistical uncertainties resulting from the process are then derived. From both forms of uncertainty, it is clear that this method of sample surface resistance measurement fails as the sample resistance becomes less than that of the host structure. While no exact resolution can be given for the system, it is possible to use the quantified uncertainties to comment on what sample resistance ranges may be measurable with an acceptable level of uncertainty.

4.4.1   Extracting sample surface resistance

The Cornell sample host cavity employs a calibrated quality factor measurement to decouple sample surface resistance from the total response of the sys-

tem. The procedure involves two separate measurements, two key assumptions, and knowledge of the field distribution on the the host and sample plate. The first measurement is a calibration, where the quality factor of the resonator with a sample plate with identical preparation to the host structure is obtained. It is assumed that the surface resistance of this calibration plate is identical to that of the host structure. The second is a sample measurement, where the sample plate is the sample of interest with unknown surface resistance. It is assumed that the dissipation that occurs on the host structure is unchanged between these two measurements. In this section, quantities corresponding to the calibration and sample measurements will have superscript "cal" and "sam" respectively. Subscripts will identify the location of a quantity where applicable, such as the dissipation on the host or plate portions of the sample host cavity.

From the definition of intrinsic quality factor, the measured intrinsic quality factor of the sample measurement will be

$$Q_0^{sam} = \frac{\omega U}{P_{total}^{sam}}$$

Here ω is the angular frequency and U is the energy of the resonator. Notice no superscript is used for the stored energy since it is assumed the calibration procedure will be carried out at a specific RF field amplitude on both measurements so that $U = U^{sam} = U^{cal}$. The total power dissipated in the system, $P_{total}^{sam} = P_{host}^{sam} + P_{plate}^{sam} + \sum_i P_i^{sam}$ has contributions from the surface of the host structure, the sample plate, and any other sources of dissipation in the system denoted here with a subscript i. Combining these expressions relates the measured quality factor with the sample plate to all possible sources of dissipation:

$$\frac{1}{Q_0^{sam}} = \frac{1}{\omega U} \left(P_{host}^{sam} + P_{plate}^{sam} + P_{other}^{sam} \right) \tag{4.1}$$

Now the dissipation on the host structure must be eliminated using the mea-

sured quality factor with the calibration plate, Q_0^{cal}. In expressions relating the resistance to dissipated power on a surface, the resistance is assumed to be an average over the entire surface which ignores any dependence it may have on the field so it can be removed from the integration. This is not ideal, as in practice the resistance does depend on field and the field is non-uniform over all surfaces of the resonator. The dissipation on the host structure will ultimately be assumed equivalent between the two measurements but in the following expression a term ΔP_{host} is introduced to account for any mismatch that could occur.

$$P_{host}^{sam} = P_{host}^{cal} + \Delta P_{host} = \frac{1}{2} R_{host}^{cal} \int_{host} |H|^2 dS + \Delta P_{host} \tag{4.2}$$

If the surface resistance of the calibration plate is known, then P_{host}^{cal} can be related to the total dissipation in the resonator system (and therefore to the measured quality factor Q_0^{cal}) using the cavity parameters in table 4.1. Specifically, the surface resistance of the calibration plate is expected to be to that of the host structure since they have identical preparation. ΔR_{plate}^{cal} is introduced to account for any possible deviations that could occur. As before, note that the resistances are averaged over the relevant surface. The calibration plate resistance will then be expressed as $R_{plate}^{cal} = R_{host}^{cal} + \Delta R_{plate}^{cal}$. Anticipating the difference between calibration resistance and the host structure being small, the subscript "host" will be dropped: $R^{cal} = R_{host}^{cal}$. The total dissipated power in the calibration measurement can now be expressed as

$$P_{total}^{cal} = \frac{1}{2} R^{cal} \int_{plate} |H|^2 dS + \frac{1}{2} R^{cal} \int_{host} |H|^2 dS + P_{\Delta R_{plate}}^{cal} + P_{other}^{cal}$$

Here two extra terms are included. $P_{\Delta R_{plate}}^{cal} = \frac{1}{2} \Delta R^{cal} \int_{plate} |H|^2 dS$ which accounts for dissipation ignored in the assumption that the averaged resistance on the calibration plate is the same as that on the host structure. P_{other}^{cal} represents the

sum of all spurious losses in the system. This expression for total dissipation in the calibration measurement can be related to the dissipation on the host structure.

$$P_{host}^{cal} = \frac{P_{host}^{cal}}{P_{total}^{cal}} P_{total}^{cal} = \frac{\frac{1}{2}R^{cal}\int_{host}|H|^2 dS}{\frac{1}{2}R^{cal}\int_{plate}|H|^2 dS + \frac{1}{2}R^{cal}\int_{host}|H|^2 dS + P_{\Delta R_{plate}}^{cal} + P_{other}^{cal}} P_{total}^{cal}$$

Expressing the field integrals in terms of the focusing factor and replacing the total dissipation of the system with the measured intrinsic quality factor, $Q_0^{cal} = \frac{\omega U}{P_{total}^{cal}}$

$$P_{host}^{cal} = \left(\frac{1}{1-\alpha} + \frac{P_{\Delta R_{plate}}^{cal}}{P_{host}^{cal}} + \frac{P_{other}^{cal}}{P_{host}^{cal}} \right)^{-1} \frac{\omega U}{Q_0^{cal}} \tag{4.3}$$

Combining equations 4.1, 4.2, and 4.3 the measured intrinsic quality factor with the sample plate can be related to the measured intrinsic quality factor of the calibration, numerically obtained cavity parameters, and spurious dissipation factors that will later be neglected.

$$\frac{1}{Q_0^{sam}} = \left(\frac{1}{1-\alpha} + \frac{P_{\Delta R_{plate}}^{cal}}{P_{host}^{cal}} + \frac{P_{other}^{cal}}{P_{host}^{cal}} \right)^{-1} \frac{1}{Q_0^{cal}} + \frac{\Delta P_{host}}{\omega U} + \frac{\frac{1}{2}R_{plate}^{sam}\int_{plate}|H|^2 dS}{\omega U} + \frac{P_{other}^{sam}}{\omega U}$$

Recall the definition of the geometry factor, G, from chapter 2: $Q = G/R = \omega U/P = \left(\frac{\omega U}{\frac{1}{2}\int_S |H|^2 dS} \right) \frac{1}{R}$. So $G = \frac{\omega U}{\frac{1}{2}\int_S |H|^2 dS}$. The term corresponding to dissipation in the sample plate can be related to the geometry factor by using the focusing factor to change the integration in the numerator

$$\frac{1}{Q_0^{sam}} = \left(\frac{1}{1-\alpha} + \frac{P_{\Delta R_{plate}}^{cal}}{P_{host}^{cal}} + \frac{P_{other}^{cal}}{P_{host}^{cal}} \right)^{-1} \frac{1}{Q_0^{cal}} + \frac{\Delta P_{host}}{\omega U} + \frac{\alpha}{G}R_{plate}^{sam} + \frac{P_{other}^{sam}}{\omega U}$$

After multiplying both sides by $Q_0^{cal} = \frac{\omega U}{P_{total}^{cal}}$ to express the sources of spurious dissipation in terms of their ratio to a source of expected dissipation and solving for the desired sample resistance, the final form is obtained:

$$R_{plate}^{sam} = \frac{1}{\alpha}\frac{G}{Q_0^{cal}}\left[\frac{Q_0^{cal}}{Q_0^{sam}} - \left(\frac{1}{1-\alpha} + \frac{P_{\Delta R_{plate}}^{cal}}{P_{host}^{cal}} + \frac{P_{other}^{cal}}{P_{host}^{cal}} \right)^{-1} - \frac{\Delta P_{host}}{P_{total}^{cal}} - \frac{P_{other}^{sam}}{P_{total}^{cal}} \right] \tag{4.4}$$

It is difficult or impossible to completely obtain measurements or estimates for the spurious contributions in this equation. To proceed with the extraction in practice, $P_{\Delta R_{plate}}$, P^{cal}_{other}, ΔP_{host}, and P^{sam}_{other} are assumed to be negligible. The resulting approximate form of equation 4.4 is used instead

$$R^{sam}_{plate} = \frac{G}{\alpha} \left[\frac{1}{Q^{sam}_0} - (1 - \alpha) \frac{1}{Q^{cal}_0} \right] \tag{4.5}$$

4.4.2 Statistical uncertainty

The measurement of quality factor, detailed in chapter 2, takes on uncertainty from the power meter data used to extract β and the fit to the power decay used to extract the decay constant. The uncertainty of the sample resistance, denoted σ_R, is found by propagating the uncertainty of the measured quality factors in the calibration and sample measurements through the expression for sample surface resistance given in equation 4.5.

$$\sigma_R = \frac{G}{\alpha} \sqrt{ \left(\frac{1}{Q^{sam}_0} \right)^4 \sigma^2_{Q^{sam}_0} + (1 - \alpha)^2 \left(\frac{1}{Q^{cal}_0} \right)^4 \sigma^2_{Q^{cal}_0} }$$

In practice, what matters is the fractional uncertainty in the quality factor, which tends to range from 1% to 10%. The fractional uncertainty seems to be independent from quality factor magnitude. To simplify the subsequent analysis, the fractional uncertainty of the calibration and sample measurements is assumed to be identical: $\frac{\sigma_{Q_0}}{Q_0} = \frac{\sigma_{Q^{cal}_0}}{Q^{cal}_0} = \frac{\sigma_{Q^{sam}_0}}{Q^{sam}_0}$. Expressing the uncertainty in the extracted sample resistance in terms of the fractional measurement uncertainty yields

$$\sigma_R = \frac{G}{\alpha} \sqrt{ \left(\frac{1}{Q^{sam}_0} \right)^2 + (1 - \alpha)^2 \left(\frac{1}{Q^{cal}_0} \right)^2 } \left(\frac{\sigma_{Q_0}}{Q_0} \right)$$

Now consider the fractional error of the sample surface resistance

$$\frac{\sigma_R}{R^{sam}} = \frac{\sqrt{\left(\frac{Q_0^{cal}}{Q_0^{sam}}\right)^2 + (1-\alpha)^2}}{\frac{Q_0^{cal}}{Q_0^{sam}} - (1-\alpha)} \left(\frac{\sigma_{Q_0}}{Q_0}\right) \tag{4.6}$$

Notice that there is a pole in the denominator, which can lead to infinite fractional uncertainty. This pole can be explained by understanding that the quality factor of the sample measurement would be limited to a maximum finite value corresponding to zero dissipation on the sample. In this imaginary case, the quality factor would be determined entirely from the dissipation of the niobium host structure, $\max\left(Q_0^{sam}\right) = \frac{Q_0^{cal}}{1-\alpha}$. Because the measured quality factor will approach a horizontal asymptote as the sample resistance decreases, any deviations from the true value occurring in the measurement will produce larger deviations in the extracted sample resistance.

It is useful to express the ratio of the two measured quality factors as a ratio of sample resistance to the calibration resistance. This will result in an equation giving the uncertainty of the extracted sample resistance for a given sample surface resistance and quality factor measurement error, and is the best method for conveying measurement resolution for this system.

From equation 4.5 and ignoring the spurious sources of dissipation such that $R^{cal} \approx G/Q_0^{cal}$, the ratio of calibration to sample measurement quality factors can be related to the ratio of the sample to calibration surface resistances

$$\frac{Q_0^{cal}}{Q_0^{sam}} = \alpha\frac{R^{sam}}{R^{cal}} + (1-\alpha)$$

Inserting this expression into equation 4.6:

$$\frac{\sigma_R}{R^{sam}} = \frac{\sqrt{\left(\alpha\frac{R^{sam}}{R^{cal}} + (1-\alpha)\right)^2 + (1-\alpha)^2}}{\alpha\frac{R^{sam}}{R^{cal}}} \left(\frac{\sigma_{Q_0}}{Q_0}\right) \tag{4.7}$$

99

The fractional uncertainty diverges as a sample surface resistance becomes small. The resolution of a sample host cavity using a calibrated quality factor measurement cannot be described by a single value but depends on the ratio of surface resistances of the sample and host structure as well as the focusing factor. One should be mindful of this equation when determining what samples are measurable with this system for a given purpose, since small surface resistance samples will not be measured accurately. Figure 4.3 demonstrates this conclusion about the limits of observed measurement uncertainties for a range of sample resistances.

4.4.3 Systematic uncertainty

As discussed in the section 4.4.1, the expression used to separate the sample surface resistance from the total response of the resonator neglects potentially relevant sources of dissipation, which results in error. How much of an impact these sources can have on the sample surface resistance reported by equation 4.5 is not immediately clear and the exact values of these sources cannot always be measured, though specific contributions could be estimated. To illuminate this, consider the difference between equations 4.4 and 4.5, $\Delta R^{sys} = R_{plate}^{sam} - \left(R_{plate}^{sam}\right)_{approx}$, normalized by the approximate expression for sample surface resistance. This can be expressed in a form that demonstrates how different contributions will have different scaling factors on their contribution to the systematic error. The desired form expresses the dissipation due to these sources relative to the total dissipation in the calibration measurement, in order to demonstrate the impact a spurious source of dissipation could have on the measurement for an assumed value relative to a measured quantity. It can be shown from previous expres-
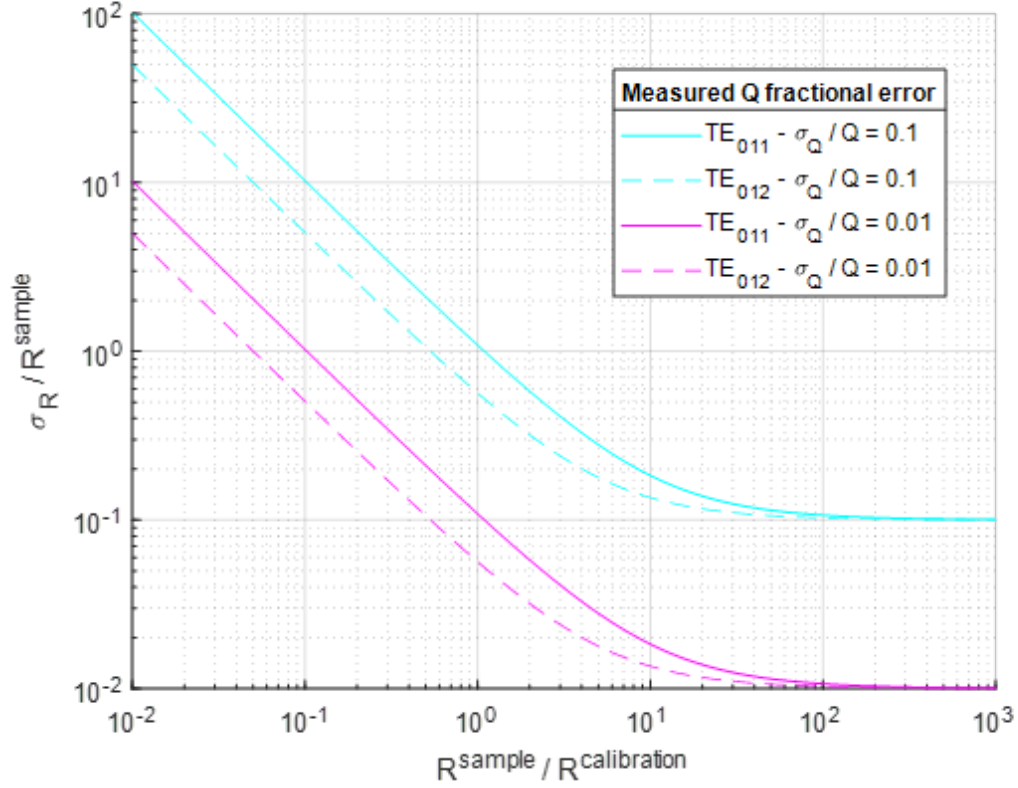
Figure 4.3: Fractional statistical measurement uncertainty calculated with equation 4.7. The fractional uncertainty in the measured quality factors is assumed equal for the sample and calibration measurements. Uncertainties are demonstrated for two values of measurement uncertainty that represent the limits of the typically observed range. The TE_{012} mode has a larger focusing factor which reduces the uncertainty for a given ratio of sample to host surface resistances.

sions that:

$$\Delta \frac{R^{sys}}{R^{sam}_{plate}} = \left\{ (1-\alpha) \frac{P^{cal}_{\Delta R_{plate}}}{P^{cal}_{total}} - \frac{\Delta P_{host}}{P^{cal}_{total}} - \frac{\Delta P_{other}}{P^{cal}_{total}} - \alpha \frac{P^{cal}_{other}}{P^{cal}_{total}} \right\} / \left\{ \alpha \frac{R^{sam}_{plate}}{R^{cal}} \right\} \quad (4.8)$$

$P^{cal}_{\Delta R_{plate}} = \frac{1}{2} \Delta R^{cal} \int_{plate} |H|^2 dS$ was defined in the previous section and accounts

for any discrepancies from the assumed perfect agreement between the average

surface resistance of the calibration plate and the host structure in the calibration

measurement. The scaling depends on the focusing factor (how much field is

focused to the host structure) and will be significant for both modes used with

101

the Cornell sample host cavity. This term could be particularly disruptive for low temperature measurements where the dominant contribution is from residual resistances that are difficult to control with surface processing and could depend on local ambient magnetic fields present on the materials as they transition into the superconducting state.

$\Delta P_{host} = P_{host}^{sam} - P_{host}^{cal}$ accounts for differences between the dissipation on the host structure between the sample and calibration measurements. It has unity scaling and its impact could be significant. A potential source for this could be microscopic flakes of indium that stick to the surface while scraping residual indium off of the flanges while switching sample plates.

The third and fourth terms correspond to sources of dissipation extrinsic to the resonator, such as spurious resonances in the coupling antenna chamber or ohmic dissipation on the copper coupling antenna itself. The choice of including $\Delta P_{other} = P_{other}^{sam} - P_{other}^{cal}$ was made to demonstrate how, if there is a non-negligible source of extrinsic dissipation in the system, it will have a nonzero contribution to the systematic uncertainty even if these dissipation sources are equivalent in both the calibration and sample measurements. This is due to the imbalance in the contributions to the resistance extraction created by the focusing factor, represented here by the fourth term. Note that the scaling of this term is the smallest so this source would have the least impact for situations resulting in equivalent dissipation. The ΔP_{other} term has unity scaling and indicates that shifts to systematic dissipation between the calibration and sample measurements can be deadly for measurement quality. Shifts between the calibration and sample measurements of this type are functionally identical to changes to the dissipation on the host structure.

The impact of equation 4.8 is demonstrated for Cornell sample host cavity parameters in figure 4.4. Here a single source of error is assumed to be nonzero with magnitude equal to the specified fraction of total dissipation. The purpose of this figure is to demonstrate, for a given sample resistance, how much impact each of these sources would have due to the cavity parameter dependent scaling factors associated with each term. The exact ratio of a given dissipation source to the total dissipation is in general not known, but this figure gives an indication of how much spurious dissipation from a given combination of sources can be tolerated to meet a target systematic uncertainty limit.

Reducing the sources of systematic uncertainty discussed here is extremely important for a calibrated quality factor measurement. As mentioned in the discussion following equation 4.6, there is a theoretical maximum quality factor. If the measured quality factors exceed this value, the extracted sample surface resistance will have no meaning. As is evident from this section, if a sample surface resistance is near to or below that of the host structure this maximum can easily be exceeded due to systematic issues. In practice this is a major issue and is often observed in samples with low surface resistances.

4.4.4 Summary

Conceptually a calibrated quality factor based measurement for advancing accelerator applications is questionable. As has been described in detail and is demonstrated in figures 4.3 and 4.4, the uncertainty of desirable samples, that is samples with surface resistance lower than niobium, is explicitly not within the scope of this measurement scheme. With this in mind it should be noted
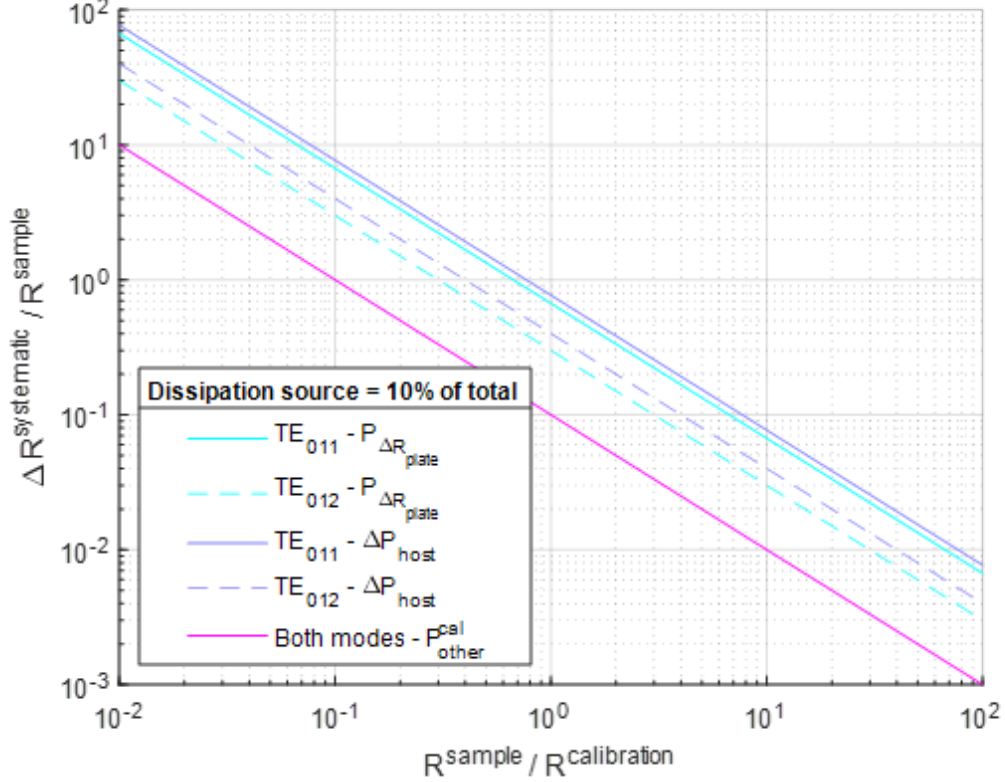
Figure 4.4: Contribution to fractional systematic error of a single source considered by equation 4.8. While the exact contributions of a given source of systematic uncertainty cannot be measured this figure can serve as a guide indicating what levels of systematic dissipation can be tolerated. Note that the term corresponding to different amounts of dissipation in the sample and calibration measurements is omitted as it is indistinguishable from the contribution ΔP_{host}

that to date very few non-niobium samples have been produced that succeed in reaching such low surface resistances [Posen and Hall, 2017, Keckert et al., 2021]. Therefore, at this time a calibrated quality factor measurement does have a place in making useful measurements of novel samples working towards accelerator goals. If samples improve, then it is usually possible to produce a reliable upper bound on surface resistances for low dissipation samples. From a scientific perspective, the system is useful for observing the large scale temperature or field dependence of a sample. It will be difficult to understand and trust

measurements with more subtle dependencies which will be obscured by systematic behaviors and noise. The combined effect of systematic error, that can change unexpectedly between tests, and small statistical error can significantly corrupt surface resistance results.

The magnitude of the RF field on the sample is measured independently from the calibration procedure, and is expected to be more reliable. But compared to accelerator cavity based measurements it is limited to relatively small values. This is partially due to operating at a higher frequency. From the perspective of advancing accelerator interests, this field is currently sufficient as no samples have been produced that exceed the observed limits.

If appropriate samples are measured and significant efforts are made to reduce and prevent systematic uncertainties, this sample host cavity can be used to deliver novel and useful results for both accelerator applications and scientific understanding. Using the equations of uncertainty presented in this section, summarized in figures 4.3 and 4.4, the suitability of a given sample can be determined. This gives rise to a new problem: identifying sample studies that both probe interesting science and have surface resistances larger than the niobium host structure. A study that attempts this path is discussed in chapter 5.

4.5 Upgrades to the Cornell sample host cavity

The original sample host cavity was designed, constructed, and commissioned by 2014 [Hall et al., 2013, 2014a,b]. Its initial design and implementation were flawed. After several years of operation these flaws manifested into serious is-

sues preventing the serious use of the sample host cavity. A series of changes were proposed to address these problems. This section introduces these problems, motivates the choices and designs of the alterations and new features, and discusses the ensuing positive and negative results. The goal was to make the system reliable for a wider range of samples and variables, acknowledging that the system has major intrinsic limitations due to the calibrated quality factor measurement. In general, the changes presented in this section were successful but there remain some new and mysterious issues degrading performance.

4.5.1 Major issues of the original system

The problems that initially prevented reliable application of the sample host cavity are summarized in this subsection. They will each be discussed in further detail in the remainder of the section.

After the original commissioning, the key problem was large residual resistance from unknown sources preventing reliable calibration and niobium sample baseline measurements. This problem was intermittent and seemed to become more common and more severe over time. By 2017 the system was unusable. The source of this residual resistance was eventually linked to a high-temperature outgassing bake to remove hydrogen after treating the surfaces with acids. By altering the standard preparation procedure for the host structure and niobium samples this issue has been entirely eliminated.

The next issue was difficulty with taking measurements. In its original form the sample host cavity was constructed with no transmitted power probe. The phase locked loop was used to minimize the reflected power signal as opposed

to using the transmitted power typically employed for this purpose (see section 2.3.2). While this was functional and it was never demonstrated to yield inferior quality measurements, it was difficult or impossible to work with as a user. Driving the cavity at resonance while temperature was slowly changing, for example, was not possible. Adding a transmitted power probe into the host structure and making changes to the forward power coupler seems to have greatly improved these difficulties and for some time appeared to, in part, reduce measurement uncertainty.

Lastly the range of input powers that could be reliably measured was restricted. For low powers the lack of a transmitted power probe was the problem because the changes in reflected power required for driving the cavity at resonance with a phase-locked loop became too noisy. More seriously, there were major problems when the resonator was driven with high power. Intermittently, at sufficiently high input powers (only several Watts), distortions in the decaying power were observed through the forward power coupler after shutting off the signal generator. These could take the form of abrupt jumps in the exponential decay either up or down or in clearly non-exponential decays. Likely related to this was a noticeable change in the measured quality factors at these higher input powers, though this occurred independently from the observation of these steps in the decaying power signal. To address this, the forward power coupler and helium-vacuum feed-through was entirely redesigned and replaced. The new system has eliminated all of these issues though it has caused some new, though less severe, problems that have yet to be explained or resolved.

4.5.2 Eliminating spurious residual resistance

Since its inception the sample host cavity would sporadically display high residual resistance. Over three years of operation this behavior became more common until all that was observed were residual resistances approaching 600 nΩ and 1000 nΩ for 4.0 GHz and 5.2 nΩ respectively at high RF field amplitudes. This limits the utility of the sample host cavity in many ways. The maximum observed fields were usually limited by amplifier power and not due to a quench of the host structure or sample. The high host resistance limits minimum resistance that can be adequately resolved. One of the key assumptions of the calibration procedure, that the host structure and calibration plate have identical surface resistance, was likely violated because the residual resistance had a strong field-dependence and may not have been uniform throughout the surfaces. Identifying the cause of this significant residual resistance and eliminating it became a priority.

Because the residual resistance looked roughly linear in its dependence on RF field amplitude, a prime candidate for its source was dissipation due to trapped flux [Liarte et al., 2018, Checchin et al., 2018]. However, no large ambient field sources were observed consistently and changes to the support structure to reduce ambient magnetic fields and thermal currents did not produce meaningful change. After this surface contamination became the focus. It is now apparent that the cause of residual resistance was contamination introduced by the standard outgassing bake to remove hydrogen after electropolishing. This was performed at ultrahigh vacuum at 800° C for 5 hours. The furnace loading and unloading is performed in a class 100 cleanroom environment but initially no steps were taken to protect the sample plate or host structure RF

surfaces from contamination within the furnace during standard operation.

Two measures have been added to the niobium preparation procedure to re-duce contamination from this process. First is covering the openings of the host structure and enclosing the sample plate with buffered-chemical polished (BCP) niobium foil when they are in the furnace. Second is removing $\sim 4\,\mu$m of material using electropolishing after the outgas baking step. Apparently, the contamination does not diffuse far into the material surface since this step appears to be very effective. Only a small amount of material can be removed in this step to avoid loading hydrogen into the material which can also degrade performance. The following procedure for resetting the surface of the host structure or producing/resetting a new niobium sample plate contains the newly introduced steps taken to mitigate contamination.

<u>Nitric acid</u>: the flanges of the cavity make use of indium gaskets to maintain ultra-high vacuum (UHV) in superfluid helium. To remove all indium from the flanges before furnace treatments each flange is supported by two PVDF bars and then submerged in $68\% - 70\%$ nitric acid for 30 minutes. After 15 minutes the host structure is rotated by 90 degrees. Typically, the interior of the cavity is also given a 30-minute nitric acid soak as well to remove any indium (or other contaminants) that could have adhered to the RF surface. The procedure is similar for the sample plates. The acid is removed with deionized (DI) water.

<u>Electropolishing (EP)</u>: For resetting the host structure or a sample plate $\sim$ $10\,\mu$m of material is removed by electropolishing. For new material $\sim 100\,\mu$m is removed. The setup used for electropolishing the host structure is shown in figure 4.5. The polishing solution is a 9:1 mixture of sulfuric acid to hydrofluoric acid. It employs a hollow aluminum rod as the cathode. A PVDF propeller is

used to agitate the solution and is operated while the polishing voltage is active. A Teflon mesh is wrapped around the cathode to capture hydrogen bubbles and prevent them from disrupting the polishing at the host structure surface. While the polishing voltage (12 V) is active, water is continuously run on the outside of the cavity to prevent the solution from heating significantly. For sample plates, a similar setup is used. The sample polishing setup is shown in figure 4.5. For this configuration, a polishing voltage is typically found between $3\,V - 5\,V$. For niobium samples, stirring is not typically used and the sample is completely emerged in liquid. Cooling for the sample plate is typically done by enclosing the container of electropolishing solution in a secondary container filled with ice. After polishing the material is rinsed with de-ionized (DI) water and then submerged in an ultrasonic bath with warm DI water mixed with liquinox for 30 minutes. Finally, it is rinsed clean with DI water and submerged in a second ultrasonic bath with pure DI water for 30 minutes.

Out-gassing bake: The host structure and/or sample plate is baked at high temperature under vacuum to remove hydrogen introduced by the acids in the electropolish solutions. First the RF surface is given a high-pressure rinse (HPR) in a class 10 cleanroom environment to remove any contamination that may have been introduced while in transit after the previous step. The cavity/plate is then sealed in a clean plastic bag and brought to a portable cleanroom that surrounds the entrance of a vacuum furnace. Prior to being loaded into the furnace the openings of the host structure or the entirety of the plate are covered with buffered-chemical polished (BCP) niobium foil. The furnace is evacuated to UHV and quickly ramped to $800°\,C$ where it is held for 5 hours. The furnace is then left to cool to near room temperature before being brought to atmospheric pressure by a clean mixture of nitrogen and oxygen.
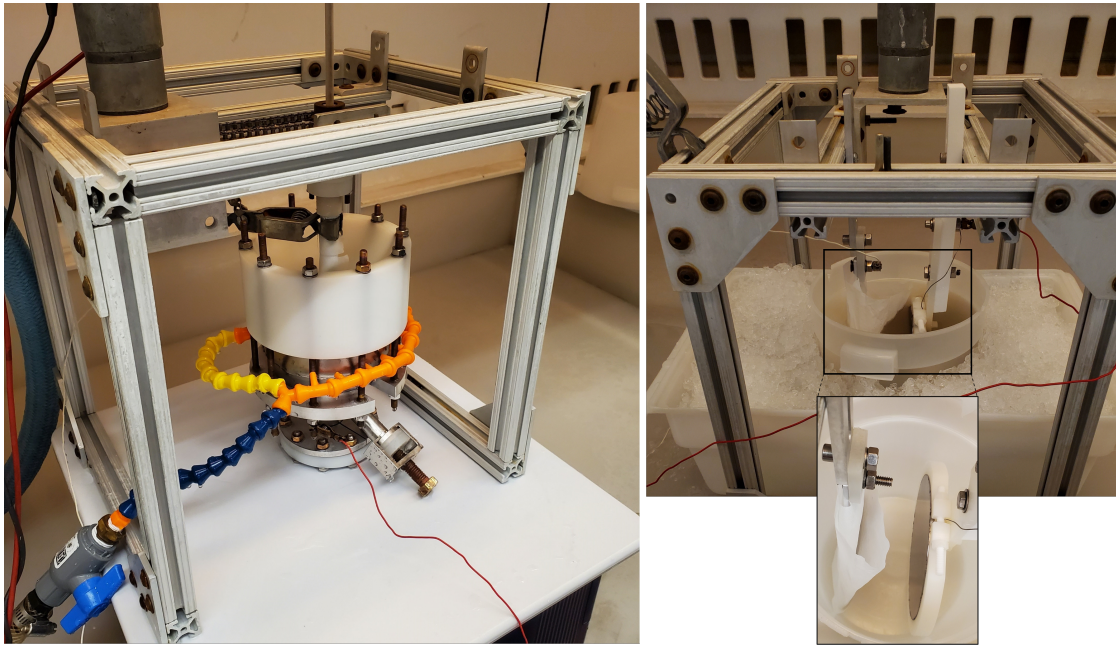
Figure 4.5: (Left) Electropolishing (EP) setup for host structure. Includes water cooling, agitation propellor, aluminum cathode and protective film, EP solution guide, and flange stoppers. (Right) EP setup for niobium sample plates showing ice cooling, circular aluminum cathode and protective film and rigid support for niobium plate

Post-bake electropolish: A light electropolish removing $\sim 4\,\mu$m after the high temperature bake appears to be a suitable balance of polishing deep enough to remove contamination introduced by the furnace without introducing too much hydrogen into the RF surface which can also degrade performance. To assist with preventing the introduction of hydrogen impurities after the target removal is reached the EP voltage is left at a small value (200 mV) where it will not continue polishing or removing significant amounts of material but will provide some bias repelling hydrogen ions from the niobium.

Since the introduction of the above procedure the observed residual resistance has remained low for three separate niobium plates. Figure 4.6 demonstrates the changes in measured residual resistance corresponding to the above procedural changes. All measurements are of niobium sample plates with

800° C bakes in vacuum. The measurement corresponding to the original treatment, where the host structure and plate are uncovered in the furnace, was performed using a different niobium plate than the next two measurements, but the original was brought back for the final measurement corresponding to the light EP on the host structure and sample plate. A significant improvement was observed after covering the RF surfaces with cleaned niobium foil in the furnace.

Removing $4\,\mu$m of material from the RF surface via electropolishing also reduces residual resistance, particularly at higher RF fields. Having a relatively flat surface resistance dependence on RF field is important for minimizing systematic error in the calibration procedure due to the unequal field distributions on the host structure and sample plate. It is interesting to note that at $4.0\,$GHz the quench field apparently was slightly reduced after the light EP. Repeating the measurement with this plate but after performing the light EP on the host structure a mild reduction in residual resistance is visible at $4.0\,$GHz but not at $5.2\,$GHz. This would suggest the sample plate was more contaminated than the host structure. However, previous measurements may suggest that the host structure can also act as a source of residual resistance. It is important that both be processed carefully after high temperature treatments.

4.5.3 Transmitted power probe

Before the transmitted power probe was added to the sample host cavity the system would intermittently be very difficult to use. It was thought that, in part, this had to do with using the reflected power for locking to resonance. It
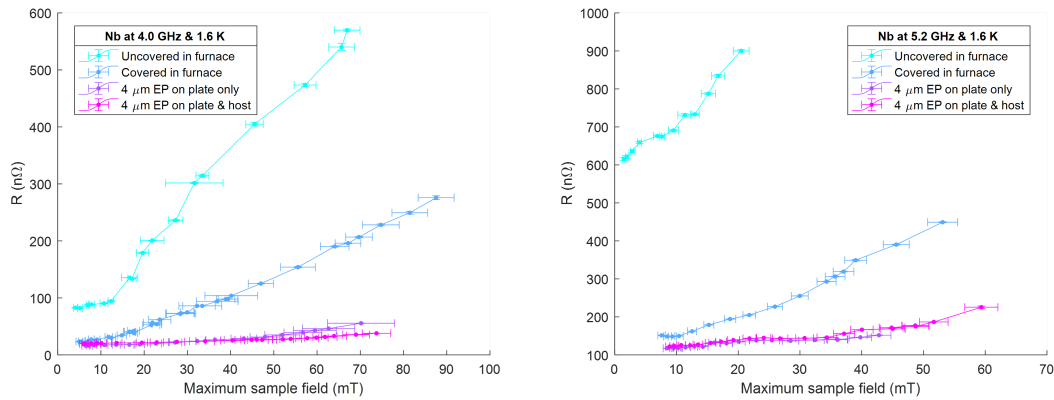
Figure 4.6: Average resonator surface resistance with niobium sample plates treated with an $800°$ C bake in vacuum measured at 1.6 K for the TE_{011} (left) and TE_{012} (right) modes. Samples displayed are chosen to exemplify the effect of removing furnace-induced contamination on residual resistance. Note that the uncovered TE_{012} mode measurement displayed here is at 2.0 K instead of 1.6 K but the resistance is expected to be largely residual so the distinction should not be too meaningful.

was common in operation of the sample host cavity to spend hours being unable to collect data since resonance could not be found - only for it to suddenly become functional again. Temperature-dependence data was never successfully collected since resonance could not consistently be found while the temperature was slowly changing. The TE_{012} mode was not measured before the introduction of the transmitted power probe. Locking to resonance with low and high powers was also problematic.

Driven by these problems the decision to add a transmitted power port to the existing host structure was made. Adding the port to the structure was challenging. The location of the port and its dimensions had to be carefully chosen such that it could be drilled in the host structure and electron beam welded into place without disturbing the surface or negatively impacting the geometry-dependent metrics of the sample host cavity. A transmitted power

coupler (TPC) then had to be engineered to meet design specifications for both modes of operation and exist within the dimensions of the port. Specifically:

- Transmitted external quality factor: $Q_e\,(\text{TE}_{011}) \leq 10^{13}$ and $Q_e\,(\text{TE}_{012}) > 10^{11}$

- No reduction of host quench field: for both modes the enhancement of the field due to the edges of the port should not increase it beyond the original peak field on the host structure.

- No extra dissipation: for both modes the dissipation on the coupling antenna should be negligible compared to total dissipation in the system.

The end-result was a success. All of the above problems have been eliminated and no new issues have been associated with the probe.

The transmitted power probe should be located such that the port is far from high-field regions of the surface. The location of the probe in this upgrade is not ideal, especially for the 5.2 GHz mode, but was imposed by physical constraints. Specifically, the location was chosen primarily since it was the most suitable surface on the existing structure for electron beam welding. Other physical constraints were considered that impacted the allowed angle and length of the tube housing the coupler, such as not interfering with the clamps on the forward power coupler (FPC) flange, not interfering with existing peripheral hardware such as that used for allowing for water or acid to drain from the high-pressure rinse (HPR) mounting system or electropolishing support structures respectively. The tube is made of high RRR niobium and the flange of reactor grade niobium. The physical structure is shown in figure 4.7. These physical constraints imposed limitations on where the TPC could be placed and the maximum length of the tube. A suitable design was found by varying the diameter

of the port, the angle at which it joined the host structure, and most critically the height of the port.

A demonstration of the design process is shown in figure 4.7. Note that all design simulations were performed with CST Microwave Studios. On the left axis the ratio of the peak field along the path of the new port edge to the max field on the host structure is plotted for both modes. For the TE_{011} mode a clear benefit is found when the port is towards the bottom of the structure. For the TE_{012} mode not much change is observed since the entire flat segment of the host structure suitable for e-beam welding is near the maximum in this mode. A value of 15 mm was chosen for the final design to optimize the TE_{011} mode performance. For instructive purposes the right axis is included to convey the amount of enhancement induced by the port. It shows the ratio of the peak field on the path of the port edge to the peak field along the same curve with no hole in the simulation. The angle of the port with the host structure and the diameter of the tube also are important for field enhancement considerations, but the former was constrained by e-beam welding requirements and the latter was utilized to help reach external quality factor demands as will be discussed later. It was found that some rounding of the port was required to prevent field enhancement, but once it was somewhat rounded increasing it further did not lead to improvements. The process of e-beam welding automatically gave the port edges some rounding as can be seen in figure 4.7.

Simultaneously with choosing the location, incidence angle, and dimensions of the port to satisfy the condition of not reducing the host structure quench field, a coupling antenna was designed to satisfy the other design requirements. As demonstrated in figure 4.8 the magnetic field can readily be coupled to using
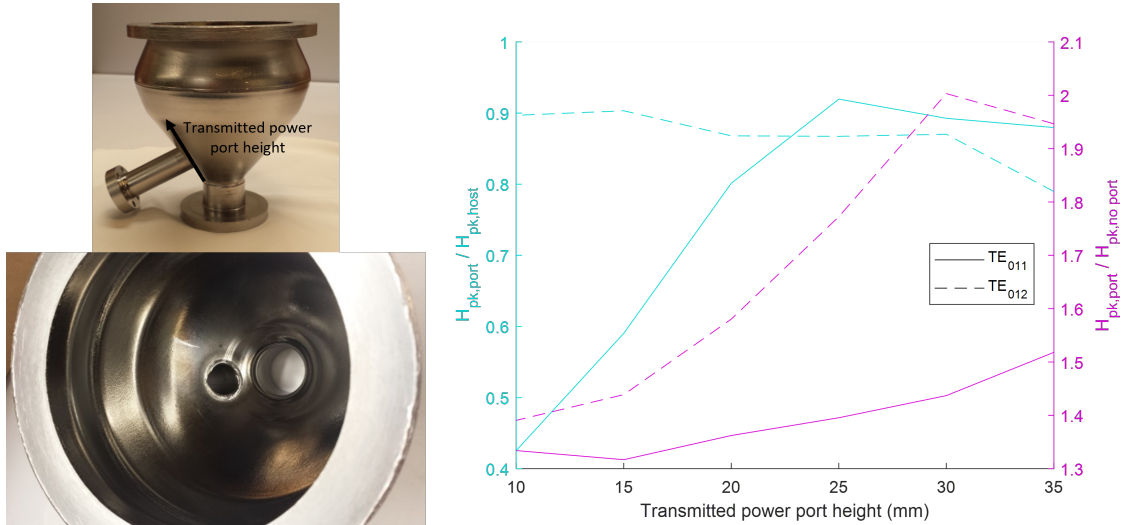
Figure 4.7: (Left) Cornell sample host cavity after the addition of transmitted power probe port and niobium tube showing the outside and RF surface. (Right) Demonstration of design process - adjusting port height (defined by the black arrow on the top left image) and demonstrating the port should not be expected to lower the host structure quench field for either mode. The left axis shows that the ratio of the peak field at the location of the new port to the peak field on the host structure is less than unity. The right axis demonstrates the enhancement of the field due to the port by comparing the peak value at the location of the new port to the peak field of the same curve simulated with no port.

a loop. Unless resonances were present the dissipation on the copper antenna was not expected to be an issue as confirmed by simulation and demonstrated in figure 4.8. The spike in dissipation around 3 mm corresponds to a quarter-wavelength coaxial-like mode coupling to the 4 GHz TE_{011} mode. The path to avoid this while keeping the port dimensions and location acceptable for the constraints described above was to make a large diameter loop. It was chosen to make it as wide as possible relative to the diameter of the tube. This helps keep the length of the tube short to avoid interfering with other parts of the RF and cryogenic systems. The stem joining the loop to the feed-through had to be long enough to be threaded onto the feed-through. The height of the loop

therefore becomes the main free-parameter for adjusting external quality factor and a value of 5.5 mm was chosen as demonstrated in figure 4.8. The SMA feed-through was a commercial piece with a modified flange. Notably, it was constructed with titanium to reduce ambient magnetic fields near the cavity. An indium gasket was chosen to prevent the risk of spurious losses from currents being driven in a copper gasket.
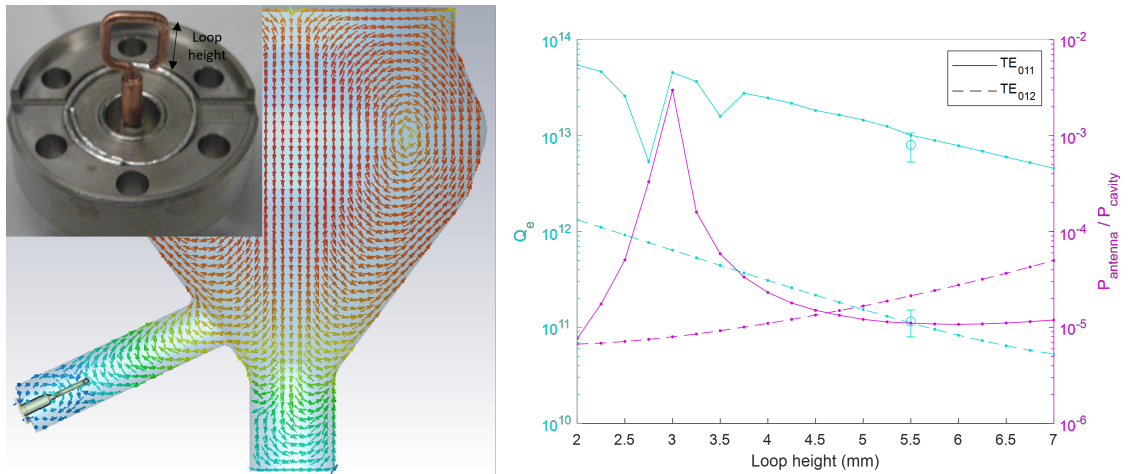
Figure 4.8: (Left) The physical coupling antenna is shown along with its feed-through and indium gasket. A cross-sectional view of the TE_{011} mode magnetic fields demonstrates how they can be enclosed in a loop for efficient coupling. The TE_{012} mode is similar. (Right) The design metrics are then shown demonstrating that a loop height of 5.5 mm satisfies the external quality factor design goals for both modes. The error bars displayed, at 5.5 mm, are the mean and standard deviation of the measured external quality factors for a dozen independent assemblies and cooldowns and indicate agreement with simulation. The simulated dissipation normalized to the lowest observed dissipation for each mode at 1.6 K is shown indicating that no spurious dissipation is expected.

The implementation of the transmitted power port and the coupling antenna appears to have been a complete success. All of the problems with operation described at the beginning of this section were eliminated. There is rarely any difficulty driving the system on resonance, high quality measurements of temperature-dependence are now possible, and the low power limit is due to

the minimum power required for triggering the power meters. No coupler resonances are observed and the measured external quality factors are near the design values, as can be seen in figure 4.8. The transmitted power probe has been assembled and removed from the cavity and thermally cycled from room temperature to liquid helium temperature dozens of times without changes in performance or developing any issues. As shown in figure 4.7 the field enhancement due to the port for the TE_{012} mode is nontrivial. While the simulation does not indicate it will exceed the maximum field on the host structure it is entirely possible discrepancies between the real system and the model used for simulation could result in the port reducing the quench field for this mode. In the TE_{012} mode the quench field and residual resistance observed are both appreciably worse than the TE_{011} mode, though are at reasonable values. No data is available to measure any potential changes in the TE_{012} mode prior to the introduction of the TPC.

4.5.4 Forward power coupler

The original forward power coupler and vacuum-helium feed-through, shown in figure 4.9, were suspected to be causing issues at high input powers. Difficulties in the high-power regime included trouble locking to resonance, unusable data caused by abrupt jumps in the power decay traces used for obtaining quality factors, and a relative shift from the low power quality factors when the input power exceeded ($\sim 10\,\mathrm{W}$) [Oseroff and Liepe, 2019]. Changes to the quality factor and difficulty locking to resonance could be attributed to the use of reflected power in the phase-locked loop. However, the anomalous features of the power decay traces occur after the signal generator is shut off and indi-

cate they must have a different source. This was the primary justification for redesigning the coupling antenna and feed-through.
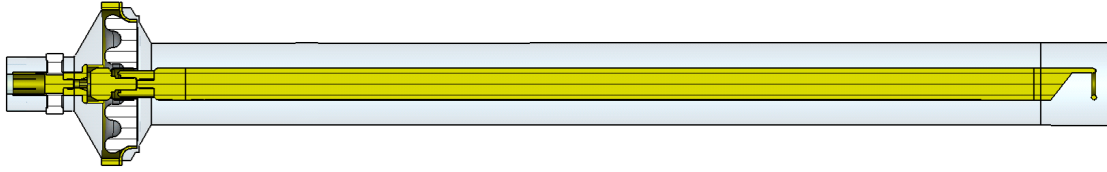
Figure 4.9: Original design for the forward power coupler. The feed-through was designed for lower frequencies and very high-power operation. The coaxial region made use of a steel vacuum tube and bellows section for the out conductor.

A number of issues existed with the original design. It consisted of a $50\,\Omega$ coaxial line ended by a loop to couple to the magnetic fields pointing along the axis of the cavity. A stainless-steel bellows segment allowed for moving the relative separation between the cavity and the coupling antenna to control the external quality factor. The range of this separation is limited by that of the stepper motor used to control the coupler position. The outer conductor of the coaxial line was stainless steel and is part of the overall support structure of the cryogenic measurement setup. This steel segment should cause greater dissipation than copper and the bellows region could be a source of spurious reflection and dissipation in the RF path. To create a $50\,\Omega$ coaxial line with this outer conductor, the OFHC copper inner conductor had to have a rather large diameter relative to the connection piece to the feed-through. The result was mechanically unstable and the structure could easily be tilted and moved. A Teflon centering piece was included but over the course of several thermal cycles it shrank and was not effective. Because the support structure used for performing cryogenic RF tests with the sample host cavity requires an extremely long coupling antenna ($\sim 30\,\mathrm{cm}$), even tilting angles less than one degree can cause meaningful displacement at the location of the antenna and change the RF per-

119

formance. The long coupling antenna makes it more challenging to design a coupler that does not having coaxial resonances at the higher frequencies used by the sample host cavity. The original feed-through was designed for lower frequencies. Simulations suggest there may have been a strong resonance very close to the TE_{011} mode though this was never measured (due to the small connection region breaking irreparably).

The re-designed coupling antenna and feed-through, shown in figure 4.10, was constructed to avoid the problems detailed above. It has a copper outer conductor to reduce dissipation and shield the main RF path from unwanted effects of the bellows and vacuum ports in the steel structure around it. A Teflon piece at the top of the outer conductor ensures the relative spacing between the inner and outer conductors is maintained so that no impedance changes are expected along the coaxial wave-guide. The feed-through is a commercially available socket N-type connected to a plug N type converter that allows for the copper pieces to be inserted into it and is much more mechanically stable than the original design. The target parameters include a suitable external quality factor range for both modes ($10^7 - 10^{12}$), no major sources of dissipation impacting measurement, and no resonances near the operating modes of the sample host cavity.

Conceptually the new coupler was sound, however its design and implementation were flawed. The external quality factor and power reflection are sensitive to small perturbations in dimensions. This design flaw was perpetuated by the difficulty of realizing the design dimensions, especially on the loop. As a result, the simulations of external quality factor and reflected power ($|s_{11}|$) used in design do not agree well with measured values. In addition, the lo-

Figure 4.10: Replacement for the original coupler, designed to operate at 4.0 GHz and 5.2 GHz respectively and correct some of the perceived issues with the original design. The coaxial wave-guide region consists only of copper and shields the path from potential issues at the bellows region. A Teflon centering piece maintains the 50 Ω geometry of the coaxial line. Due to difficulties with simulation and construction of the exact dimensions, the new coupling antenna displayed a number of issues such as resonances near one of the operating modes. To remove them, the outer conductor was shortened until no resonances were visible.

cation and orientation of the coupler were influenced by imperfections in the flange used to attach the coupling antenna to the overall support structure. This resulted in tilt angles up to $0.7°$. Beyond the disagreement between the observed and simulated values, there are unexplained features in the measured external and intrinsic quality factors and how they depend on the position of the coupling antenna relative to the cavity.

Resonances were initially present near the 5.2 GHz mode but were removed by gradually reducing the length of the outer conductor. The measured reflection spectrum of the current iteration is shown in figure 4.11. This measurement was performed at room temperature but similar measurements have been carried out with the system at cryogenic temperatures. No major changes to $|s_{11}|$ have been observed at different temperatures or coupler locations relative to the cavity. It also seems robust against changes in coupler rotation and overall tilt. It is currently believed that coupled resonances are not a source of measurement issues.
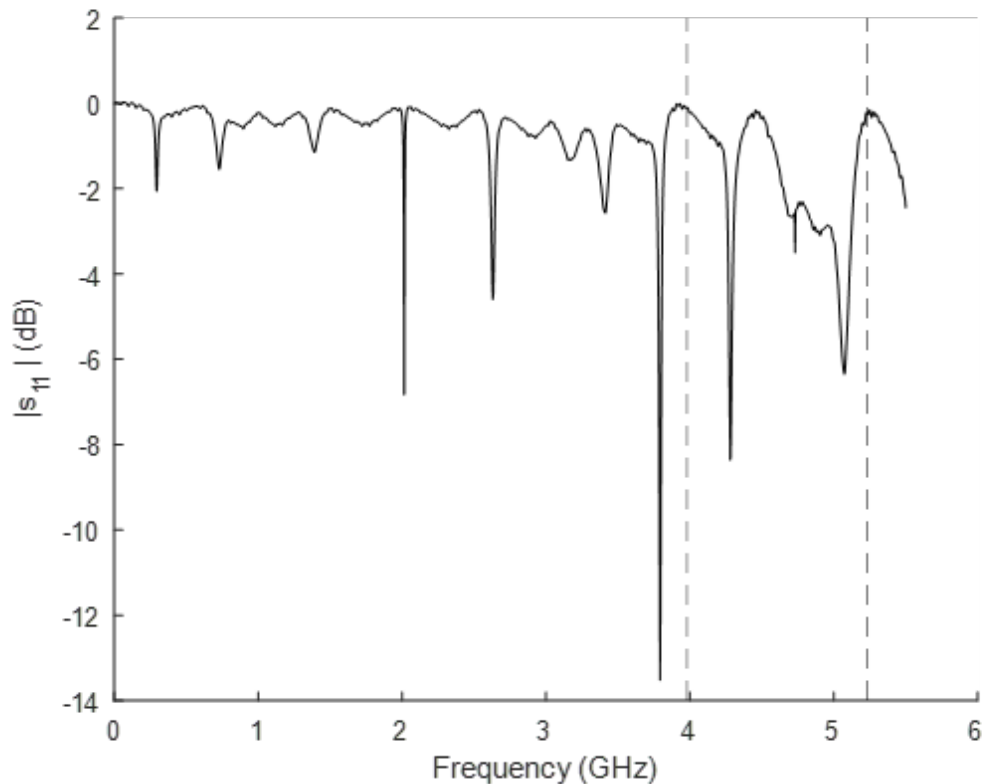
Figure 4.11: Measured reflected power at the input to the vacuum feed-through of the forward power coupling antenna. Dashed vertical lines correspond to the operating modes of the sample host cavity. Simulations did not agree well with the measured values so the length of the outer conductor was gradually changed until no resonances were observed at either of the operating modes.

The range of external quality factors accessible within the adjustable coupler range with the current iteration of the coupling antenna is shown in figure 4.12. Each of the lines corresponds to a separate measurement of a niobium plate used for either calibration or baselining before a sample deposition. The choice of measurements presented here was made to demonstrate the full range of variation observed. Some of the changes are due to intentional changes in the coupling antenna such as changing the tilt angle by a fraction of a degree. However, it is just as common that changes of this order can occur spontaneously. Typically, if no conscious change is made to the coupling antenna, it will hold

its external quality factor for four or five measurement cycles (from assembly to cryogenic temperatures to disassembly). An exact mechanism is not known, but due to the sensitivity of the coupler metrics to its dimensions and position it is reasonable to expect slight changes occurring from transporting the system between the various steps. For the TE_{011} modes note that, despite the wide range of observed external quality factors at a given spacing between the coupler and cavity the upper limit remains in the desired range. Recently the lower limits of the external quality factor for this mode have been less accessible due to an unexplained spike upward. A possible explanation of this feature is the tilt of the loop, causing it to act as an off-center hook shape coupling to the magnetic fields perpendicular to the axis. The TE_{012} mode, for some of its lower Q_e situations, is sometimes well below the target upper limit. There are no issues with its lower limit. It is alarming that the external quality factor can change so easily for both modes, but it does not seem to have caused major issues.

The measured intrinsic quality factors as a function of coupler position are demonstrated in figure 4.13. The included measurement series are those of figure 4.12 for comparison, however, they also present a complete picture of the coupler position dependence of the intrinsic quality factor. In some measurements the intrinsic quality factor is seen to drop exponentially with coupler position (coupler - cavity separation decreasing). This is expected since the circular tube between the coupling antenna and the cavity opening acts as a circular wave-guide operated below its cut-off frequency. There is a second case displayed in figure 4.13 where an anomalous behavior is observed. Here the reported quality factor increases beyond what is physically and intuitively reasonable. The expected and anomalous coupler position dependence have been observed on both modes. Typically, if one is behaving as expected the other
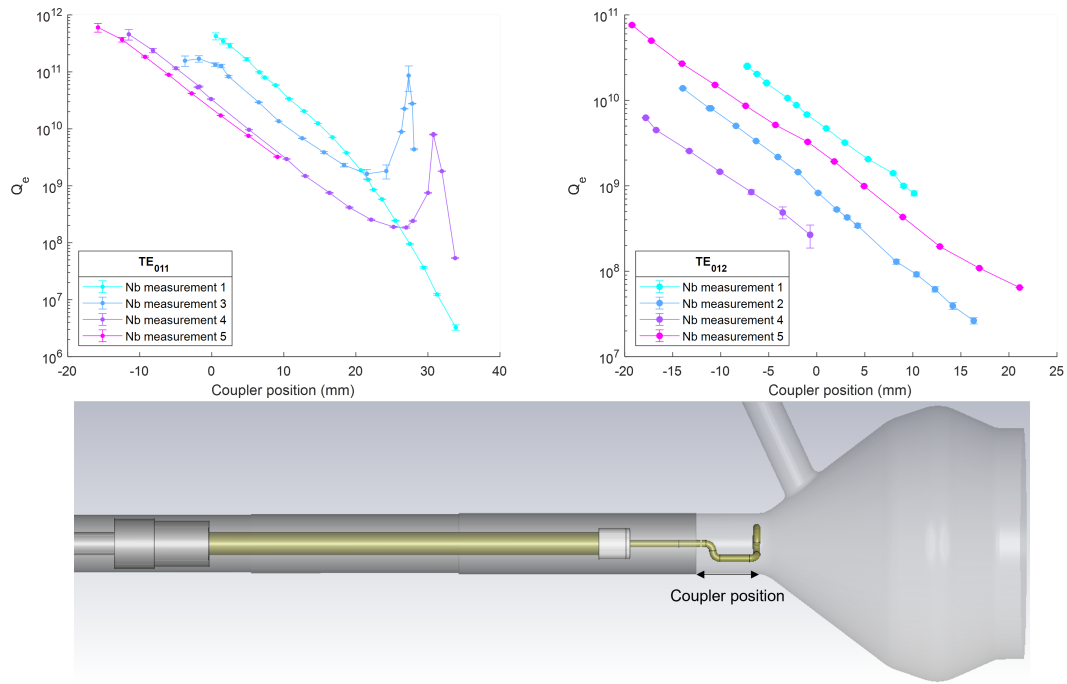
Figure 4.12: Measured external quality factors for the TE_{011} mode (left) and TE_{012} mode (right) at $2\,K$ over either the full range of motion of the stepper motor and bellows or until the measurements become nonsensical for unknown reasons. The coupler position corresponds to the distance towards the cavity measured from the its flange with the support structure. Each line corresponds to a separate measurement of a different niobium calibration or baseline plate. Changes in external quality factor are often due to slight changes in the coupling antenna such as re-assembling it and changing the tilt angle by fractions of a degree, but can also happen spontaneously.

is anomalous. The mechanism causing this is not currently known. Similar to the shifts in external quality factor, the changes in behavior can be induced by subtle shifts to the fundamental power coupler after it is removed and replaced. However, this can also occur spontaneously. A shift between the two cases has even been observed mid-measurement.

This anomalous dependence of the intrinsic quality factor on the coupler position is alarming; however, it does not appear to be deadly if measurements are performed with the coupling antenna far from the cavity (smaller values

for the coupler position). In this low coupling regime (left side of figure 4.13) the values of Q_0 all converge to a similar value. This is expected since, while each of the measurements presented here corresponds to a different niobium sample plate surface, they are still the same material at the same temperature and frequency. This indicates that as long as measurements are taken with low coupling the anomalous behavior should not have a major impact. Low coupling is also required for minimizing dissipation on the coupling antenna. All of the measurements presented in figure 4.13 level off at lower coupler positions which should be expected since when the coupler is far from the cavity its dissipation should be minimal and should not impact the measurement. This indicates the design has succeeded in maintaining reasonably low dissipation on the coupling antenna in both modes, though the TE_{012} mode may still have some error from dissipation on the coupling antenna. For the cases demonstrating the expected coupler position dependence the exact dissipation on the coupling antenna could be extracted by fitting a line to the high coupling positions where this dissipation dominates and extrapolating it to a given position.

The results presented here indicate that reliable measurements can be made in the low coupling regime despite significant problems existing in this system. Even in the TE_{012} mode, where the external quality factor upper limit can be lower than desired, the results of figure 4.13 indicate that the measured quality factors approach reasonable values and have minimal dependence on the coupler location. Compared to the previous version of the forward power coupler this is an overall improvement since, despite the changing external quality factor ranges and anomalous dependencies on coupler position, the original issues preventing reliable measurements above $\sim 10\,\text{W}$ are entirely removed. The new design was an overall success that helped eliminate some of the problems re-
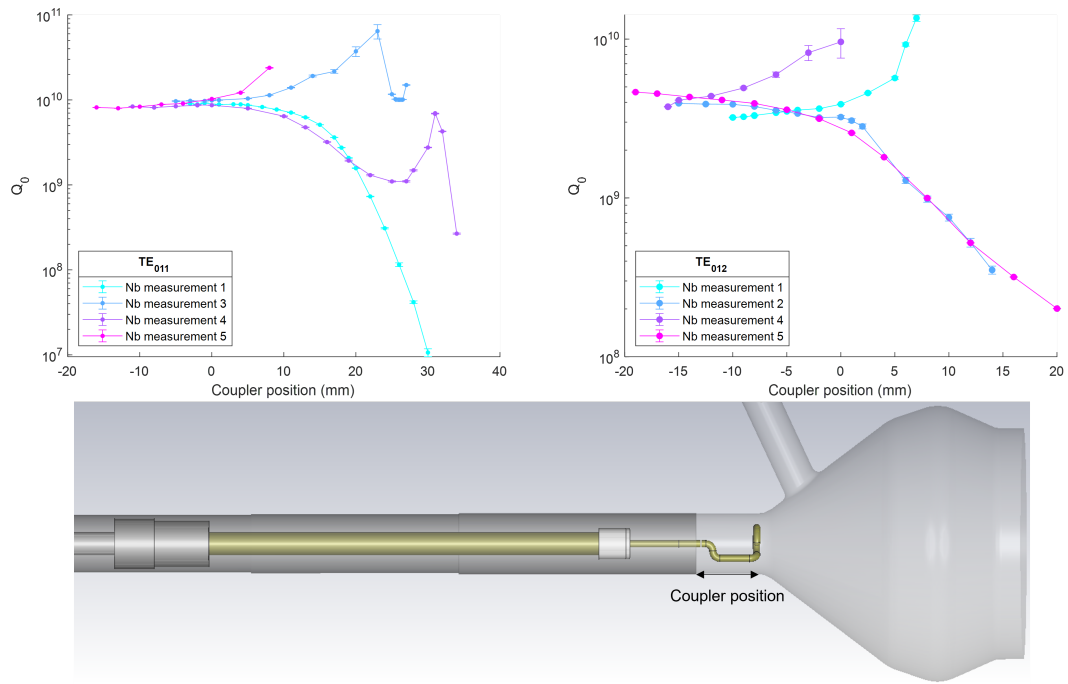
Figure 4.13: Measured intrinsic quality factors for the TE_{011} mode (left) and TE_{012} mode (right) at 2 K over either the full range of motion of the stepper motor and bellows or until the measurements become problematic for unknown reasons. The coupler position corresponds to the distance towards the cavity measured from the its flange with the support structure. Each line corresponds to a separate measurement of a different niobium calibration or baseline plate. In some cases, the expected exponential decrease in the quality factor due to increased dissipation on the coupling antenna as it moves closer to the cavity is observed. In others an anomalous observation is made in which the measured quality factor increases. This behavior has been observed on both modes of operation but typically not simultaneously and can be induced by subtle changes to the coupling antenna or spontaneously.

ducing the utility of the sample host cavity. Despite this, a new design that is easier to construct and is more robust to perturbations should be a priority for further improving the system.

4.6 Calibration and baseline measurement

It is essential for a calibrated quality factor measurement to have a reliable calibration data set. For calibration, a niobium plate is prepared identically to the host structure, as described in section 4.5.2, and it is assumed the two have equivalent surface resistance. In this section, the most recent calibration data sets are presented along with the fits used to calibrate the space between measurement fields and temperatures. The reasonable quality of the calibration will be demonstrated by comparing it to theoretical expectations and related data from other sources.

4.6.1 Calibration data and fits

With the sample plate prepared identically to the host structure the average resistance of the entire resonant structure is assumed to have a uniform average resistance, $R = G/Q$, where G is the simulated geometry factor and Q is the measured quality factor. The basic measurement schemes explored with the sample host cavity include low-field temperature-dependence, where the temperature is continuously swept as data is taken, and low-temperature RF field amplitude dependence, where the temperature is held constant and the input power is altered as data is taken.

The average surface resistance of a niobium calibration plate measured in both of these scenarios is presented in figure 4.14. The statistical measurement error that is obtainable, primarily from power meter measurements, does not lead to significant error. However, the reported RF field uncertainty is signifi-

127

cant and is demonstrated by horizontal error bars on the field-dependence figure.

To utilize these measurements as a calibration for samples of interest it is required to relate them to the temperature or RF field amplitude at which the same measurements take place. For this purpose, the calibration data is fit to a polynomial (fifth order for temperature-dependence, second order for 4.0 GHz field-dependence, and first order for 5.2 GHz field-dependence). The resulting fits and their 95% prediction intervals are represented by the shaded areas in figure 4.14. The prediction intervals then assume the role of "measurement" uncertainty for the calibration in the sample resistance extraction procedure. As such the choice of polynomial order is made in an attempt to ensure that the behavior of the data is captured within this prediction interval. This is largely true for the data presented here, with the exception of the RF field amplitude dependence of the surface resistance at 5.2 GHz. Here the data follows no clear polynomial dependence. A linear fit was chosen since it can be made to capture the behavior entirely over the range of fields explored, though it does obscure minor changes in the resistance field-dependence that may be present at this frequency. To justify this recall that this sample host cavity should really only be used for careful resistance measurements when the sample has a surface resistance greatly exceeding that of the host structure (specifically the values presented in figure 4.14 for a given temperature). In this high resistance sample regime the minor details of the RF field-dependence will not be crucial to the measurement resolution and can be omitted without major issues.
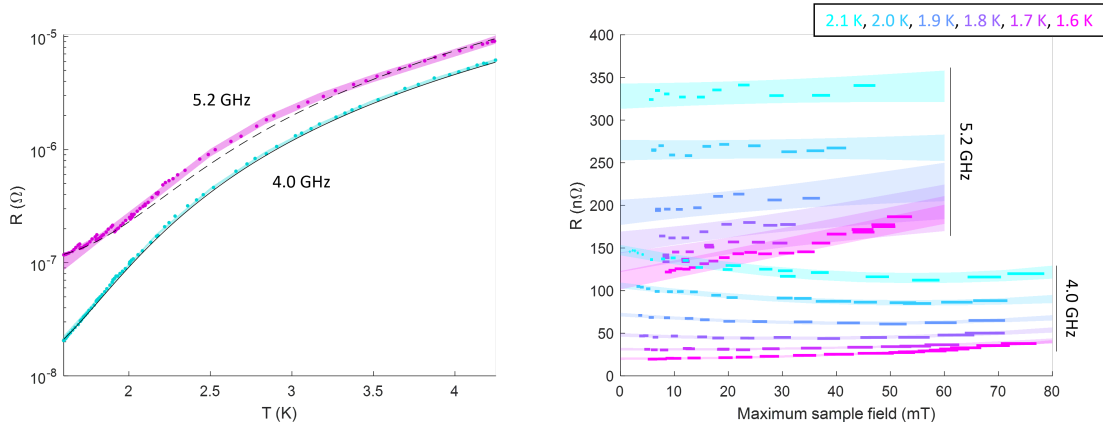
Figure 4.14: Calibration data sets for low field (5 mT – 10 mT) surface resistance temperature-dependence (left) and low temperature (1.6 K − 2.1 K in steps of 0.1 K) surface resistance RF field-dependence (right). Data is presented for both modes of operation at 4.0 GHz and 5.2 GHz. The quantifiable measurement uncertainty in resistance is negligible however the horizontal bars on the right figure indicate uncertainty in the reported field amplitude. The shaded regions correspond to fits used to compare sample measurements at specific fields and temperatures. For the low field temperature-dependence (left) the fit is a fifth order polynomial. For the field-dependent plot (right) the fits are to first and second order polynomials for the 4.0 GHz and 5.2 GHz data respectively. On the left figure the black lines correspond to fitting data to the results of the SRIMP code discussed in section 4.6.2 and indicate reasonable agreement between this data and theoretical expectations

4.6.2 Compare calibration data to theory

To check that the calibration data is reasonable it is fit to a model of surface impedance. The model [Abrikosov et al., 1959] is based on Gor'kov's solution to the BCS Hamiltonian using a Green function method. The relationship between current and vector potential is found assuming the RF field is very small and treating the superconductor as a bulk therefore ignoring surface features or effects brought on by larger amplitude RF fields. The calculation for surface impedance allows for impurities in the superconductor and gives results for diffuse and specular surface scattering. In this work, the surface resistance will be

assumed equal to the average of the resistances predicted by the model calculated with diffuse and specular surface scattering. For the relatively small mean free paths considered here, the difference between the two forms of surface scattering is not significant. The method used here is a MATLAB function [Valles, 2014] adapted from a FORTRAN function [Halbritter, 1970] known as surface resistance with impurities (SRIMP). The results of the model are expected to be similar to those of the standard Mattis-Bardeen calculation [Mattis and Bardeen, 1958, Linden et al., 1994]. This calculation and its results are further discussed in chapter 3.

The material-specific inputs to the model are critical temperature, zero-temperature energy gap, zero-temperature clean limit penetration depth and coherence lengths, and electron mean free path. The penetration depth and coherence length are assumed to be 39 nm and 40 nm respectively [Valente-Feliciano, 2016]. The critical temperature was found to be 9.26 K by measuring changes in magnetic field outside of the cavity at three locations near the host structure and calibration plate as it was slowly warmed from the superconducting to normal conducting state. The mean free path is obtained by fitting to measurements of changes to penetration depth corresponding to changes in resonant frequency as the cavity temperature is increased towards its critical temperature.

The exact expression relating changes in penetration depth to changes in resonant frequency is discussed in section 2.3.3. A vector network analyzer is used to measure the resonance frequency with the coupler positioned far in the cavity to more accurately observe resonances at high temperatures. The resonance frequency of the cavity has a linear relation to the pressure of the cryostat which can vary slightly as the temperature increases. This relation

is obtained by measuring the dependence of resonant frequency on the cryostat pressure at temperatures far below the critical temperature, where penetration depth depends very weakly on temperature so any changes observed are due to the changing pressure. The measured resonant frequencies near the critical temperature are adjusted using this relation to remove any dependence on the cryostat pressure. The zero-temperature energy gap is found by fitting the model to the temperature-dependence of the resistance along with a temperature-independent residual resistance term added the output of the model - that is $R = R_T + R_0$ where R_T is the temperature-dependent component of the total resistance and R_0 is the residual resistance.

The procedure for fitting this model to the calibration data was to first simultaneously fit the electron mean free path to the resonance frequency temperature-dependence near the critical temperature at both 4.0 GHz and 5.2 GHz. Using this mean free path as an input, the temperature-dependence of the measured surface resistances at both frequencies is then fit to determine the zero-temperature energy gap and residual resistances for each frequency. This process is iterated a few times to allow for the parameters to converge. The resulting fit parameters are $l = 131$ nm, $\frac{\Delta_0}{k_B T_c} = 1.9026$, $R_0 (4.0\,\text{GHz}) = 10.71$ nΩ, and $R_0 (5.2\,\text{GHz}) = 102.4$ nΩ. With these parameters the resulting surface resistance of the model is shown as black lines next to the measured data in figure 4.14 and the model results vs measurement for penetration depth in figure 4.15. In both cases reasonable parameters produce good agreement with the observed data. Most notably the temperature-dependence of the resistance in the TE_{012} mode measurement has some discrepancy from the model though it is not a large enough to cause significant doubt in the measurement.
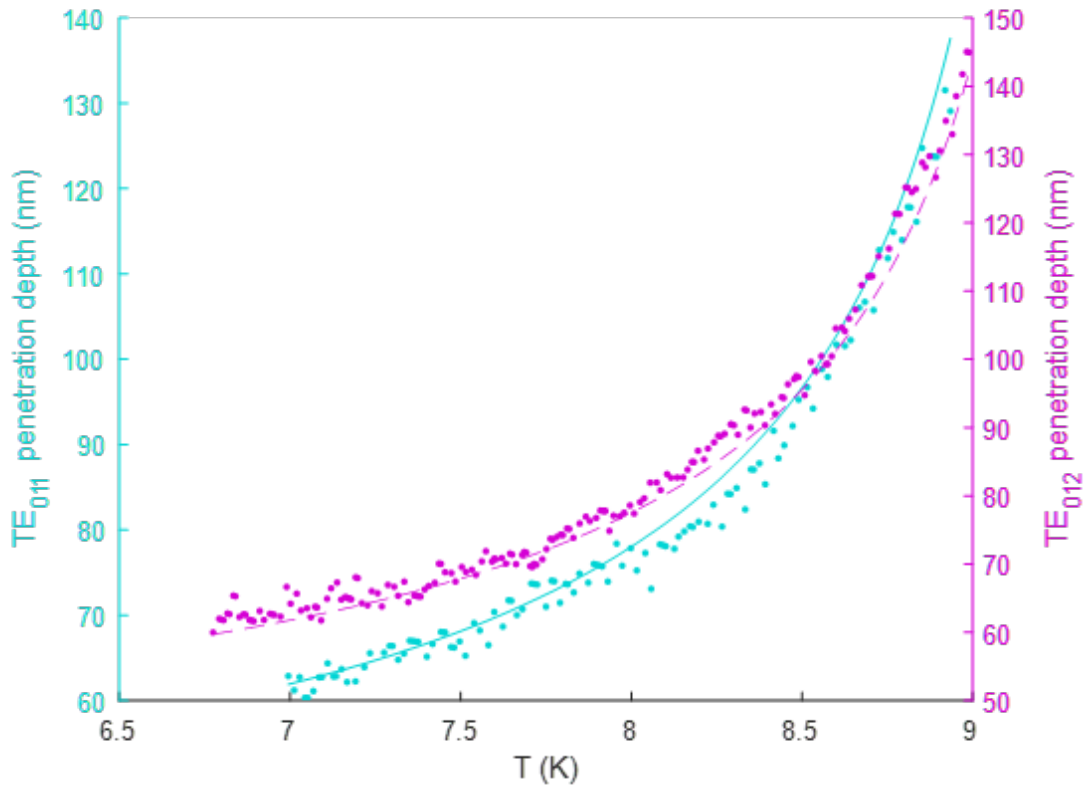
Figure 4.15: Penetration depth of niobium from calibration measurement at 4.0 GHz and 5.2 GHz (dots). The lines represent the prediction from SRIMP [Halbritter, 1970] with parameters fit to the data.

There are currently no models available that reliably predict field-dependent surface resistance. Despite this, fitting the low-field prediction to explore the field-dependence of the surface resistance may be at least qualitatively meaningful. To achieve this, the aim is to fit the field-dependent data at the six temperatures presented in figure 4.14 as a function of the RF field amplitude. Before fitting to the SRIMP model, MATLAB's "linearinterp" model is fit to both the 4.0 GHz and 5.2 GHz data sets. This allows for comparing each of the temperatures at a specific field for the fit to the SRIMP model. Data outside the field range explored in measurement for a given temperature will not be included in the fit. The fit to the SRIMP model is carried out as before, using the mean

free path found above but allowing for the energy gap and residual resistance to vary to extract the field-dependent residual resistance. Subtracting this from the total measured resistance gives the field-dependence of the temperature-dependent component of resistance. Both components of the total resistance are presented in figure 4.16.
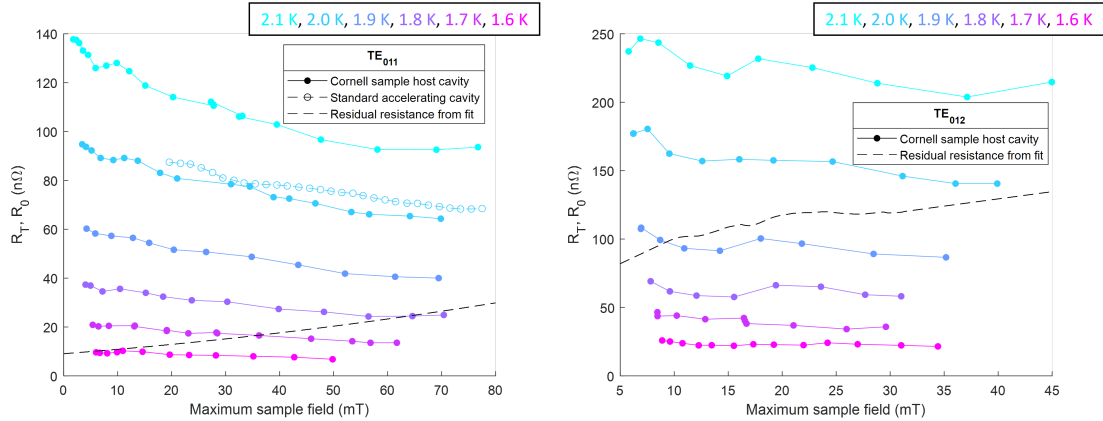
Figure 4.16: Fit of the surface resistance RF field amplitude dependence of figure 4.14 with the SRIMP model to obtain residual resistance, R_0 displayed as black dashed lines, and the zero-temperature energy gap as a function of field (not shown). The routine was carried out individually for 4.0 GHz (left) and 5.2 GHz (right). The temperature-dependent component of the resistance is found as $R_T = R_{meas} - R_0$ and is displayed for each of the measured temperatures. Measurements of a similar niobium surface are reported in literature using a 3.9 GHz TM_{010} mode resonator at 2.0 K [Martinello et al., 2018]. Their results are included here with open circles for comparison. Excellent agreement between the two independent measurements is observed.

Two main conclusions can be drawn from figure 4.16. First is that the data produced with this cavity agrees well with that from a standard niobium accelerating TM_{010} mode cavity with similar preparation measured at another lab [Martinello et al., 2018]. In their work the temperature-dependent resistance component, R_T was likely extracted with a similar procedure. This indicates that the calibration data obtained with the sample host cavity is of reasonable

quality. The second noteworthy feature is the appearance of an anti-Q-slope (anomalous field effect) at 4.0 GHz defined by the surface resistance decreasing as RF field amplitude is increased. This behavior is clearly visible in the raw data at the higher temperatures presented before being obscured by residual resistance. Ignoring the approximations made in using the low field model to fit this relatively high field amplitude data, the anti-Q-slope is even more apparent in the extracted temperature-dependent component of resistance. Normalizing by R_T evaluated at the lowest field measured, it is seen in figure 4.17 at 4.0 GHz that the anti-Q-slope may be independent of temperature in the range studied here. The surprising appearance of anti-Q-slope at 4.0 GHz for a clean niobium surface is not novel and was first reported recently by Fermilab [Martinello et al., 2018]. However, this is the first data reported to reproduce this observation and does so with a TE_{011} mode resonator, indicating that the currently not-understood mechanism giving rise to an anti-Q-slope does not appear to be due to normal electric fields. The behavior at 5.2 GHz is less clear. Looking at the normalized data in figure 4.17 there may be a drop in the resistance comparable to the 4.0 GHz data (noting the range of fields is smaller than at 4.0 GHz) though the behavior is noisy. No reliable 5.2 GHz data is available for comparison.
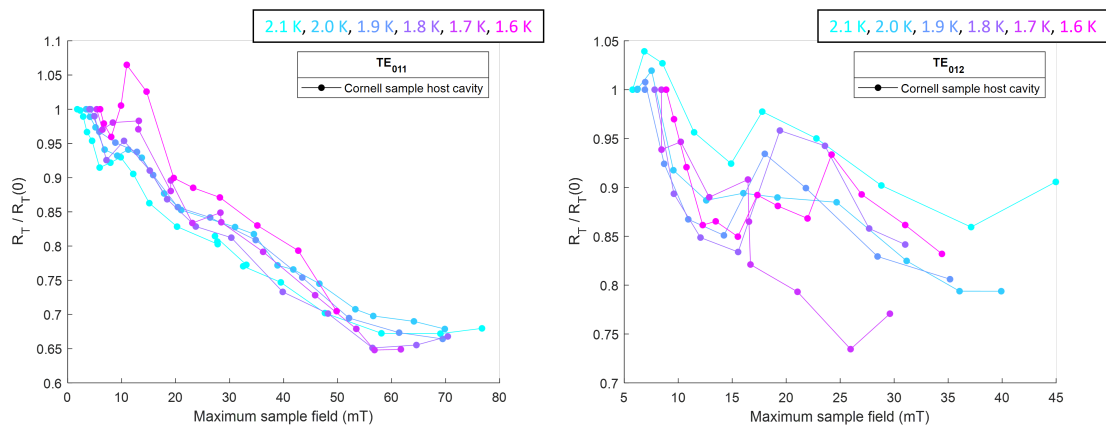
Figure 4.17: The temperature-dependent component of the resistance presented in figure 4.16 normalized to its lowest RF field value. This demonstrates the clear reduction in resistance as RF field is increased at 4.0 GHz (left). At 5.2 GHz (right) a similar reduction may be present but is less clear due to noise and a smaller range of RF field amplitudes.

CHAPTER 5

INITIAL MEASUREMENTS OF THE RF FIELD-DEPENDENT SURFACE RESISTANCE OF PROXIMITY-COUPLED GOLD LAYERS ON CLEAN NIOBIUM

The attempts to improve the capabilities of the Cornell sample host cavity were detailed in chapter 4. While the changes did result in improvements, the intrinsic limitations of a calibrated quality factor measurement still prevent its utility for studying the physics of a sample with low surface resistance relative to the host structure. Created by this limitation is an opportunity to contrive novel studies of samples that are good candidates for the Cornell sample host cavity while still being of interest both scientifically and technologically. Traditionally sample studies are driven by technological goals pushing to minimize surface resistance. The samples of interest for the Cornell sample host cavity, however, are those that go in the opposite direction. An ideal sample would be one possessing relatively large surface resistance ($\sim 2 - 10$ times that of niobium). The challenge is then to identify samples with large surface resistances that view the questions of cutting-edge of superconducting RF research from new perspectives.

This chapter focuses on one of these ideas: the study of the field-dependent surface resistance related to gold layers proximity-coupled to bulk niobium. The connection to accelerator application is primarily one of improved understanding as to the role of the native niobium oxide layer that exists on all niobium accelerator cavities. Specifically, the focus is on the role of the normal conducting niobium oxide phases present in this layer. This concept is not new and measurements and models have been conducted and created attempting to

discover if the oxide layer has an impact on relevant metrics such as the surface resistance magnitude, its dependence on field, or on the quench field of the cavity [Eremeev, 2008, Kubo and Gurevich, 2019, Gurevich and Kubo, 2017]. While compelling connections between the cavity performance and the properties of its surface oxide can be drawn from these studies, it is difficult to separate out the influence of other factors such as changing impurity concentrations due to heat treatments used to alter the oxide and the exceedingly complex structure of the niobium oxide itself.

The idea that will be pursued in this chapter is to replace the niobium oxide with a gold layer. Gold does not oxidize, has a much simpler structure than the niobium oxide resulting in more predictable properties, and does not require heat treatments that can alter impurity concentrations at the surface of the niobium. As such it is expected that the gold layer can be more easily controlled than niobium oxide allowing for more clearly relating any changes to surface resistance to changes to the gold layer properties. Relevant models predict that a strong normal conductor like gold should, at even modest thicknesses, increase the surface resistance of the sample. Thus, it is expected that gold layers could be produced with properties that increase the surface resistance enough for accurate measurement using the Cornell sample host cavity.

Measuring the field-dependence of the surface resistance of a proximity-coupled gold layer chosen with properties leading to large surface resistances may not be directly applicable for SRF application but could provide a more controlled setting for data to be compared to theory. Models describing the surface resistance of a thin normal conductor coupled to a bulk superconductor could apply to both the higher resistance situation as well as the case of the

more complicated oxide structure. Therefore, improving the understanding of one case should result in improved understanding of the other.

The results of the study yielded reasonable low-field agreement with proximity-coupling models for calculating the surface resistance of a structure using acceptable input properties. The field-dependence of the model used as a guide for this work did not agree with the data. No parameter choices used in this model could even qualitatively produce the observed increase in resistance with respect to applied RF field magnitude. Assuming there are no major systematic issues, this indicates that the measurement contains features related to the sample that are not accounted for in the model. It is not clear at this time if these features are due to the intended gold layer or if they are the result of unwanted contamination. The measured field-dependence of surface resistance normalized to an arbitrary value appears to be independent from gold layer thickness. The normalized surface resistance roughly follows a square root relation to the applied RF field amplitude.

This chapter will begin by further motivating the potential impact of niobium oxide on surface resistance and its field dependence. Models describing the surface resistance of a proximity-coupled bilayer are introduced and reviewed. The model used to guide this study, which was heavily based on several of those which are discussed, is developed in detail. Details of the experiment are then given, including the procedure used for replacing niobium oxide with a gold layer and the resulting RF measurements.

5.1 Niobium oxide

The native oxide of niobium has been extensively studied [Halbritter, 1987, Semione et al., 2019, Sun et al., 2022], yet due to its complexity and dependence on surface preparation it remains mysterious. A cartoon image of the native niobium oxide after being exposed to clean air following a 5 hr vacuum bake at 800° C is presented in figure 5.1. While this image is largely an artist's rendering, it is based on information on the chemical makeup of the native oxide obtained by high resolution X-ray photoemission spectroscopy (XPS) studies in conjunction with four-dimensional scanning transmission electron microscopy (4D-STEM) equipped with electron energy loss spectroscopy (EELS). The properties at different heights are studied by removing material via sputtering or by imaging cross-sections of specimens prepared by focused ion beam (FIB). Directly over the niobium is a transition layer consisting of NbO_x ($x < 1$). This layer is very thin (< 1 nm) and is therefore difficult to resolve but it is expected to behave as a metallic normal conductor. It is persistent and even very high temperature treatments do not remove it [McMillan et al., 2020]. Above this is a $1 - 2$ nm layer consisting mostly of NbO_2 and a final $3 - 5$ nm layer consisting mostly of amorphous Nb_2O_5. These upper layers are complicated and included within their disordered structures are metallic phases and non-stoichiometric motifs of the majority phase [Sun et al., 2022].

Conventionally only the bottom oxide layer is considered to be normal conducting while the Nb_2O_5 and NbO_2 are considered insulating and semiconducting respectively [Eremeev, 2008, Semione et al., 2019]. A recent study of valence band mapping imply that the valence band edge is higher than the Fermi level indicating normal conducting properties for all layers [Sun et al., 2022]. It is

thought that the metallic and non-stoichiometric phases present in the disordered structures are what give rise to this normal conducting behavior. If true, this represents a major shift from the conventional understanding of niobium oxide, as the presence of a thicker normal conductor should have more impact on the surface resistance.
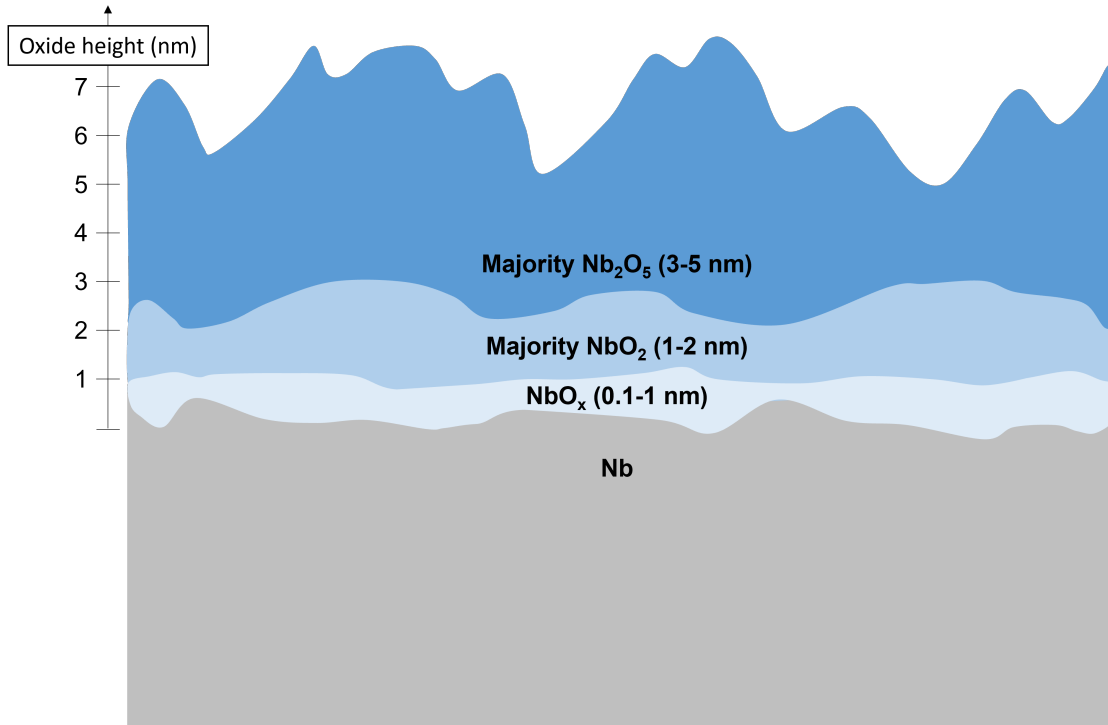
Figure 5.1: Cartoon of a niobium surface after oxidizing following a 5 hr vacuum bake at 800° C emphasizing the current picture of the native oxide structure.

From this discussion it is clear why attempting to understand what role niobium oxide has in SRF cavities by direct measurements have proven difficult. The structure, even if correctly understood, would be extremely challenging to adequately model. In addition, the conventional means by which the oxide structure is altered involves heat treatments which will also affect the impurity concentration in the niobium surface obscuring the role of the changes in oxide structure.

5.2 Cavity measurements of different oxide structures

Some studies have been carried out attempting to probe changes to relevant SRF metrics resulting from modification of the niobium oxide structure [Eremeev, 2008, Posen et al., 2020]. In an effort to demonstrate the potential impact of niobium oxide on the surface resistance relevant portions from the work of Eremeev are discussed in this section. A single 1.3 GHz cavity was assembled to a cryogenic RF test stand modified to include a heating element around the cavity for the purpose of modifying the oxide. Using this setup, the oxide structure is altered by heating the surface and then flowing controlled amounts of oxygen into the system. The corresponding changes to the surface resistance of the cavity could be measured without exposing the cavity to water or air at atmospheric pressure as is done in typical assembly procedures. This process of changing the surface via heating / oxygen exposure in between RF measurements at 1.5 K was then repeated. The results are summarized in figure 5.2. The first measurement (black circle) is the baseline measurement following the assembly of the chemical polished and a high pressure rinsed cavity. Following the baseline three types of surface alteration recipes were performed each followed by an RF measurement. A 400° C vacuum bake for at least 1 hour (represented by circles), exposure of the cavity interior to a small amount of dry air at room temperature (represented by triangles), and exposure of the cavity interior to a large amount of dry air at room temperature to simulate the normal amount present in a cavity assembly (represented by squares). This cycle of treatments was then repeated three times denoted by color in figure 5.2.

As mentioned in the previous section the interpretation of these results is challenging due to difficulty in understanding and controlling the changes in-
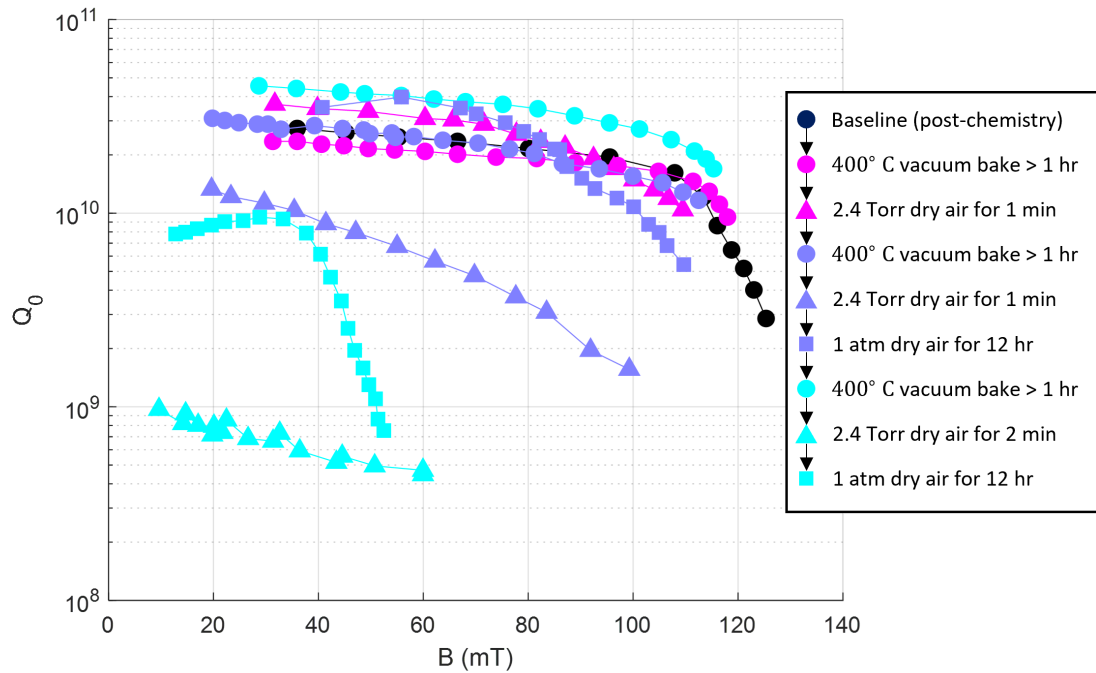
Figure 5.2: 1.5 K RF data corresponding to a single 1.3 GHz TM_{010} mode cavity with a special cryogenic RF measurement setup enabling medium temperature vacuum bakes without the need to break the vacuum seal of the cavity between RF measurements. The cavity was tested after changing its surface via treatments specified in the legend.

duced by each process. After each bake the layers other than the thin NbO_x layer was removed. In addition, it is likely that impurities present in the niobium bulk and surface were redistributed. It is expected that after removing the majority of the native oxide, then flowing different amounts of air at room temperature, the oxide structure would be regrown. It is unclear what properties this regrown layer would possess or how it would affect the persistent NbO_x layer.

From the perspective of the current work the relevant conclusion from Eremeev's study is that changing the oxide structure can, for better or for worse, change the magnitude of surface resistance as well as its qualitative dependence on RF field amplitude. The first generation, shown by the pink curves in figure

, has a relatively mild impact. After this and the second 400° C bake, the effect of introducing a small amount of air at room temperature greatly increased the surface resistance (triangles). This is striking as at room temperature one would expect the only change would be to the surface oxide. When a large amount of air was introduced at room temperature following the minor exposure, the surface resistance was greatly reduced compared to that of the small exposure. Additionally, an apparent anomalous field effect where the resistance decreases with increasing field became visible at low-fields. It is not the aim of this section to speculate on what physical changes are causing the exact shifts or answer the interesting questions, only to imply that the processing leading to the RF data denoted by triangles and squares is likely changing the oxide structure and properties and that these curves demonstrate dramatic shifts in surface resistance resulting from these processes.

5.3 Modeling the surface resistance of a proximity-coupled bilayer

Modeling the surface resistance of a very thin (on the order of $0.1\,\mathrm{nm} - 1\,\mathrm{nm}$) normal conductor proximity-coupled to an underlying bulk superconductor is central to understanding the effect of niobium oxide in accelerating cavities as well as in guiding the proposed study of gold layers. A well-constructed model can provide quantitative predictions for comparison with a carefully conducted experiment. Models will also indicate which of the many parameters of the bilayer system should be the focus of a systematic study and can guide what parameter ranges will have larger surface resistances as desired for accurate

measurement using the Cornell sample host cavity.

In this section a brief literature review of relevant models is presented. By combining some of these models a surface resistance was calculated for the normal conductor - superconductor bilayer system. The details of this calculation and results are given. The results are organized to motivate the choices made for gold layer parameters and the analysis of data coming later in this chapter.

5.3.1 Review of existing calculations

A series of models [Gurevich and Kubo, 2017, Kubo and Gurevich, 2019] were the inspiration for the gold layer study of this chapter. These models specifically consider the niobium oxide, its role in current data, and methods by which its control could lead to future improvements. The properties of the superconducting and normal conducting layers are calculated. The thermodynamic Usadel equation can be used, assuming the dirty limit and the response of the metals is much faster than the RF period. Since they focus on the very thin NbO_x layer they speed up the calculation by replacing the solution in the normal layer with a surface boundary condition approximating the effect of a very thin normal layer on the superconducting properties. The surface resistance is obtained by plugging the solutions to the Usadel equation into the local limit case of the surface resistance model by Nam [Nam, 1967a,b]. In the model by Kubo the standard Usadel equation is modified to include the pair-breaking effects of a strong magnetic field. To the author's knowledge this model is the only existing attempt at calculating surface resistance of a proximity-coupled normal layer system in the presence of nontrivial RF magnetic fields. The primary con-

clusion of this work relevant to this thesis is the expectation that pair-breaking effects (including a normal conductor at the surface or the induced screening currents due to a strong RF field) can lower surface resistance at low-field and may be a mechanism to explain the anomalous field effect (anti-Q-slope) [Hein, 1999, Grassellino et al., 2013]. Further details of this model are delayed to the following section as this model is nearly identical to what was used there (with the exception of replacing the boundary layer as a normal conductor).

A similar model making use of the thermodynamic Usadel equations was developed aiming to describe the utility of proximity-coupled bilayers for kinetic inductance detectors [Zhao et al., 2017]. This model does not restrict its focus to very thin normal layers and solves the Usadel equation in both the normal conductor and superconductor domains. The method to calculate surface impedance differs in the decision to use a transmission line model to incorporate the electrodynamics of the layers and their internal inhomogeneity. The conductivity used in the transmission line picture is calculated using the conductivity of Nam's model [Nam, 1967a,b] identically to the previous model. This work considers very small RF fields and does not account for any of the effects introduced by a large field.

One of the more sophisticated models for a low-field normal conductor - superconductor bilayer is that of Belzig [Belzig et al., 1998, 1999]. The superconducting properties are calculated using the Eilenberger model and the calculation of the surface impedance allows for non-local electrodynamics. Thus, it can explore a wide range of material purity.

A final model considered was that of Pambianchi and Anlage [Pambianchi et al., 1994, Pambianchi, 1995] which aimed to consider relatively thick normal

conducting films in the low-field limit. This series of work developed a model for the effective penetration depth of a proximity-coupled bilayer using the generalized London equation (generalized to an inhomogeneous material) based on intuition of the proximity effect changes to the pairing potential. The surface resistance was then calculated based on a combination of the penetration depth result and the classic Mattis-Bardeen model [Mattis and Bardeen, 1958]. This model has shown good agreement with low-field experiments [Pambianchi et al., 1995, 1996].

5.3.2   Model implemented for the gold layer study

To guide the target parameters and data analysis of the proximity-coupled gold layer study a model was implemented. It primarily follows that of Kubo & Gurevich with some exceptions. Similar to the model of Zhao, it does not replace the effect of the normal layer on the superconducting properties with a boundary condition. This is to allow for the option to more carefully handle thicker normal layers if that became of interest to the study. For the purposes of the work presented here all layers were thin and the boundary condition approximation would have been sufficient. The field is assumed to decay exponentially into the material and is assumed to remain constant in the normal layer. For the thin normal layers used in this study this is a reasonable approximation. Here the details of the model and the methods of calculation are specified in order to be transparent. The cited models above provide a more complete description but the discussion here attempts to efficiently convey the important features of the model and convey all stages of the numerical calculation.

The problem can be divided into two distinct phases. First the superconducting properties are obtained for the situation of interest. Next these properties are combined with electrodynamics to calculate the surface resistance or dissipation. The properties of the superconducting system are calculated including the effects of the proximity-coupling and its response to a nonzero surface magnetic field. Both effects exhibit a strong position-dependence controlled by a coherence length for proximity-coupling and a magnetic penetration depth for the applied field. The Usadel equations are used to calculate the general properties and include these effects as they are general enough to calculate the position-dependence while being simple enough for relatively basic calculation.

The geometry used in this model is shown in figure 5.3. It consists of a normal conducting layer of thickness, d, Fermi velocity, $v_{f,n}$, and conductivity, σ_n. Anticipating a very thin normal layer the mean free path, l_n, is not specified. In this study it is expected that $d \ll l_n$ so scattering will more frequently occur at layer interfaces than with impurities in the normal layer. A contact resistance, R_B, is specified between this normal layer and a semi-infinite bulk superconductor. Contact resistance is defined as the product of the electrical resistance between the two layers multiplied by the contact area (perhaps it would be more clear to call it contact resistivity, but here the notation of Kubo & Gurevich is followed). The specified bulk superconductor properties include its Fermi velocity, $v_{f,s}$, normal conducting state conductivity, σ_s, mean free path l_s, critical temperature T_c, zero temperature energy gap, Δ_0, Debye frequency Ω, and a Dynes parameter, Γ [Dynes et al., 1978, 1984]. Following Kubo & Gurevich, the normal conducting layer is assumed to have the same values for Γ and Ω. For both layers the electron effective mass is assumed to be the standard free electron value. The incident RF magnetic field amplitude at the surface will be denoted as B_0

with frequency, f. Finally, the temperature is specified.
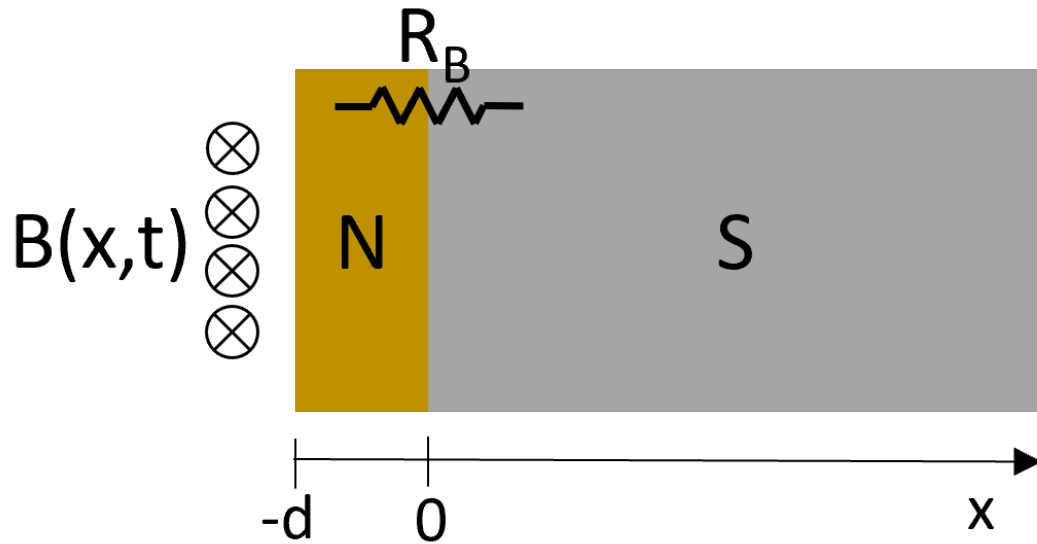
Figure 5.3: Diagram of proximity-coupled bilayer demonstrating relevant dimensions and parameters

The model is based on the Usadel formulation, which provides an approximate solution for the equations of motion of the BCS Hamiltonian in the quasiclassical ($\Delta \ll E_f$) and dirty ($l \ll \xi$) limits [Usadel, 1970]. This approach results in a differential equation that can be solved to obtain two Green functions that define the superconducting state. Green functions describe the propagation of a particle in time (energy) and space (momentum). The superconducting state is described by a combination of quasiparticle excitations and Cooper pairs. Accordingly, the "normal" Green function conveys information about the quasiparticle excitations while the "anomalous" Green function describes electrons participating in Cooper pairs [Belzig et al., 1999]. Knowledge of these Green functions can be used to calculate the properties of the superconducting state. Different types of Green functions exist that can be useful in different situations. In this work the relevant Green functions will be the imaginary time or Matsub-

ara Green function and the retarded Green function. For the derivation of the Usadel equation and complete descriptions of the various types of Green functions, the reader should make use of a dedicated text [Kopnin, 2001].

The calculation begins by obtaining the position-dependent pairing potential in the superconductor and a position-dependent "penetration depth" in both layers. It is convenient to use the imaginary-time Green functions for this purpose as will be seen later. To simplify the numerical calculation, the Green functions are parameterized by a newly introduced variable, $\theta_n(x) = \theta(x, \hbar\omega_n)$ following a standard method [Belzig et al., 1999]. Here x is the distance from the normal conductor - superconductor interface towards the superconducting interior (figure 5.3). The index, n, corresponds to the temperature-dependent Matsubara frequencies, $\omega_n = 2\pi \frac{k_B}{\hbar} T \left(n + \frac{1}{2}\right) - \Gamma$. Γ is the phenomenological Dynes parameter that incorporates a finite quasiparticle lifetime into the model [Dynes et al., 1978, 1984]. It is employed here mainly to assist the numerical calculation and is kept much smaller than the bulk superconducting pair potential. The imaginary-time normal and anomalous Green functions are given by $G_n(x) = G(x, \hbar\omega_n) = \cos\theta_n(x)$ and $F_n(x) = F(x, \hbar\omega_n) = \sin\theta_n(x)$ respectively. For each Matsubara frequency the Usadel equation in region i (normal conductor or superconductor) becomes [Kubo and Gurevich, 2019]

$$\frac{\hbar D_i}{2} \frac{\partial^2 \theta_n}{\partial x^2} = \hbar\omega_n \sin\theta_n - \Delta\cos\theta_n + s\sin\theta_n\cos\theta_n \tag{5.1}$$

The material dependent diffusion coefficient, $D_i = \frac{v_{f,i} l_i}{3}$ [Kopnin, 2001], is defined from the material's Fermi velocity, v_f and mean free path, l. It can also be expressed as $D_i = \frac{\sigma_i}{2\nu(E_f)e^2}$ in terms of the conductivity, electric charge, and density of states at the Fermi level using the Drude model expressions for electron density, $n = \frac{1}{3\pi^2}\left(\frac{mv_f}{\hbar}\right)^3$, single-spin density of states, $\nu(E_f) = \frac{1}{2\pi^2\hbar^3}m^2 v_f$, and conductivity, $\sigma = \frac{ne^2 l}{mv_{f,i}}$.

Equation 5.1 is the standard Usadel equation referenced previously with an extra term that mixes the normal and anomalous Green functions with a coefficient *s*. This term attempts to encode pair-breaking effects into the model such as those induces by paramagnetic impurities [Kubo and Gurevich, 2019]. In this model paramagnetic impurities are neglected but, following Kubo, it is used to encode the pair-breaking screening currents induced by the magnetic field [Kubo and Gurevich, 2019].

$$s = 4\pi^2 \Delta_0 \left(\frac{B(x,t)}{\phi_0/(\lambda_0 \xi_0)} \right)^2$$

Where $\phi_0 = \frac{\pi \hbar}{e}$ is the magnetic flux quantum, Δ_0 is the zero-temperature pair potential deep in the superconductor (far from surface effects), $\xi_0 = \sqrt{\frac{\hbar D_s}{2\Delta_0}}$ is the zero-temperature dirty-limit coherence length, $\lambda_0 = (\pi \mu_0 \Delta_0 \sigma_s / \hbar)^{-1/2}$ is the zero-temperature dirty-limit superconductor penetration depth [Gurevich and Kubo, 2017], and $B(x,t)$ is the RF magnetic field. Here it is assumed the fields decay exponentially after entering the superconductor. This implicitly assumes that the effect of the higher fields and the normal layer on the penetration depth of the superconductor is negligible. Further it is assumed that the field is constant in the normal layer. In general, these are likely weak assumptions though it should be reasonable for extremely thin normal layers at low-field [Pambianchi et al., 1994]. These assumptions are also the justification for not calculating the pair-breaking term, *s*, in both layers but just using the superconductor value. Explicitly $B = B_0 \exp\left(-\frac{x}{\lambda}\right) \sin(\omega t)$ in the superconductor and $B = B_0 \sin(\omega t)$ in the normal conductor. ω and B_0 correspond to the angular frequency and amplitude of the magnetic field incident on the surface respectively. It is critical that the reader be aware that for the solution to this differential equation it was assumed that $\lambda = \lambda_0$. Thus, the results here are restricted to relatively low temperatures (approximately half the critical temperature where the penetration depth does

not vary much with temperature) which is fine for the intended studies. Later in the process when calculating surface resistance, the resulting imaginary-time Green functions will be used to calculate penetration depth more carefully. A more careful analysis could perhaps calculate the more exact penetration depth here and plug it back in then repeat until results relax to steady values. This procedure was not studied extensively in this work but for the parameter ranges examined the correction from its implementation was minimal.

The pair potential in the superconductor is obtained via the self-consistency equation. Here the form used in the model by Zhao is used in favor of that in the work of Kubo and Gurevich. Note that while the proximity-coupling effect can induce nonzero energy gap in the excitation energies available in the normal conducting layer, the pair potential is zero. A common misconception is that the pair potential is equal to half of the energy gap but this is not always the case.

$$\Delta(x) \ln\left(\frac{T_c}{T}\right) - 2\pi k_B T \sum_{\substack{\omega_n > 0}}^{\omega_n \leq \Omega} \left(\frac{\Delta(x)}{\hbar \omega_n} - \sin \theta_n\right) = 0, \qquad x > 0$$

$$\Delta(x) = 0, \qquad x < 0$$

Here Ω is the Debye frequency of the superconductor. Since the pair potential is included in the Usadel equation for each n and is itself a function of a series of θ_n it is necessary to simultaneously solve a system of equations including the full range of the summation in the self-consistency equation with equation n corresponding to $0 < \omega_n \leq \Omega$.

The solution to this system of equations is carried out with boundary conditions which are now specified. At the vacuum interface ($x = -d$) the boundary condition is chosen such that no current flows normal to the interface (no cur-

rent into the vacuum).

$$\frac{d\theta_n}{dx}\bigg|_{x=-d} = 0$$

For the normal conductor - superconductor interface ($x = 0$), general results based on the Eilenberger formulation are used [Kuprianov and Lukichev, 1988].

$$\sigma_n \frac{d\theta_n}{dx}\bigg|_{x=0^-} = \sigma_s \frac{d\theta_n}{dx}\bigg|_{x=0^+}$$

$$\sigma_n R_B \frac{d\theta_n}{dx}\bigg|_{x=0^-} = \sin\left[\theta_n\left(x = 0^+\right) - \theta_n\left(x = 0^-\right)\right]$$

Here $x = 0^-$ and $x = 0^+$ represent the location immediately to the left and to the right of the interface respectively. Note that σ_n is the normal conducting layer conductivity and the n does not correspond to the Matsubara frequency index.

Deep in the superconductor bulk (ideally $x = \infty$ but for numerical simplicity it was specified to be $x = 10\lambda_0$) the Green functions return to their form in the case of a homogeneous alloy at zero applied field. Specifically, the solution to equation 5.1 for $s = 0$ and $\frac{d^2\theta}{dx^2} = 0$.

$$\theta_n(x = \infty) = \tan^{-1}\frac{\Delta}{\hbar\omega_n}$$

The numerical solution was carried out using MATLAB's multipoint boundary value problem solver. The initial guesses used were $\theta_n = 0$ in the normal conducting layer, corresponding to $F_n = 0$, and the bulk value $\theta_n = \tan^{-1}\frac{\Delta}{\hbar\omega_n}$ in the superconducting layer described above in the discussion of boundary values. This segment of the solution yields a position-dependent pair potential, $\Delta(x)$, and will also be used to calculate a position dependent penetration depth when calculating the surface resistance.

For calculating the local density of states and surface resistance the expressions used require the retarded normal and anomalous Green functions. These

can be obtained by solving equation 5.1 with the substitution $\hbar\omega_n + i\hbar\Gamma \rightarrow -i\epsilon$ and utilizing the pair potential obtained from the above procedure. Here $\epsilon = E - E_f$, where E is the quasiparticle excitation energy, E_f is the Fermi energy, and Γ is the Dynes parameter defined above. Making the substitutions the Usadel equation for the retarded normal and anomalous Green functions parameterized as before, $G^R(x, \epsilon) = \cosh\theta^R(x, \epsilon)$ and $F^R(x, \epsilon) = \sinh\theta^R(x, \epsilon)$ respectively, becomes

$$\frac{\hbar D_i}{2}\frac{\partial^2\theta}{\partial x^2} = -i(\epsilon + i\hbar\Gamma)\sinh\theta^R + i\Delta\cosh\theta^R + s\sinh\theta^R\cosh\theta^R$$

This single differential equation is solved with input parameter ϵ ranging from 0 to $1.8\Delta_0$. The boundary conditions and initial guesses after substitution are identical to the imaginary case except the bulk condition becomes $\theta^R(x = \infty) = \tanh^{-1}\frac{\Delta}{\epsilon + i\hbar\Gamma}$. The resulting θ^R can then be used to obtain the density of states and surface resistance.

The local density of states for quasiparticle excitations in layer i normalized to its normal conducting value at the Fermi level is found from the real part of the retarded normal Green function $\nu(x, \epsilon) = N_i(x, \epsilon)/N_i^{NC}(E_f) = \text{Re}\left\{G^R(x, \epsilon)\right\} = \text{Re}\left\{\cosh\theta^R(x, \epsilon)\right\}$.

The surface resistance is calculated from a sophisticated calculation by Nam based on Eliashberg theory [Nam, 1967a,b]. The limiting case employed here assumes the decay of the field can be described by an exponential and no decay is seen in the normal layer, diffuse surface scattering, local electrodynamics (which is implied from using the dirty limit Usadel equations), and that the equilibrium Fermi distribution is sufficient to describe the quasiparticle energy distribution. This calculation is for low-field surface resistance and therefore does not consider high-field effects such as the changing of quasiparticle energy

levels which could be an issue for its application to the high-field case considered here [Deyo et al., 2022]. The surface resistance will be given in terms of a local conductivity.

$$R_s = \omega^2 \mu_0^2 \lambda^2 \left(\int_{-d}^0 \sigma_1 dx + \int_0^\infty \sigma_1 \exp\left[-\frac{2x}{\lambda}\right] dx \right) \tag{5.2}$$

Here the penetration depth λ can be different than the value previously used, λ_0, and is calculated from the solution to the imaginary-time Usadel equation [Gurevich and Kubo, 2017].

$$\lambda_i(x) = \left(\frac{4\pi\mu_0 k_B T \sigma_i}{\hbar} \sum_{\omega_n > 0}^{\Omega} |F_n(x)|^2 \right)^{-1/2}$$

This is the penetration depth corresponding to screening in the superconducting layer. For the thin normal conducting layers considered in this study it is found that corrections to the effective penetration depth of the bilayer from including the normal conducting response are minimal. For most situations of interest, it was found that the penetration depth did not vary substantially from the bulk value despite the spatial variation of the superconducting properties near the normal conductor interface. For results discussed here and in the coming sections the penetration depth deep in the bulk, was used.

σ_1 is the real part of the complex conductivity and was calculated following the calculation by Nam with simplifications to the form by Kubo and Gurevich.

$$\sigma_1 = \frac{\sigma}{\pi\hbar\omega} \int_0^{\pi/\omega} dt \int_{-\infty}^\infty d\epsilon M \frac{1 - \exp\left(-\frac{\hbar\omega}{k_B T}\right)}{\left[1 + \exp\left(-\frac{\epsilon}{k_B T}\right)\right]\left[\exp\left(\frac{\epsilon}{k_B T}\right) - \exp\left(-\frac{\hbar\omega}{k_B T}\right)\right]}$$

Where σ is the conductivity in the appropriate layer and the spectral quantity M is defined as

$$M = \text{Re}\left\{G^R(\epsilon)\right\} \text{Re}\left\{G^R(\epsilon + \hbar\omega)\right\} + \text{Re}\left\{F^R(\epsilon)\right\} \text{Re}\left\{F^R(\epsilon + \hbar\omega)\right\}$$

The resulting surface resistance and its field-dependence depend strongly on the many input parameters. In general, the qualitative behavior can be broken into three behavioral regimes having small, medium, and large contact resistance. Qualitatively what is meant here by this relative magnitude scale of the contact resistance depends on the other input parameters of the model and will be developed in the coming discussion. Parameters chosen for motivating the gold layer study while simultaneously demonstrating the field-dependence behaviors are listed in table 5.1.

Layer	N	S
T_c (K)		9.2
$\frac{\Delta_0}{k_B T_c}$		1.76
l (nm)		6
σ (S/m)	10^8	7.1×10^6
v_f (m/s)	1.4×10^6	1.4×10^6
d (nm)	1.5	
R_B ($\Omega \cdot \text{m}^2$)	—-	
$\hbar\Gamma$		$0.005\Delta_0$
$\hbar\Omega$		$11\Delta_0$
T (K)		2
f (GHz)		4
B (mT)	—-	

Table 5.1: Parameters used for model demonstration.

The resulting predictions for surface resistance are displayed in figure 5.4. Here the surface resistance is normalized to the result of the model in the case of no normal conducting layer. The surface resistance in the zero-field limit is given as a function of the contact resistance. Here three behavioral regimes of the model can be clearly distinguished. For high contact resistances the two metals are effectively disconnected so the normal conducting layer behaves electrically as a normal conductor resulting in a relatively large dissipation. At low contact resistances the proximity-coupling effects in the normal conductor result in greatly reduced dissipation lowering the total surface resistance. The inter-

mediate contact resistance regime occurs where there is an anomalous spike in the zero-field surface resistance above that corresponding to the decoupled normal conductor. This is the typical dependence of surface resistance prediction on the contact resistance. The predicted resistance is at a steady minimum for the high coupling (small R_B) range, spikes to a high value for the intermediate coupling range, and then relaxes to the decoupled limit at high R_B. The relative magnitude of the predicted surface resistance in each region can change as well as the range of contact resistances over which of the intermediate range is observed. This form of dependence with contact resistance is almost always observed unless the normal layer Dynes parameter is made large (corresponding to a shorter quasiparticle lifetime).

The right side of figure 5.4 demonstrates the field-dependence of the surface resistance and how it changes with contact resistance. For the strong proximity-coupling range the surface resistance prediction is fairly constant with field. The high contact resistance regime usually sees a slight increase in the resistance as the field is increased. Most notably is the intermediate contact resistance range where the surface resistance is reduced from the low-field peak value to that corresponding to the normal conducting being weakly coupled to the superconductor. Going to higher fields than those explored by figure 5.4 usually causes increases in the resistance in all of the contact resistance behavioral regimes.

To better understand the surface resistances predicted by this model, consider the corresponding local density of states shown in figure 5.5. Here the rows are the density of states predicted for a system with low, intermediate, and high contact resistance (from top to bottom). The left and right columns correspond to the zero-field and high-field prediction. The black dashed line is

156
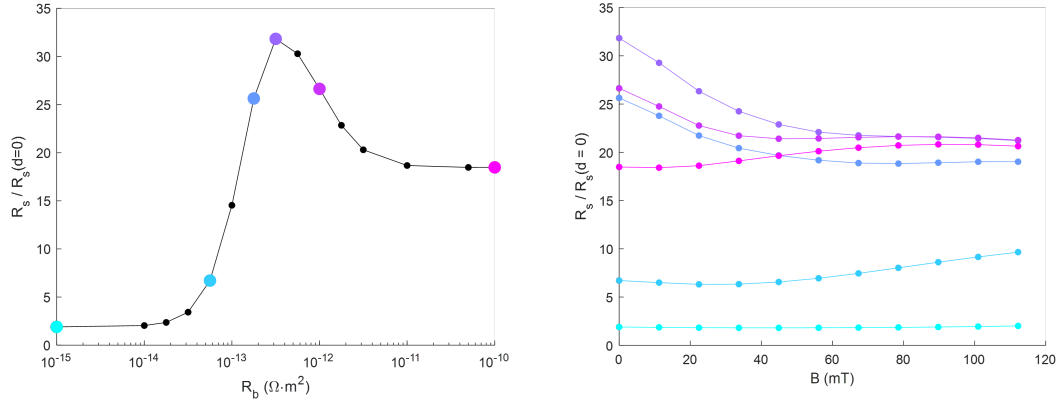
Figure 5.4: Predicted surface resistance with parameters listed in table 5.1 normalized to the value with no normal conducting layer. The left plot shows the predicted normalized surface resistance in the zero-field limit dependence on contact resistance. The right plot shows the field-dependent normalized surface resistance with specific contact resistances. The colors correspond to those on the left side and can be matched directly to the zero-field limiting case.

the density of states at the interface in the normal layer. The remaining curves are the local density of states in the superconducting layer at various distances from the metal-metal interface. In the density of states corresponding to the low contact resistance regime it is clear that the normal layer has a superconducting density of states with a complete energy gap which indicates it will have a similar excitation spectrum to a superconductor resulting in low dissipation. In the high contact resistance range, the electrical connection between the two layers is effectively blocked so that the proximity-coupling between the two layers does not occur. This is evident from the normal conducting density of states being constant (over the relatively small energy scale for a normal conductor). Here the normal layer behaves as a normal conductor and is responsible for the relatively increased surface resistance seen at this range in figure 5.4. For the intermediate contact resistance range, the two-peak density of states seen in the low-field intermediate contact resistance density of states is indicative of the

157

surface resistance exceeding that of the fully decoupled normal layer but does not explain its occurrence. In the work of Kubo, this feature is attributed not to the density of states but to the real part of the anomalous Green function and how it enters the calculation of conductivity in the spectral function [Kubo and Gurevich, 2019]. At high fields the intermediate contact resistance density of states in the normal layer approaches the decoupled limit and explains why the corresponding surface resistance approaches its corresponding decoupled limit.

It is clear from figure 5.5 that the proximity-coupling effect does not only induce relevant changes in the normal layer but the density of states in the superconducting layer is reduced in height and the peak become broader near the interface. This can cause changes in the surface resistance of the superconducting layer. For most cases considered in this study the resulting changes to the superconductor layer contribution to surface resistance were small compared to those of the normal conducting layer.

5.4   Preparation of proximity-coupled samples

For the purposes of this study the target sample is one with higher surface resistances, appropriate for measurement with the Cornell sample host cavity, that probes potentially interesting properties. If the model predictions are accurate then a proximity-coupled bilayer with properties in the intermediate contact resistance range would be expected to have a large surface resistance that reduces notably as RF field increases. This would be perfect for study with the Cornell sample host cavity as it would be easier to resolve the details of its surface resistance and would provide further understanding as to the potential effects of
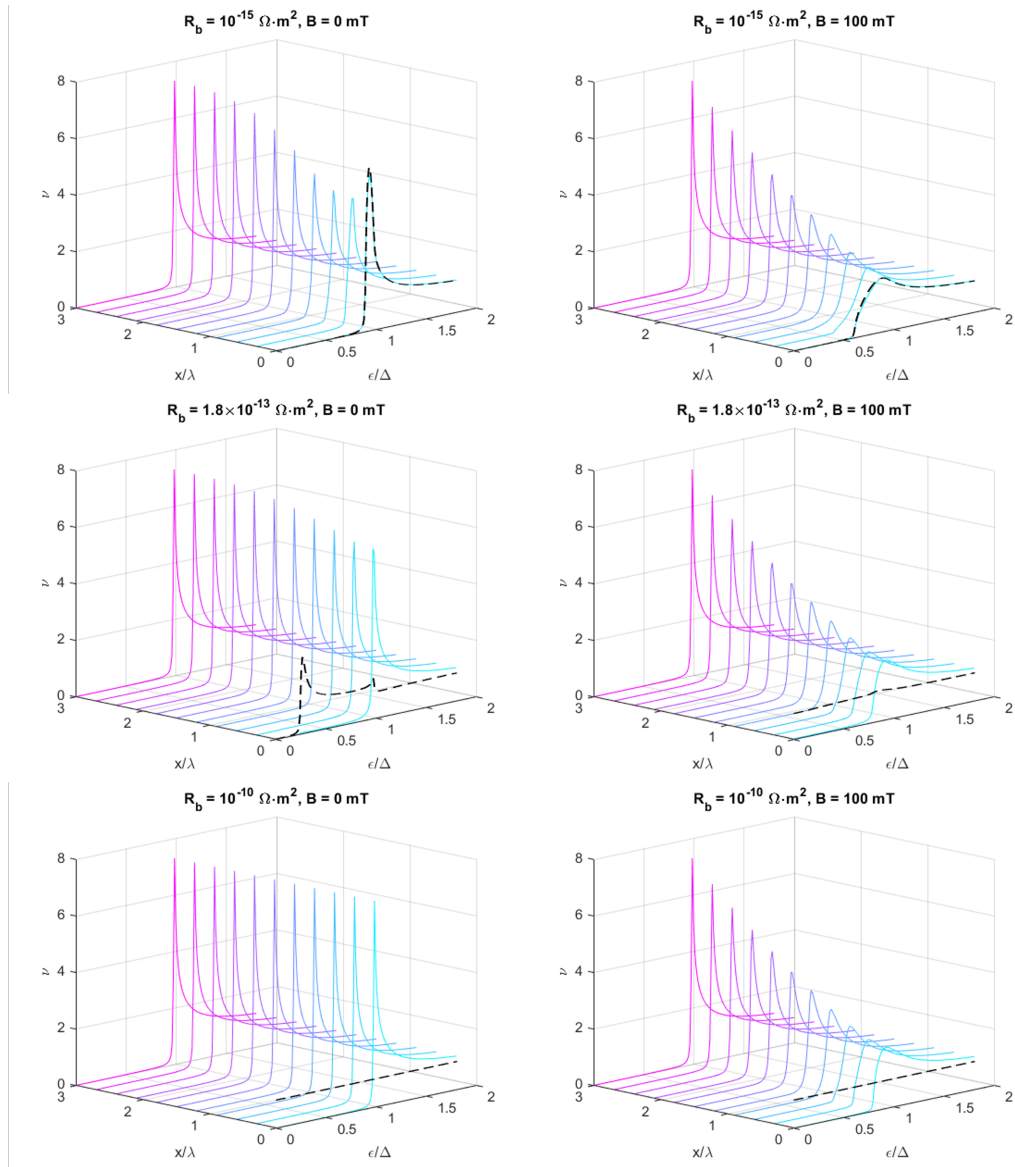
Figure 5.5: Local density of states predictions with the properties specified in table 5.1. ϵ is the quasiparticle excitation energy relative to the Fermi level and x is the distance from the metal-metal interface demonstrated in figure 5.3. The black dashed line is the value at the interface in the normal layer. The others are in the superconducting layer. The top, middle, and bottom figures correspond to the low, intermediate, and large contact resistance behavioral regimes specified in the text. The plots on the left and right correspond to zero magnetic field and high magnetic field respectively.

normal conducting layers present in SRF cavities. This understanding could be valuable for guiding future cavity research directions.

For a gold layer with set internal properties (σ, l, v_f, etc.) and contact resistance, the intermediate contact resistance regime will change with thickness as demonstrated in figure 5.7. The plan for the study was to create this situation experimentally; that is, to measure the surface resistance of a proximity-coupled bilayer while changing the thickness of a normal conductor with all other properties constant. A niobium substrate was prepared by removing its native oxide and replacing it with a gold layer. The gold layer pacifies the surface preventing further oxidization. The thickness of this gold layer is gradually increased. Between each addition to the gold layer thickness an RF measurement will be carried out to measure how a normal conductor thickness impacts surface resistance in a proximity-coupled bilayer. It is assumed that the contact resistance will not change with gold thickness. This contact resistance could be increased by adding a very thin insulating layer prior to the initial gold deposition but this study only examines a layer with the lowest readily accessible contact resistance. If successful this study would provide better understanding on what role a normal conductor has in the total surface resistance in a proximity-coupled system under strong RF fields.

5.4.1   Gold layer deposition

The deposition of the gold layer can be broken into two stages. First the native oxide layer had to be removed in order to study the proximity-coupled gold-niobium system without the effects of the normal conducting oxide phases. This also was required to decrease the contact resistance between the gold and niobium. Second the gold layer must be deposited onto the niobium in a way that does not allow for the oxide to regrow before the gold can passivate the surface.

A similar but low-field study of the surface resistance of proximity-coupled systems accomplished both of these steps via sputtering. A niobium film was sputtered onto a substrate then, without breaking vacuum, a normal conducting film was sputtered on top [Pambianchi et al., 1995, 1996]. This procedure would reduce the contact resistance but sputtered thin film niobium tends to be inferior to bulk niobium. Specifically, its dependence with RF field amplitude can be more dramatic than bulk niobium with typical preparation [Valente-Feliciano, 2016]. The study discussed in this chapter focuses on field-dependence so bulk niobium was used to isolate potential field-dependent effects resulting from the proximity-coupling of the gold.

The niobium substrate used was a fine grain 3 mm thick disk. The first $100\,\mu$m were removed via electropolishing (EP) to create a smooth surface and eliminate any contamination embedded in the original surface from its manufacturing. The EP procedure used was described in section 4.5.2. Following this chemical procedure the plate was baked at $800\,$C in ultra-high vacuum (UHV) for out-gassing. Finally, a $4\,\mu$m EP was performed to remove any contamination introduced by the furnace without introducing significant concentrations of hydrogen from the acids in the solution. Following this the sample plate was measured on the Cornell sample host cavity to act as a baseline measurement. Unfortunately, after this measurement it was necessary to reset the host structure which significantly altered its surface resistance due to unrelated issues with the flange where the sample attached to the host. The resistance of the baseline measurement cannot be directly compared to the gold layer measurement but information about the quench field should still be relevant.

The native oxide is present on the surface of the sample plate during the

baseline measurement. It was necessary to remove it and deposit a gold layer without exposing it to air. To do this the niobium sample was loaded into a glove box filled with nitrogen at atmospheric pressure. The sample was left in diluted Hydrofluoric acid (HF) (1 % in DI water) for 30 minutes to remove the oxide. The chemical treatment was necessary since heat treatments are unable to remove the most relevant portions of the oxide [McMillan et al., 2020]. The HF was cleaned off of the sample surface using methanol. It was then left to dry in the nitrogen atmosphere before being sealed into a plastic bag for transport to a gold deposition system. At this point it is expected that the surface has not oxidized and is bare niobium.

To obtain a very thin and uniform gold layer on this substrate a CVC SC4500 combination thermal / electron beam evaporation system was used. The sealed bag with the niobium substrate was placed in the chamber. A nitrogen purge was turned on and flowed for some time. The chamber was opened just enough to reach in to remove the sample from the sealed bag and place the sample on the stage as quickly as possible. Some oxide may form in this procedure but ideally it will be minimized by the nitrogen flow. The chamber was then evacuated to a pressure of 10^{-6} Torr. The gold deposition rate of this system is 0.01 nm/s. The final thickness was monitored by calibrated Quartz Crystal Control. The slow deposition rate was used with this method to control the final thickness to be 0.1 nm. To clean the gold ingot surface 15 nm was pre-deposited.

The sample plate was then prepared for RF testing using a DI water high pressure rinse (HPR) and carrying out all steps of the assembly in a cleanroom environment as is typical. Following the initial RF test the sample plate was removed from the cavity, the indium gasket was scraped away using copper

edges, and the sample was high pressure rinsed with DI water prior to depositing more gold. There was a danger of contaminating the RF surface with indium between depositions. The sample was cleaned with the DI water HPR prior to its initial gold coating and between each subsequent deposition to reduce the risk of microscopic indium flakes or any other contaminants being present. This procedure was then repeated to obtain surface resistance measurements of proximity-coupled systems with gold layers having nominal thicknesses 0.1 nm, 0.5 nm, 1.0 nm, 1.5 nm, and 2.0 nm.

5.4.2   Measurement of contact resistance

To measure the contact resistance between the gold and niobium layers on the sample plate used for the RF measurements a second sample was prepared with an identical process to that described in section 5.4.1. This 1 cm × 1 cm sample may not have the exact contact resistance of the larger plate used for the RF study but should provide a reasonable estimate. The removal and suppression of the surface oxide was identical but some changes were made when depositing the gold to enable the measurement of contact resistance. Specifically, a mask was placed over the niobium surface before depositing the gold to create contacts and a thicker gold layer of 50 nm was used to ensure successful connection to the probes. The mask produced rectangular strips with dimensions of 7.5 mm × 1 mm to be used to measure contact resistance. The resulting structure is shown in figure 5.6.

The contact resistance was obtained at cryogenic temperature using a Quantum Design DynaCool physical properties measurement system (PPMS). The

resistance was obtained using a four-probe measurement using the system's AC resistivity measurement (with the probe spacing and contact area specified to be 1 cm and 1 cm^2 respectively) . The low temperature results of this measurement are shown in figure 5.6. The resistances shown here are between the two strips on the left side of the sample.
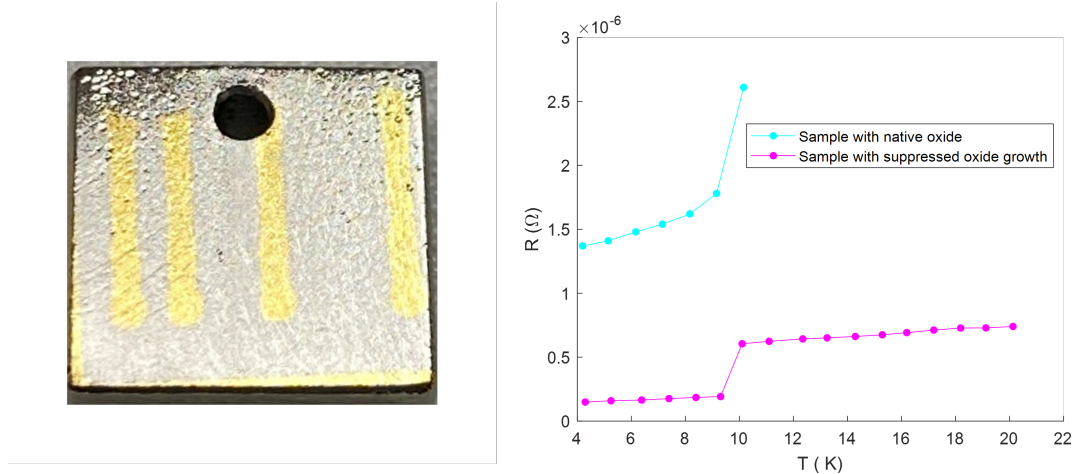
Figure 5.6: Measurement of contact resistance expected for the gold-niobium bi-layer. (Left) A 1 cm × 1 cm sample prepared identically to the larger sample plate used for RF measurement described in section 5.4.1. The gold stripes are 50 nm thick and have areas roughly equal to 7.5 mm^2. (Right) The resistance corresponding to connections made on the two left-most strips obtained by a four probe AC measurement. The total resistance when the niobium is in its superconducting state is expected to be entirely due to the contact resistances of the two strips. A separate sample was prepared (not shown) without attempting to remove the native niobium oxide for comparison.

In the superconducting state at the low frequencies (∼ 100 Hz) of the measurement the contribution to the total resistance from the niobium will be negligible. The gold layer's contribution should be significantly less than the reported resistance due to its small thickness. Specifically for a conductivity of 10^8 S/m at 4 K the resistance for the 7.5 mm × 1 mm × 50 nm geometry would be on the order of 10^{-11} Ω. Therefore, the only contribution to the measured resistance when the niobium is superconducting will be the contact resistance

at the interface between the two contacts. Assuming this contact resistance is equal and uniform for both contacts this gives $R = 2R_{contact}\left(\frac{1}{A_1} + \frac{1}{A_2}\right)$. Here A_1 and A_2 are the areas of the contacts roughly having area $A = A_1 = A_2 = 7.5\,\mathrm{mm}^2$. It is assumed that current flows through the entirety of the contact area which may not be valid but provides a lower bound estimate. Using this with the 4.2 K measured resistance of figure 5.6 the contact resistance is expected to be roughly $R_B = 5.6 \times 10^{-13}\,\Omega \cdot \mathrm{m}^2$. As a control a second sample was prepared with gold layers deposited onto niobium without making an effort to remove the native oxide. The contact resistance of this sample obtained in the same way yields $R_B = 5 \times 10^{-12}\,\Omega \cdot \mathrm{m}^2$.

This measurement is intended to be a rough estimate and there is no guarantee that the value reported here is truly uniform or accurately reflects that of the larger sample used in the RF measurements. But it does give a guide as to what range of values may be expected and by comparing it to the control sample (with gold deposited over the native oxide) it does indicate that the deposition method is at least reducing the thickness of the niobium oxide if not entirely preventing it.

5.4.3 Comments on the realized sample

Before discussing the RF measurements, the expectations for the surface resistance given the contact resistance measurement of the previous section are considered. Figure 5.7 indicates the expected behavioral regime for the proximity-coupled system using parameters that are able to partially explain the low-field surface resistance measurements in the next section. The parameters are given

in the discussion of figure 5.11 and are essentially those of table 5.1 modified to better represent the expected clean niobium surface and its measured critical temperature. Anticipating that the gold film thickness will be much less than its mean free path due to impurity scattering it is expected that its conductivity will be greatly reduced from the bulk value and will increase with film thickness. The conductivities used in figure 5.7 are chosen from the results demonstrated in figure 5.12 such that the model prediction agrees with low-field surface resistance measurement. Based on literature they are expected to be within a reasonable range as is discussed in section 5.5.4.
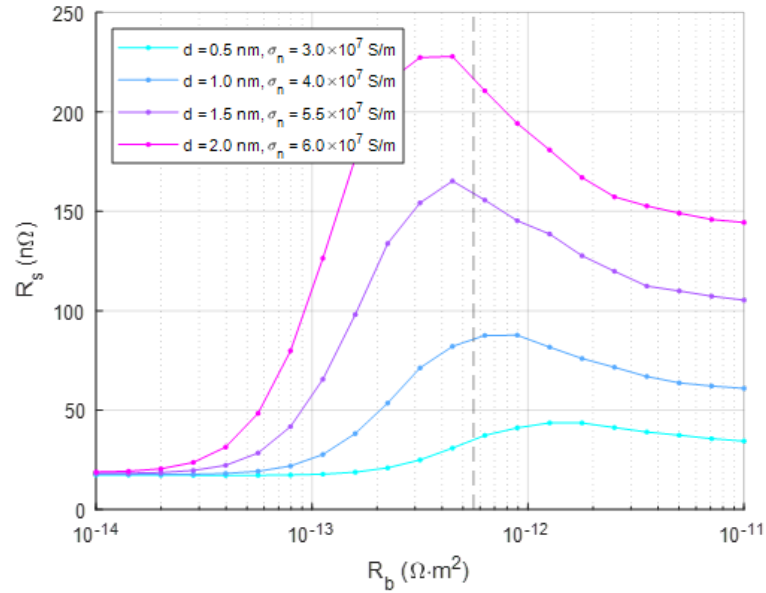
Figure 5.7: Surface resistance calculated from equation 5.2 at 4.0 GHz and 1.6 K using parameters listed in the discussion of figure 5.11. The black dashed line indicates the approximate expected contact resistance of the experiment. The thicknesses and conductivties were chosen to be within the range of agreement between measured data and the simulation for the expected contact resistance as indicated in figure 5.12. This figure demonstrates how the location and nature of the behavioral regimes predicted by the model can vary with input parameters and demonstrates that for reasonable parameters the sample considered in this study could be in the desired intermediate contact resistance range.

In figure 5.7 the black-dashed line indicates the contact resistance measured in section 5.4.2. The model predictions indicate that, for the chosen parameters, this contact resistance would place the sample in the desired proximity-coupling range for some of the thicknesses explored. Notice that the location and shape of the intermediate proximity-coupling range changes as the normal layer thickness (and corresponding conductivity) changes. For the thinnest layer the sample may be to the left of the peak and as the thickness increases it will move to the right and pass through the peak. If the experimental situation is truly represented by the parameters used in this discussion, then the field-dependence demonstrated in figure 5.4 for the intermediate contact resistance range should be expected.

5.5   RF measurements of the gold layer study

This section presents the surface resistance of the sample prepared as described in section 5.4.1. The expected gold thicknesses are 0.1 nm, 0.5 nm, 1.0 nm, 1.5 nm, and 2.0 nm. The Nb plate was given the typical preparation described in section 4.5.2. Interestingly measurements were performed with its native oxide before and after electropolishing $4\,\mu$m following the five hour $800°$ C vacuum bake. The importance of this step in the preparation was just discovered prior to carrying out the gold-layer deposition and this was done while attempting to understand the relevance of the process. Unfortunately, due to an issue with the host structure flange it had to be modified and the host structure surface was reset to eliminate contamination introduced from the needed chemical work. This reset included the $4\,\mu$m electropolish on the host structure following its five hour $800°$ C bake. There is no baseline measurement that has the same host structure

surface as that which was used with the gold layer measurements. The existing baseline measurements do provide similar low-field resistances and can be used for rough comparison. Further the quench fields, if they occur on the sample plate (which is expected since it was dependent on sample plate) can be directly compared.

The measured surface resistance at low fields can be made to agree with predictions from the model of 5.3.2 using reasonable parameters. But there are too many inputs and unknowns so this becomes a somewhat trivial exercise. The predicted field-dependence is not seen in the data. No parameter ranges studied could produce even qualitatively similar results as the field increased. There are many possible explanations of the discrepancy which range from defects in the sample, extrinsic sources introduced by the cryostat, real sources from the gold layer that are not included in the model, or issues with the model itself.

Most importantly the quench field observed for the minimum gold thickness appears to be higher than the baseline measurement, as well as similar niobium plates studied, for both frequencies. To the best of the author's knowledge this is a real effect of replacing a significant fraction of the metallic native oxide with a thinner gold layer and was not caused artificially by systematic issues.

5.5.1 Quality factor measurements

The resulting RF measurements of the sample plate prepared according to section 5.4.1 at 1.6 K are given in figure 5.8. With the exception of the calibration which was performed on a separate sample plate all of the measurements reported in this figure are for the same substrate with the specified modification

made to the surface. The baseline measurements attempted to quantify the surface resistance of the niobium with its native oxide. These were performed before and after a $4\,\mu$m electropolish (EP) after the high temperature vacuum bake which removes impurities introduced by the furnace as discussed in 4.5.2. The host structure surface was reset due to an issue with its flange after these baseline measurements so the quality factors of the baseline measurements cannot be directly compared with the gold sample data. Despite this there is some overlap since the host structure surface is similar before and after its reset. The main change comes from the addition of the post-bake electropolish which removes contamination that led to increased reduction of quality factor as the field increases. At low-field the resistance of the host structure should be similar - though it would likely be slightly lower with more impurities present prior to the light EP. The measurement of quench field is not expected to be affected by the change of host structure surface and are directly compared with those of the sample after gold layer deposition. The calibration data, which was measured with the same host structure surface and has the same preparation as sample plate prior to the gold deposition, is expected to be a better indication of the surface resistance with a native oxide and will be used for this purpose in coming sections.

At 4.0 GHz the baseline measurement after electropolishing has similar quality factor to the 0.1 nm gold thickness measurement at low fields. At 5.2 GHz the quality factor is notably higher after the 0.1 nm gold layer deposition though for this frequency it is found that residual resistance varies strongly between samples. From this data it appears that the surface resistance of a sufficiently thin gold layer is at worst comparable to the niobium with its native oxide and at best could actually reduce it. As more gold is added the low-field resistance

quickly is increased resulting in the reduced quality factors of figure 5.8.

The field-dependence of the quality factor for different gold thicknesses could suggest that field-dependent features activate at low fields. A rapid decrease in Q_0 is observed until a field that seems to decrease as the gold thickness increases. For the 0.1 nm thickness it is not observed, but for each subsequent thickness iteration the drop in quality factor is sharper and the field where the slope changes is lower. This effect is most clear at 4.0 GHz but is also visible at 5.2 GHz. This has not been studied further as a part of this work so the nature of the mechanism can only be speculated on. Some ideas include entry of flux vortex loops or an abrupt weakening of the proximity-coupling effect due to increased screening currents and magnetic field.

As the RF field amplitude increases the 0.1 nm Au layer maintains a higher quality factor than all other measurements. The most striking result is the apparent enhancement of the quench field observed at both frequencies. With this thin gold layer passivating the surface from oxide growth the quench fields become 105 mT at 4.0 GHz and 65 mT for 5.2 GHz. For typical niobium plates the quench field is 70 mT − 80 mT at 4.0 GHz and 50 mT at 5.2 GHz. Rarely it increases beyond this, for example, the baseline measurement prior to the postbake EP also has an anomalously high quench field of around 90 mT at 4.0 GHz and 55 mT at 5.2 GHz. Interestingly the light EP after the furnace treatment reduces the quench field from this high value to the typical range. While this indicates the sample plate used for the gold layer study does have a capacity for anomalously high quench fields it is the result of this study that a very thin gold layer replacing the niobium oxide substantially increased the quench field beyond both the typical range and the high value seen for the baseline.
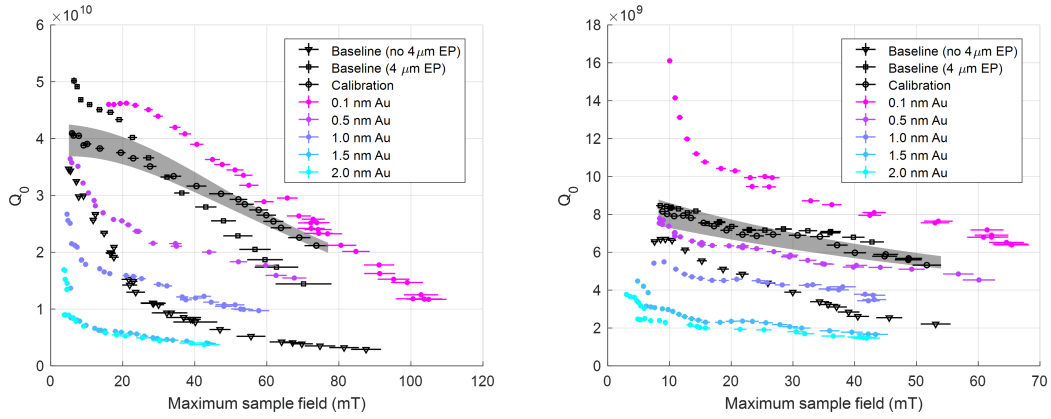
Figure 5.8: Intrinsic quality factor measured at 1.6 K and 4.0 GHz (left) and 5.2 GHz (right). All measurements were performed on a single niobium sample plate including its baseline measurement and then with a gold layer replacing the native niobium oxide prepared according to section 5.4.1 except for the calibration described in section 4.6. The calibration data is shown in addition to the calibration polynomial fit (shaded regions) used for surface resistance extraction in later sections. The baseline measurements were carried out with and without a 4 μm electropolish (EP) after the high temperature vacuum bake. The host structure surface was reset between the baseline measurements and those where the native oxide was replaced with gold so direct comparison of the quality factor magnitude should be done carefully. All samples were limited by quench indicated by the highest field in the figure.

This claim, that replacing the niobium oxide with a very thin gold surface has increased the quench field, is remarkable. As such it is important to consider if this is due to any other effects. Specifically, if there were any systematic issues that led to artificially high quench fields. To the best of the author's knowledge this is not the case and increased quench fields are a real effect of the gold layer replacing the niobium oxide.

Various metrics of RF measurement quality were considered. The external quality factors of both the forward power coupler (FPC) and the transmitted power coupler were obtained via combining quality factor and coupling factor measurements and plotted against the input power. As expected, there was lit-

tle variation in these values with RF power. Before each sample is measured at a given frequency, attenuation measurements are made on the cables between the power meters, amplifier, and the cavity. If there are issues with these attenuation measurements it could lead to inaccurate RF field data. These attenuation measurements showed little to no variation between the eight samples considered in figure 5.8.

The only systematic variation occurred after the 1.0 nm gold thickness measurement and was only a small shift in one of the RF paths. It is possible that following the attenuation measurements of the 0.1 nm gold measurement the RF system was reassembled in a way that had a faulty connection or some other form of issue changing the attenuation from the measured values. This is unlikely to explain both frequencies having an enhancement since the two frequencies are measured using mostly different RF system components and their attenuation measurements are done separately. The attenuation of the RF path inside the cryostat going to the cavity can be obtained by comparing forward power measurements coming from the amplifier with the reflected power when the cavity is driven off-resonance. This procedure is detailed in chapter 2. These measurements are both made for every data point in figure 5.8 to monitor any changes in the attenuation of the coaxial line that can occur with changing temperature and power. While the resulting attenuation does change anomalously between sample measurements, it is not expected to have led to the increase in quench field. The changes in attenuation appear to be connected to the anomalous behaviors of the FPC discussed in chapter 4. While these changes were observed throughout this study, the fact that the shifts in attenuation do not appear to change the reported quench fields in any other measurements of figure 5.8 indicates it is unlikely to have caused the enhancement. More importantly

the anomalous coupling behavior only occurs at one frequency at a time and therefore should not cause enhancement in both frequencies.

Lastly a third niobium sample plate was prepared after the gold layer study was completed and displayed nearly identical quench fields to the calibration measurement shown in figure 5.8. This third measurement had the opposite FPC behavior from the original calibration. While none of this discussion can prove the quench field enhancement reported here is real it is the author's hope that it demonstrates that an attempt was made to verify the claim in the hopes that this effect can be studied more and reproduced.

5.5.2   Field-dependence of surface resistance

The surface resistance of the gold layer samples can be extracted according to the procedure discussed in chapter 4. The results are displayed in figure 5.9. The 0.1 nm gold sample cannot be accurately converted due to its apparent surface resistance being too low to be accurately resolved. The systematic error leads to negative values for many of the data points of this sample at both frequencies. The remaining four iterations of the study have significantly higher surface resistance and appear to be resolved reasonably well. Still there is likely some unaccounted systematic error that can lead to relative shifts in the surface resistance between the samples. Naively it is expected that the sample with a thicker gold layer would result in higher surface resistances. With the exception of the step from 1.5 nm to 2.0 nm driven by a 4.0 GHz field this trend is observed. This indicates that systematic errors, while present, are not expected to dominate the measurement.
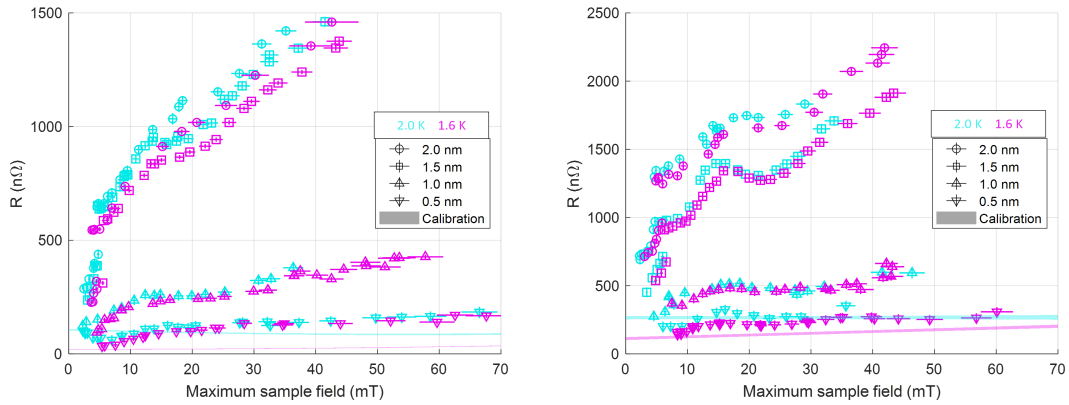
Figure 5.9: Extracted sample surface resistance of thin gold layers deposited over bulk niobium at 1.6 K (cyan) and 2.0 K (pink) driven by RF fields at 4.0 GHz (left) and 5.2 GHz (right). All measurements were performed on a single niobium sample plate with a gold layer replacing the native niobium oxide as described in section 5.4.1 except for the calibration which was a separate niobium sample plate. The 1.6 K data is that shown in figure 5.8 and was limited by quench. The maximum fields at 2.0 K were intentionally lower than the quench field since they were done prior to the 1.6 K measurement and the surface resistance can sometimes increase following a quench. This has been observed at 5.2 GHz but does not seem to be an issue at 4.0 GHz. In some cases, quench fields were reached earlier than expected.

The difference between 2.0 K and 1.6 K is small compared to the increase in the overall resistance. This will be discussed in more detail in the next section. The surface resistance increases quickly with RF field amplitude, which is not the expected result from section 5.3.2. Despite this there are noteworthy features in the field-dependence. As described in the previous section there is an abrupt jump in surface resistance at low fields for the 1.5 nm and 2.0 nm measurements at both frequencies. This jump is not as dramatic for the smaller thicknesses but there is an increase in the low-field slope. At approximately 15 mT the field-dependence tends to become somewhat flat for all measured gold layer thicknesses and at both frequencies. At 5.2 GHz the resistance sometimes drops slightly but this effect is possibly a systematic issue as is discussed in a later

section. As the field increases to higher values, this plateau region transitions into an increase in surface resistance with respect to the RF field. This data indicates the field-dependence of the gold layer samples is nontrivial. Some of its structure could be introduced by the system, especially at 5.2 GHz. However, the overall increase is expected to be real as it is consistent with the naive expectation that thicker gold layers should lead to increased surface resistance.

5.5.3 Temperature-dependence of surface resistance

The low-field temperature-dependence of the gold layer surface resistances was measured and is presented in figure 5.10. This figure focuses on temperatures higher than of the measurements in figure 5.9. For high temperatures the dissipation in the niobium is far stronger and, based on the similarity between the values reported for the gold layers and their similarity to each-other and the calibration, appears to be dominant over any contributions from the thin gold layers. In this case the resolution of the host cavity is limited resulting in significant measurement error which obscures detailed analysis based on this data. However, some rough conclusions may be drawn.

At both frequencies the surface resistance, even at high temperatures, tends to increase with the gold layer thickness. Exceptions to this could be explained by considering the dramatic increase in surface resistance with RF field amplitude observed in figure 5.9 at low RF field amplitudes. For example, at 4.0 GHz the 1.5 nm surface resistance is high compared to the 2.0 nm data. From the lower segment of figure 5.10 it is clear that some of the anomalously high surface resistance measurements for the 1.5 nm film may be the result of being driven

by a relatively large RF field compared to that of the corresponding 2.0 nm data.

As discussed in figure 5.8 the 0.1 nm gold layer appears to have lower surface resistance than the calibration niobium sample with the typical native niobium oxide. From figure 5.10 this reduction becomes more apparent at low temperatures indicating that the improvement comes from reducing a small feature that does not greatly impact the bulk niobium properties. This assertion is consistent with the replacement of the native niobium oxide with an extremely thin gold layer and indicates that dissipation in the native niobium oxide could be important for optimizing niobium surface resistance.
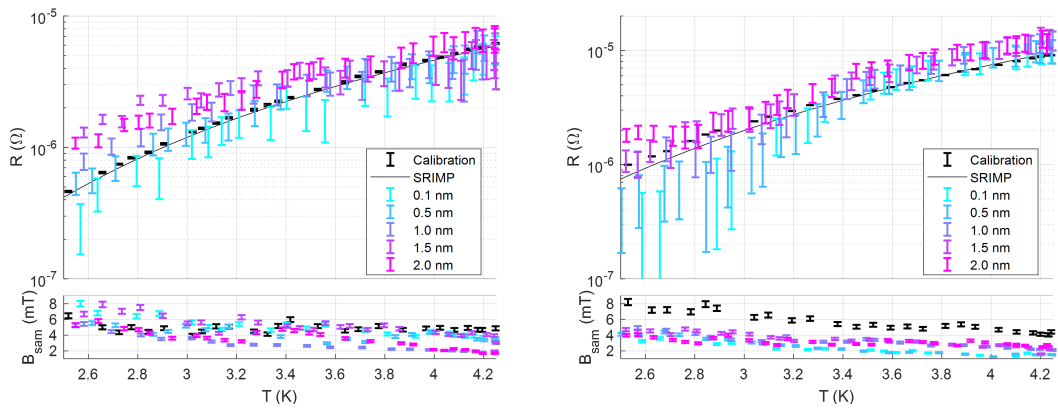
Figure 5.10: Extracted sample surface resistance of gold layers deposited over bulk niobium as described in 5.4.1 plotted as a function of temperature at 4.0 GHz (left) and 5.2 GHz (right). The RF magnetic field amplitude at which each measured resistance was obtained is presented below the surface resistance data. The niobium calibration and its fit using SRIMP [Halbritter, 1970] are plotted as a reference.

As a first pass at RF field-dependent analysis assume the measured surface resistance can be described by the sum of its temperature-dependent and temperature-independent contributions. That is $R_{total} = R_T + R_0$ where R_T denotes the temperature-dependent contribution and R_0, the temperature-independent portion, will be denoted as the residual resistance. The residual resistance can be eliminated by considering the difference between the resistances at 2.0 K and

1.6 K which is done in figure 5.11. These curves were obtained by fitting a linear interpolation to the 1.6 K data and then subtracting this from the 2.0 K data at a given RF field amplitude. The uncertainty displayed here is twice the measured uncertainty at 2.0 K. This assumes the statistical uncertainty for the 2.0 K and 1.6 K data is similar and ignores any contribution from the linear interpolation. The niobium calibration plate with a native oxide is included for reference. Any real information of this analysis is lost in noise but some discussion can be attempted. At 4.0 GHz there is an apparent shift above the niobium calibration for the two thicker gold layers of the study while the two lower thickness measurements are below that of the baseline. This dependence on gold layer thickness is the opposite of that which is predicted by the model in section 5.3.2.

The model results are more intuitive and indicate that the change in surface resistance as a function of temperature should be larger for low thickness normal conductors and will increase as the gold layer thickness is increased. The parameters used for these predictions were chosen based on literature while making slight adjustments to better agree with the data. Unless otherwise specified the values of table 5.1 were used. The niobium T_c and mean free path were changed to the values of the calibration measurement, 9.26 K and 100 nm. The niobium conductivity increases accordingly with mean free path. The contact resistance was that measured in section 5.4.2, $5.6 \times 10^{-13} \, \Omega \cdot m^2$. The gold layer conductivity was set to 10^8 S/m which may be slightly high but is not unreasonable. It is important to note that the model predictions were offset so that the prediction of the niobium surface with no normal conducting layer (black line) would match the corresponding SRIMP model predictions [Halbritter, 1970]. This was done to account for the expected discrepancy between the dirty-limit model with the relatively clean niobium layer. Naively one would expect the

niobium surface resistance to be largely unchanged by the gold layer thickness (for the thicknesses considered here) so the change in predicted surface resistance with respect to gold thickness should be due to the gold layer itself. As the thickness increases the proximity-coupling becomes less effective leading to less temperature-dependence in the surface resistance.
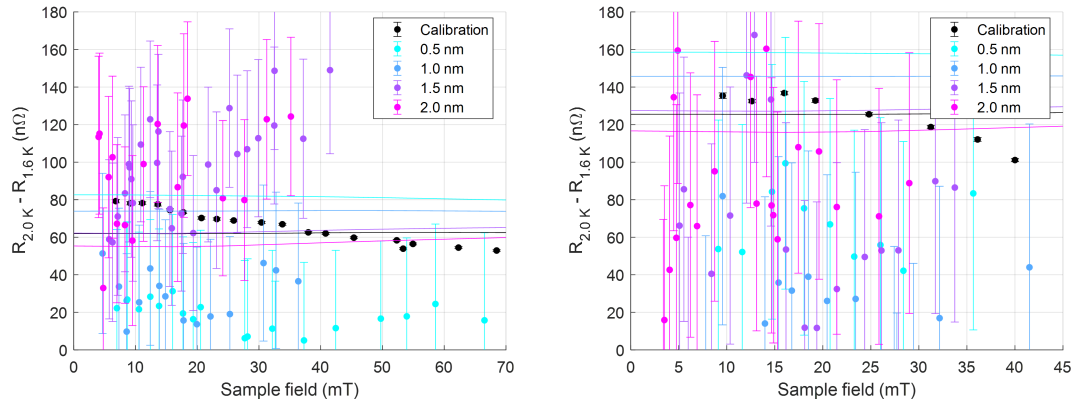
Figure 5.11: Difference between the 2.0 K and 1.6 K surface resistance measurements of figure 5.9 at 4.0 GHz (left) and 5.2 GHz (right). The black points are the calibration Nb sample with native oxide while the others correspond to the samples of differing gold layer thickness. The 1.6 K data was fit with a linear interpolation which was then subtracted from the measured 2.0 K data. The statistical uncertainty displayed here is twice that of the 2.0 K measurements. The lines are the predictions from the Usadel equation formulation in section 5.3.2. These predictions were offset by 33 nΩ and 78 nΩ for 4.0 GHz and 5.2 GHz so that the predictions from the SRIMP model [Halbritter, 1970] agreed with the Usadel-based model prediction with no normal layer (black line).

The uncertainty in the measurements prevents resolution of the measured field-dependence for the temperature-dependent component of the surface resistance. The model predicts it should be essentially independent of field. The noisy data can at least claim that the measured values have an upper bound on any potential field-dependence differing from the model prediction though this does not do much for the analysis. Primarily figure 5.11 is included not to

assert agreement between data and model but to convey the model prediction and to indicate that the temperature-dependent component of the resistance is smaller than the residual resistance for much of the field-range explored. Most importantly this discussion has clearly indicated that the apparent increases in total surface resistance with respect to gold layer thickness are likely explained by a residual resistance. The next section considers whether the results can be explained by dissipation strictly in the thin gold layers or if there are further complications.

5.5.4   Gold layer contribution to surface resistance

To explore the measured surface resistance and compare it to models, the discussion should be turned to the contribution to the total surface resistance coming from the normal conducting layer. The prediction of this quantity is readily obtained from the first integration in equation 5.2. To estimate this normal layer contribution experimentally, assume that the surface resistance contribution from the niobium layer is roughly independent on the properties of the normal conductor. For the relatively large contact resistance expected and the thin gold layers considered in this study this may be a reasonable approximation. Thus, to obtain the measured surface resistance corresponding to the normal layer it can be argued that subtracting the surface resistance of the niobium substrate from the total value will yield the desired value.

The exact properties of the niobium substrate used in the gold layer study are not known. Because of the previously mentioned mechanical issue the host structure had to be reset between the measurements of the sample plate with the

native oxide (baseline measurement) and with the gold layer samples. A reasonable approximation for the surface resistance of the niobium substrate used in the gold layer study should be the niobium plate used for the calibration which was prepared identically (prior to the gold deposition). In either case any role of the native oxide must be ignored. There has been only one other measurement of a niobium sample plate performed after the conclusion of the gold layer study. By comparing the results of the measurement on this new niobium plate with that of the calibration plate some information can be obtained about how much variation may be expected between niobium plates with similar preparation. From this single point of comparison, it appears that little variation is expected at 4.0 GHz (approximately 10 nΩ of residual resistance) but more significant change may be present for the 5.2 GHz mode (ignoring any possible systematic error, approximately 400 nΩ at 1.6 K). The source of the difference between the calibration plate and the new niobium plate at 5.2 GHz is unknown and could be due to systematic variations such as trapped flux dissipation or issues with the RF path to the cavity. More plates would need to be studied for a confident discussion. This lack of consistency at 5.2 GHz is troubling, but regardless of the source, it can be treated as a systematic error in the subsequent analysis and does not appear to be significant enough to obscure meaning from the gold layer study.

Comparisons between the measured normal layer contribution to the net surface resistance and the model predictions from equation 5.2 are presented in figure 5.12. The thin dashed and solid lines correspond to the model predictions with a proximity-coupled gold layer and a completely decoupled normal layer respectively. For the model predictions identical input parameters were used as those described in the discussion of figure 5.11. The proximity-coupled layer

again uses the contact resistance of $5.6 \times 10^{-13}\,\Omega \cdot \text{m}^2$ from 5.4.2. This parameter range corresponds to the anomalous behavior described in section 5.3.2 where the surface resistance with proximity-coupling exceeds that of a decoupled layer as is clear in the figure. The measured normal layer resistance contribution obtained as described above is presented here as a thick line superimposed over model predictions, indicating what conductivity would produce a surface resistance where the model agrees with the data. The longer thick lines correspond to the full range of measured surface resistances for each gold layer including all fields explored. The shorter thick lines correspond only to the surface resistance measured at the lowest field and its uncertainty.

While no attempts were made to measure the bulk conductivity of the gold films resulting from the thermal evaporation described in 5.4.1 a value of $2.7 \times 10^8\,\text{S/m}$ can be inferred from the reported room temperature conductivity and mean free path in literature describing similar gold films [Gilani and Rabchuk, 2018]. The actual conductivity could vary from this value but it is expected to be a reasonable guide. This value is represented in figure 5.12 by the vertical lines on the right end of each plot. The thickness of the gold films in this study are expected to be much less than the mean free path corresponding to the above bulk conductivity, $l_n = 37.7\,\text{nm}$ [Gilani and Rabchuk, 2018]. Because of this, electrons are expected to scatter at the vacuum interface and the niobium interface much more often than with the impurities that gives rise to the above conductivity in the bulk case.

The effective gold layer conductivity of this study should therefore be expected to be much less than the bulk conductivity due to the increased scattering rate and it should depend on the thickness of the film. Conducting thin films

with thicknesses less than their mean free path deposited on an insulating substrate have been studied experimentally and theoretically [Gilani and Rabchuk, 2018, Lacy, 2011]. Using the semi-classical model by Lacy as a guide yields an expected conductivity for a gold layer of finite thickness with insulating interfaces on both sides. These values are indicated by the vertical lines on the left side of the plots in figure 5.12 colored according to the relevant gold layer thickness. For the niobium-gold interface this predicted conductivity should represent a lower limit since the electrons can either scatter at the gold interface, as assumed in the semi-classical model, or be transported into the niobium. If electrons do not scatter at the metal-metal interface then one can only expect this will increase the conductivity since the bulk niobium has a much higher conductivity than the thin-film gold ($\sigma_{Nb} = 1.5 \times 10^8$ S/m [Padamsee et al., 2008]). This expected conductivity range presented in figure 5.12 is approximate and could vary with gold layer properties. Further, the semi-classical model may not be accurate to describe the thinner layers considered here. Nevertheless, it should be sufficient for providing a rough guide for the expected normal layer conductivity.

The decision to include the decoupled normal conductor contribution in figure 5.12 was done both to demonstrate a simpler case and to see what conductivity of a decoupled limit would be required to explain the anomalously high surface resistance reported in the measurements at high RF field amplitude. As presented in the discussions of figure 5.4 and figure 5.5 the decoupled normal layer behavior is predicted for sufficiently strong RF fields. For the highest fields the conductivity required, for the 1.5 nm and 2.0 nm layers, exceeds the expected maximum value. As described above this upper limit is the expected bulk value and is therefore much higher than should be expected for the thin films. Even
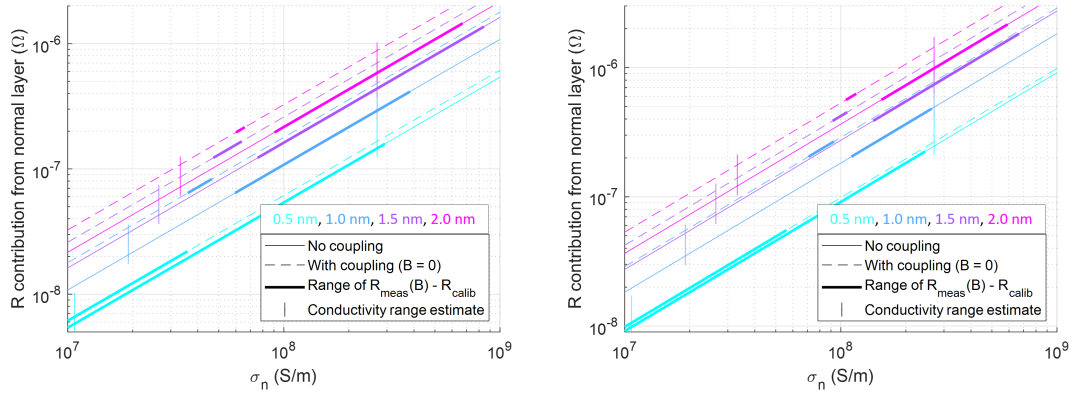
Figure 5.12: Contribution to total surface resistance from the normal conducting layer predicted from equation 5.2 and estimated from the data of figure 5.9. The normal layer conductivity in the absence of proximity-coupling effects is used as the horizontal axis. The measured data ranges are plotted on top of the model predictions at the conductivities for which the two values agree. The comparison is made at 4.0 GHz (left) and 5.2 GHz (right). The resistance from the calibration measurement is subtracted from the measured resistance to estimate the contribution from the normal conducting layer. This procedure was carried out at 1.6 K – except for the minimum value at 4.0 GHz in the 1.5 nm measurement where 2.0 K was used instead due to insufficient low-field data. Since the gold layer contribution is expected to not vary much with temperature this should be a reasonable substitution. The thick line overlapping with the decoupled normal conductor model prediction indicates the full range of this estimated contribution from data over all fields measured. The proximity-coupled (dashed line) prediction is compared only with the lowest field of the measured surface resistance contribution (including its statistical uncertainty). The vertical lines indicate the estimated minimum and maximum conductivity expected for the gold layer based on literature models and data.

if the material properties of the gold conspire to produce a higher conductivity than expected from literature it is unlikely to be high enough to account for the measured surface resistances at high RF fields. At lower fields the surface resistances could be explained by a decoupled normal layer though it would require a somewhat high conductivity, again nearing the extreme limit of the bulk conductivity.

The surface resistance prediction at the expected contact resistance (with proximity-coupling) displayed in figure 5.12 is the value expected at zero RF field. As can be seen in figure 5.4 there is no parameter range expected to increase the surface resistance as much as was observed. If the experimental situation truly corresponded to the model, then the field-dependence would be expected to be either flat or to decrease. Clearly this does not describe the field-dependence of the data, indicating that other effects may be dominating the behavior of the data as the RF field amplitude increases. Including the higher field values for the proximity-coupled case therefore would not serve much purpose in figure 5.12.

The low-field measurement, however, is highlighted as it better explains the data than the decoupled limit case. As described above, the contact resistance from section 5.4.2 is expected to put the sample in the intermediate proximity-coupling range where the surface resistance is higher than the decoupled value. This increase pushes the conductivity for which agreement is found to lower values that increase as the gold thickness increases as expected. For the thin gold films considered in this study it is intuitively expected that the conductivity should be towards this side of the limit because the film thickness is much less than the expected mean free path due to impurities. The conductivity ranges of agreement between the model with proximity-coupling and the lowest field measurement do not agree between 4.0 GHz and 5.2 GHz.

One explanation of this disagreement is the previously discussed assumption of the niobium substrate surface resistance that is subtracted from the measured gold layer total resistances. It is likely that the residual resistance in the niobium layer, especially in the 5.2 GHz measurement, was significantly larger

than the assumed value of 100 nΩ. Using higher values for the 5.2 GHz resid-
ual resistance can push the agreement range to similar values between the two
frequencies.

5.5.5   Further consideration of R(B)

At this point in the analysis, it is clear that the field-dependence of the surface
resistance measured in this study cannot be explained by the model in section
5.3.2. Figure 5.12 indicates that the low-field enhancement of surface resistance
with a lightly coupled normal layer can explain the measured data with rea-
sonable parameters. But the predicted decoupling of the normal layer with in-
creasing field, as presented in figure 5.4 and figure 5.5, is not observed. In this
subsection explanations of this discrepancy are offered and the measured field-
dependence is considered more carefully. Possibilities for the lack of agreement
between the experiment and model include the model itself, the implementation
of the model, systematic issues with the sample host cavity and its peripherals,
or issues with the sample itself.

The model agrees at low-field with other surface resistance calculations in
the appropriate limits. There are currently no good models of surface resis-
tance field-dependence so it cannot be directly checked for high-field behavior.
The model, as implemented, only includes the pair-breaking effect of nontrivial
screening currents induced from the applied RF field. It is possible that other
effects should be included such as the influence on surface resistance from the
quasiparticle populations being driven outside of equilibrium [Gurevich, 2014,
Kubo and Gurevich, 2019]. Kubo discusses how this equilibrium model does

not produce the correct frequency dependence of anomalous field effects [Martinello et al., 2018] and suggests that treating the more realistic nonequilibrium situation could correct this issue. In addition to modeling the effect of strong RF fields on the superconducting state, the method employed for calculating the surface resistance using the microscopic state information as an input is also critical to accurately describe experiments. The model in section 5.3.2 uses a method that explicitly assumes small RF fields. There are many possible issues with using such a calculation such as the induced time-dependent superconducting states being used in Fermi's golden rule [Deyo et al., 2022]. The author is not aware of any superior methods for handling the calculation of surface resistance at high RF fields. Modeling the surface resistance of a system driven by strong RF fields remains prohibitively difficult and the attempt to match the results of this study with calculations should be viewed accordingly.

Beyond the model, there are experimental considerations which should be discussed. The Cornell sample host cavity has severe limitations in terms of surface resistance resolution and reproducibility. In this study, with the exception of the 0.1 nm and 0.5 nm measurements, the surface resistances should be high enough to reliably resolve surface resistance field-dependence at low temperatures. Spurious dissipation, especially at 5.2 GHz may have varied between measurements. Comparing the calibration measurement to a baseline measurement of a niobium sample prepared identically to the calibration plate that took place directly after the gold layer study indicates that minimal changes to the surface resistance measurement and its RF field-dependence are expected at 4.0 GHz. At both frequencies the residual resistance reported increased but the increase at 5.2 GHz was large and is discussed in detail in section 5.5.4.

At 5.2 GHz, the qualitative RF field-dependence fluctuates slightly between measurements. This may indicate the influence of unknown systematic effects. The oscillations with RF field clearly visible in the 1.5 nm and 2.0 nm measurements in figure 5.9 show this effect appearing and disappearing. In both cases the resistance becomes more level around 15 mT but in some measurements the resistance drops off slightly while in others it remains constant.

This effect was first seen in the 1.0 nm measurement, which was repeated three times. The first two were done with no systematic changes and both displayed the resistance dropping with field. The third measurement was carried out after replacing the coupling antenna, its feedthrough, and the coaxial cable going to the forward power coupler (FPC) in the cryostat. In this final iteration the surface resistance leveled off with RF field but did not drop to lower values as field increased. In addition to this field-dependence change, the third iteration also reported an overall lower surface resistance value than the others. The act of remaking the coupling antenna shifted the behavior of the FPC as discussed in chapter 4.

This was not expected to account for the behavior discussed now, as the constant and dropping behaviors are seen on subsequent measurements with both forms of coupling behavior. Specifically, the third iteration of the 1.0 nm, 1.5 nm, and 2.0 nm measurements all had similar FPC behavior. This shifting field-dependence was not observed in the calibration measurement but was visible in the baseline measurement performed on a new sample plate after the gold layer study. These systematic issues are troubling, but do not disqualify the study. The finer details of the structure, especially at 5.2 GHz, should not be completely trusted. But the field-dependence effect discussed here is relatively

minor compared to the total upward trend of surface resistance with respect to field strength. There is no reason to believe that systematic issues dominated the field-dependence of the surface resistance in these measurements.

It is possible that issues with the sample itself could account for the extra dissipation with increasing field strength. The primary candidate for extra dissipation on the sample from contamination is microscopic indium flakes left on the surface after removing the indium gasket from the flange. This process involves scraping the flange with a copper edge for 30 to 60 minutes. Methanol is used throughout this procedure to loosen the indium and reduce the risk of indium flakes becoming airborne. Despite this indium flakes sometimes end up close to or on the RF surface. To the author's knowledge no visible indium flakes were left on the RF surface before adding a thicker gold layer but it is possible small amounts of residual indium stuck to the surface after a small piece was removed. The sample was high-pressure rinsed with DI water before each iteration of gold deposition in an attempt to minimize this issue. If the surface is truly a relatively uniform gold layer, then simple calculations of inner surface temperature taking into account the removal of heat from the system through the superfluid helium interface with the niobium outer surfaces [Xie, 2012] indicate that heating of the sample is not likely to account for the observed field-dependence. If there are microscopic flakes of indium present it is possible that these could act as hot spots leading to more dissipation. It is unclear if this can account for the observations.

Another consideration is dissipation due to trapped flux vortices oscillating in the applied RF field [Gurevich and Ciovati, 2013, Liarte et al., 2018, Checchin et al., 2018, Checchin and Grassellino, 2020]. These vortices are prevented from

being expelled as the sample is cooled to the superconducting state by defects pinning them in place. The cryostat used for this study is shielded by a Mu-metal cylinder which reduces the ambient magnetic field by several orders of magnitude at the location of the sample and host structure. The magnetic field is strongest in the direction normal to the sample surface. Its magnitude on the sample plate back side (3 mm from the inner surface) was measured using two flux gate magnetometers configured to measure the magnetic field normal to the sample plate positioned at about half the radius of the RF surface.

For the gold layer study, the ambient magnetic field varied between a minimum of 5 mG and a maximum of 15 mG. This variation does not indicate any systematic trends as the lower thicknesses with smaller surface resistances sometimes had the largest ambient fields. The qualitative behavior of the 4.0 GHz and 5.2 GHz data was consistent between samples despite the sample being thermally cycled back to room temperature and back to cryogenic temperature between each frequency study. The one exception is the shift from 1.5 nm to 2.0 nm thickness where the 4.0 GHz measurement has a much smaller difference than the 5.2 GHz. This difference cannot be accounted for by ambient magnetic fields observed by the two flux gates.

Regarding field-dependence it is critical to compare the ambient fields of the gold layer study to that of the calibration and baseline measurements. No major differences were observed. If trapped flux dissipation is expected to account for the differences it would therefore be required that the substitution of the gold layer for the native oxide greatly increases the density of trapped flux vortices. It is not clear what role flux dissipation would have in the proximity-coupled normal layer or if the gold layer and its thickness would trap more flux vortices

than the native oxide.

In addition to the ambient magnetic field present on the sample during its transition into the superconducting state it is known that thermal currents induced by the Seebeck effect in metallic bilayers can lead to significant magnetic fields and trapped flux in superconducting RF cavities [Hall, 2017]. Primarily this has been observed in cavities where $2\,\mu m - 3\,\mu m$ of Nb_3Sn is grown onto a niobium substrate. This effect can be minimized by slowly cooling the cryostat preventing temperature gradients along the cavity. This is a trade-off for niobium cavities where it is thought that cooling quickly, to produce large thermal gradients, more effectively expels magnetic vortices during the transition to the superconducting state [Kubo, 2016].

Adapting the approximate analysis for thermal currents in a Nb_3Sn cavity [Hall, 2017] to the geometry of the sample host cavity with a thin gold film, it is found that for a given thermal gradient across the sample the magnetic fields generated from thermal currents will be many orders of magnitude less than the situation of Nb_3Sn cavities due to the extremely thin gold layers involved. For this analysis it was assumed that the primary thermal gradient was oriented radially outward on the sample. The helium is transferred into the cryostat from the bottom and it is expected that the primary cooling happens by conduction through the metallic pieces at the bottom (the host structure) which are cooled first. The cooling therefore would flow through the host structure and then into the sample plate. While it is expected from this analysis that the thermally generated magnetic field at the sample would scale directly with gold layer thickness it would be very small compared to the ambient field for any reasonable thermal gradient magnitude. This analysis may not be entirely valid but has

demonstrated reasonable agreement with expectations for Nb_3Sn cavities. All helium transfers for this study were performed as quickly as possible to maximize thermal gradients. While this simple analysis indicates this may not have been an issue, it would have been ideal to repeat a measurement with a slower cool down to compare. This would have required a second calibration with a similar cool down but would have more conclusively dismiss concerns about this source of trapped flux.

The above is speculative and hopefully provides an honest account of the theoretical and experimental situation relevant to this study for readers to consider. For a final consideration of the field-dependence the results of figure 5.9 are normalized for directly comparing the field-dependence as gold layer thickness changes. The resulting normalization at 1.6 K is shown in figure 5.13 where it is clear that the relative field-dependence of the gold layer samples is almost independent of thickness. For 4.0 GHz the calibration is clearly different than all of the displayed gold layer samples. At 5.2 GHz the calibration arguably is similar to the normalized gold layer field-dependence but as will be argued later in the text a more careful analysis indicates different behavior. At 2.0 K this difference is more pronounced.

The normalized gold layer surface resistances in figure 5.13 appear to roughly follow a square root dependence on field amplitude. The lines in this figure demonstrate a fit of a power law $R(B) = AB^a + C$ to the normalized data requiring $C > 0$ and $a = 0.5$. At 4.0 GHz it is clear this fit applies fairly well for the gold layer across the entire field range and is not as effective for the calibration. At 5.2 GHz this is less clear. The same fit has been carried out for a a ranging from 0 to 1. The residual sum of squares (RSS) resulting from this procedure

191
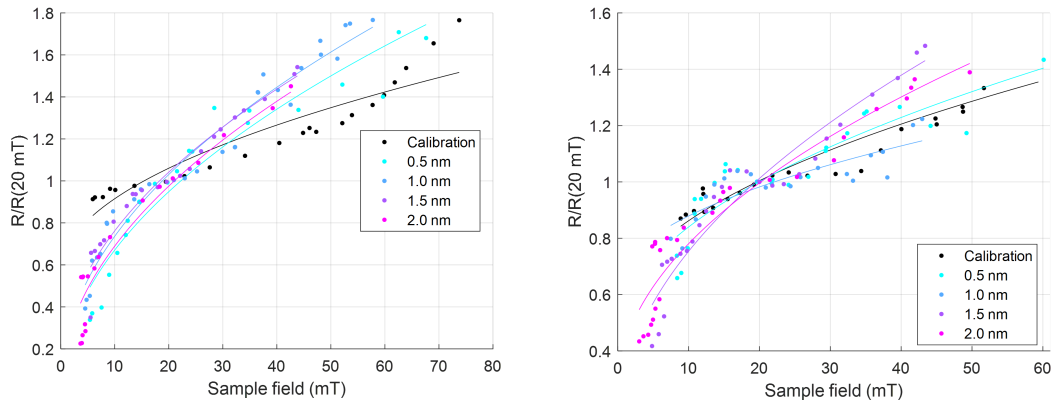
Figure 5.13: Extracted sample surface resistance from figure 5.9 at 1.6 K and 4.0 GHz (left) and 5.2 GHz (right) normalized by its value at 20 mT. The lines result from fitting a power law $R(B) = AB^a + C$ to the normalized data requiring $C > 0$ and $a = 0.5$. The calibration sample is included as a reference to compare the effect of replacing native niobium oxide with a given thickness of gold.

is shown in figure 5.14. It is clear that the square root dependence is valid at 4.0 GHz for all gold layers. At 5.2 GHz this does not appear to be the case but a clear difference between the calibration and the samples with a gold layer can be seen. It has been suggested that this rough square root dependence could be indicative of a single row of vortices entering the surface as the RF field is increased moving past pinned vortices [Gurevich, 2022].
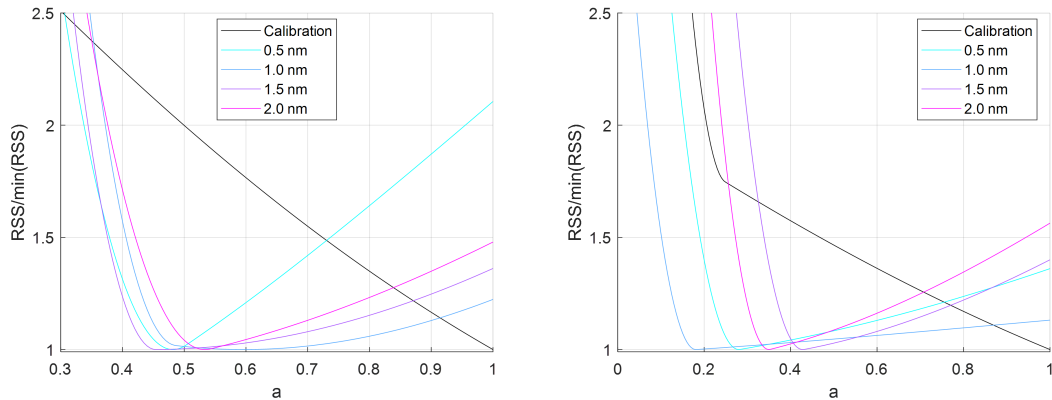
Figure 5.14: Normalized residual sum of squares (RSS) resulting from fitting the power law $R(B) = AB^a + C$ to the normalized data with $C > 0$ to the data of figure 5.13 at 4.0 GHz (left) and 5.2 GHz (right).

5.6   Conclusion

The gold layer study discussed in this chapter was inspired by experiments and theories discussing the possible relevance of normal conducting phases present in niobium oxide to SRF metrics. The niobium oxide properties are complex and difficult to accurately characterize from a material studies perspective. Experimental attempts to modify the properties of the native oxide have employed furnace treatments which could have secondary effects on the niobium surface that obscure the dependence of measured surface resistance on its oxide properties. These experiments indicate substantial changes to surface resistance can be induced by these treatments so it is reasonable to suggest that the changes to the oxide are at least a possible source of the observed shifts. In this study the aim was to isolate the role of a normal conducting film present on a bulk superconductor to help guide considerations on the importance of niobium oxide in SRF cavities.

Primarily this work was inspired by the models of Gurevich and Kubo studying the influence of a normal conducting layer over a bulk superconductor. Their model predicts parameter ranges where there exist technologically useful improvements to the surface resistance and its dependence on field. It also makes predictions indicating that if the native niobium oxide is replaced with a thin normal conductor with appropriate electrical contact resistance between the two metals, then one could expect surface resistances greatly exceeding the value of a bare niobium surface that display anomalous field-dependence. This scenario is well-suited for the Cornell sample host cavity which, theoretically, should allow for detailed study of superconducting RF response for samples with surface resistance exceeding that of niobium. The goal was to realize and

study a sample in this parameter range to probe for qualitative agreement between these dramatic model predictions and an experiment with a simplified surface compared to the niobium oxide.

Gold was selected for the normal conducting film since it adheres well to niobium and does not oxidize, allowing for adding more gold between RF measurements to study how the surface resistance changes with film thickness. An attempt to eliminate or at least minimize the niobium oxide present before depositing the gold was made by soaking the niobium in dilute Hydrofluoric acid in an oxygen free environment and attempting to minimize any exposure to oxygen before thermally evaporating gold onto the bare surface. This procedure was found to reduce contact resistance compared to a control with native oxide. The resulting contact resistance was expected to produce the desired intermediate coupling for the target sample parameters.

Reasonable agreement is found between the model predictions at low-field and experimental surface resistance measurements. This indicates that the broader aspects of the data can be trusted despite experimental issues such as shifts in the behavior of the sample host cavity or mild contamination of the sample. The field-dependence prediction of the model is completely unable to even qualitatively reproduce the increase in surface resistance with RF field amplitude that was observed in the study. At this time there is no solid explanation for the discrepancy but some suggestions were made based on model limitations, possible sample contamination, and unaccounted effects such as magnetic flux vortices. Interesting observations can be made about the data despite its lack of explanation. Specifically, the rough field-dependence of the sample appears to be independent of gold layer thickness. This surface resis-

tance appears to scale with the square root of RF field amplitude.

The most exciting result of the study came from the first iteration with the thinnest gold layer (approximately 0.1 nm thick). This extremely thin gold layer is expected to effectively passivate the niobium surface and prevent oxidation. Assuming the thickness reported here is accurate and the growth procedure was successful in preventing surface oxidation then this sample would have successfully replaced niobium oxide with a normal conducting film thinner than the metallic portion of the niobium oxide typically present. The results of this measurement indicate that the surface resistance with this thin gold layer is less than or near to that with the niobium oxide. The increase of resistance with RF field is found to be less pronounced. Most critically the quench field measured greatly exceeded that of the same sample before the native oxide was replaced. Reviewing the experimental metrics of this study there is no clear reason to expect this result is a systematic aberration. The claim motivated by this finding is that eliminating or reducing the thickness of the metallic portion of the native oxide could enhance quench fields of niobium cavities. This study has not been reproduced and doing so is essential for validating this important claim.

This study was exploratory in nature. Guided by this work, improvements to the study could be carried out in the future. The sample host cavity's RF pathways could be modified to reduce some of the sources of systematic shifts in measurement and operational behaviors, more care could be taken with the sample surface between gold depositions, studying different cooling rates, and the successful acquisition of baseline data would be the author's immediate recommendations. The deposition of gold using thermal evaporation was done for simplicity but other deposition methods should be considered, especially those,

such as electroplating, that prioritize the elimination of oxygen from the sample surface, which was a complication that has largely been ignored in the discussion of this sample. From a technological standpoint the main direction that should be explored as a result of this work is further consideration of eliminating the metallic portion of the native oxide. This could be done by an insulating or normal conducting passivation layer.

From this study it is clear that thin normal conducting films present on a superconducting surface can greatly obscure the response of the bulk. Any experiments, past and future, that report on the surface resistance of a superconductor should also consider the nature of its oxide. Decades of optimizing the treatments used on niobium may have inadvertently tailored the resulting surface oxide, among other features, to optimize the desired metrics. For less studied materials that report unexpectedly poor performance, which is very common, it should be asked if the nature of the surface oxide could be relevant. For example, there is no literature considering whether Nb_3Sn, which has low surface resistance but anomalously low quench fields, could be improved by more carefully controlling its oxide. Though there is compelling evidence that this material is primarily limited by Josephson vortex entry at grain boundaries, this could provide an alternative method for attempting to improve the quench field.

CHAPTER 6

CONCLUSION

In this work an attempt was made to advance the understanding of the high-amplitude microwave-superconductor interaction. The study aimed to provide relevant data for application and to probe interesting physics, while using samples that can be reliably measured with available equipment. The attempt was successful. Novel and relevant data was produced that can be used for guiding understanding and research directions.

6.1   Advancing the sample host cavity

The measurement system available for this work, the Cornell sample host cavity described in chapter 4, is not ideal for measurements intended for studying materials that are as good as or better than those currently used for accelerator applications. Its measurement scheme relies on the system having minimal noise and virtually zero systematic error. In this work, two questions about the sample host cavity were explored. The first question was how to quantify the systematic issues to determine its limits of operation for a given application. The second was how much could limiting aspects of the system be suppressed.

The Cornell sample host cavity uses a calibration procedure to decouple the response of the sample from that of the system as a whole. This procedure was derived including general sources of systematic error. Quantitative statements can be made by categorizing each contribution based on where it enters the calculation and expressing each contribution source in terms of its fraction of the total system response. Using this systematic uncertainty calculation, it is

possible to determine the tolerable contributions to the system response from a variety of unwanted but relevant sources. This information can be used to guide the development of similar systems in the future.

The (fractional) statistical uncertainty of the extracted sample surface resistance will increase as the true sample surface resistance decreases. The error is especially pronounced when the sample surface resistance becomes less than that of the host structure. An expression giving the expected uncertainty in the extracted surface resistance for a given fractional measurement error was obtained. This equation can be used as a guide for those considering constructing a similar sample host cavities to determine if it is suitable for their goals. For existing systems with known measurement uncertainties, it can be used to consider what samples can be studied with an acceptable level of error.

Significant systematic changes were implemented in an attempt to minimize the sources of statistical and systematic uncertainty, as well as addressing difficulties and limitations in the cavity and its peripheral systems.

First, it was found that the sample preparation procedure introduced contamination that led to sporadic results, produced systematic error, and obscured the behaviors of any samples that were studied. A more careful preparation procedure was developed. At 4.0 GHz, samples have routinely displayed high quality and low variation for the samples with identical preparation. At 5.2 GHz, the situation is improved, but there appears to still be a fair amount of variation. The source of this variation is not known

Second, a transmitted power probe was added to the cavity. This involved drilling a hole in the existing structure and electron beam welding a port. The

geometry of this addition and its implementation were both carefully designed and conducted, as any issues could have resulted in an unusable system. A transmitted power coupler was designed to achieve target parameters for both modes of operation. This addition appears to have been a complete success and has dramatically improved the power handling and system usability. At 4.0 GHz, no detrimental effects have been observed from the addition. There is no 5.2 GHz data to compare to from before the addition, but the port is not expected to be a limiting factor in this mode either.

Third, the forward power coupler (FPC) was redesigned. While the issues this change was designed to address appear to be resolved, new problems related to the FPC have been created. Overall, the system is better as a result of the changes made to the FPC. But if the Cornell sample host cavity is used in the future, another iteration to improve the FPC would be recommended.

These changes have produced a more reliable measurement system that is easier to operate and can explore a larger parameter space than the previous iteration. It is limited in utility, but if users are aware of the limitations documented in this text, it can be used for certain applications where the uncertainty is tolerable.

An unintended but equally interesting situation that was also explored in this work was the study of a niobium surface in the presence of strong 4.0 GHz and 5.2 GHz fields, where limited data is available. The 4.0 GHz results are similar to those published elsewhere, and display the apparent "anti-Q-slope" that is not seen at lower frequencies with similar surface preparation. Notably, this is the first demonstration of this phenomena in niobium using a TE_{011} mode excitation. Observing the anti-Q-slope in this mode indicates that surface electric

fields are likely not relevant for its occurrence.

In its current form, the sample host cavity can be used for rough investigations of superconducting samples. Repeating measurements across several samples may be a good step to include when planning a study, as this could mitigate concerns about or expose the presence of systematic variations between measurements. Further use should follow a redesign of the FPC in an attempt to eliminate the new issues that appear related to the version introduced in this work.

6.2   Proximity-coupling in a strong microwave field

Recognizing the limitations of the sample host cavity, it was necessary to carefully select what sample studies to pursue. The decision was made to study the high-amplitude microwave interaction with thin gold films grown over a niobium substrate because it was expected to be appropriate for the sample host cavity, had a connection to accelerator application, and existing models indicated it could display interesting behaviors for certain parameter ranges. Following existing work, a model was implemented to guide the target parameters of material growth. From this guidance, a procedure was created to strip the niobium oxide and deposit thin gold layers. RF measurements were carried out before adding additional gold to the film to study how the behavior changed with thickness.

Low-amplitude field measurements were reasonably well-explained by the model. As the field strength increased, this agreement vanished. The qualitative behavior of the measurements does not match the model prediction of

field-dependence for any parameters explored. Explanations for the discrepancy were considered, but no conclusions could be drawn. The measured field-dependence of the proximity-coupled samples was observed to be essentially independent of gold layer thickness and proportional to the square root of the field strength. Most strikingly, comparing the quench field of the sample with its native oxide (prior to gold deposition) to the thinnest gold layer studied, it was observed to have increased substantially. This increase was observed at both frequencies studied. The surface resistance of this particular gold layer sample was too low to be resolved adequately by the sample host cavity. While not quantitative, it can be said that this indicates the introduction of the gold layer (at this thickness) had either no or limited detrimental effects on surface resistance.

This study was a first attempt and the results have not been reproduced. The results should be viewed in the spirit of attempting to guide future studies and considerations, but should not be taken as established. From this standpoint, the indication of this study is that the niobium oxide, present in all accelerator cavities, is worth further consideration. Specifically, it should be studied further to determine if reducing or eliminating the niobium oxide can improve cavity quench fields. While the results of this study specifically deal with niobium, they indicate that the native oxide of a general superconductor should be carefully considered. This consideration ranges from attempting to improve existing Nb_3Sn cavities, to judging novel materials displaying unexpectedly poor performances. The author is unaware of the native oxide being broadly discussed in literature in this context. It is hoped that the results of this study motivate others to delve more into this topic.

In this study, the choice to use a gold layer as the normal conductor was somewhat arbitrary. Its selection was based on knowledge that it adheres well to niobium and that it does not oxidize. The latter property allowed for incrementally adding to the gold thickness of a single sample between RF measurements. This would be more cost effective compared to creating different samples for each thickness studied, and would ideally limit the variation of critical parameters like the contact resistance between the substrate and the film. Explicitly, the aim was to better understand what role a normal conductor has in the microwave interaction when proximity-coupled to a bulk superconductor. The gold accomplished this, but may also be well-suited for further use.

From the application perspective, is there any reason to use a normal conducting capping layer to prevent oxidation instead of an insulating layer? From the models discussed in chapter 5, there may be some benefit to using a thin layer with specific properties. From a practical stance, the difficulty of controlling the native oxide is not the capping layer itself, but removing the oxide. The oxide, specifically the metallic portion, cannot realistically be removed by heat treatments. Chemical treatments are required. The oxidation is thought to occur quickly and with little oxygen present [Sun et al., 2022]. Therefore, any capping layer must be deposited on a chemically treated substrate with minimal exposure to oxygen. From the experience gained in this study, it is clear that gold is a rather simple method to accomplish this.

In this study, the procedure was to remove the oxide layer using a chemical treatment in a glovebox with a nitrogen atmosphere, seal it in a plastic bag in the glovebox, and then transport it to a thermal evaporation chamber with an active nitrogen purge. This procedure was not ideal, and may have allowed for some

oxidation. If it was sufficient, however, the same method could perhaps be used for deposition equipment capable of depositing an insulating layer. The ideal path would be to remove the oxide and deposit the capping layer inside of the glovebox. For a conducting capping layer, this could readily be accomplished by electroplating, which is naturally performed in a glovebox. Insulating capping layers would require a more sophisticated method of transferring a sample to a deposition system capable of growing an insulating capping layer while completely preventing sample oxidation. If such a system exists and is readily available, it would be an interesting study to compare to the normal conducting capping layers studied in this work.

BIBLIOGRAPHY

A. Abrikosov, L. Gor′kov, and I. Khalatnikov. A Superconductor in a High Frequency Field. *JETP*, 8:182, Jan 1959.

P. Anderson. Theory of dirty superconductors. *Journal of Physics and Chemistry of Solids*, 11(1):26–30, 1959. ISSN 0022-3697. doi: https://doi.org/10. 1016/0022-3697(59)90036-8. URL https://www.sciencedirect.com/ science/article/pii/0022369759900368.

A. Andreev. The thermal conductivity of the intermediate state in superconductors. *JETP*, 46(5):1823, 1964.

S. M. Anlage. The physics and applications of superconducting metamaterials. *Journal of Optics*, 13(2):024001, Nov 2010. doi: 10.1088/2040-8978/13/2/ 024001. URL https://doi.org/10.1088/2040-8978/13/2/024001.

S. M. Anlage. Microwave Superconductivity. *IEEE Journal of Microwaves*, 1(1): 389–402, 2021. doi: 10.1109/JMW.2020.3033156.

N. Ashcroft and N. Mermin. *Solid State Physics*. Cengage., 2021. ISBN 9780357670811. URL https://books.google.com/books?id= CcSazQEACAAJ.

D. Bafia, A. Grassellino, M. Checchin, J. F. Zasadzinski, and A. Romanenko. The Anomalous Resonant Frequency Variation of Microwave Superconducting Niobium Cavities Near T_c, 2021. URL https://arxiv.org/abs/2103. 10601.

J. Bardeen, L. N. Cooper, and J. R. Schrieffer. Theory of Superconductivity. *Phys. Rev.*, 108:1175–1204, Dec 1957. doi: 10.1103/PhysRev.108.1175. URL https: //link.aps.org/doi/10.1103/PhysRev.108.1175.

J. Bardeen, R. Kümmel, A. E. Jacobs, and L. Tewordt. Structure of Vortex Lines in Pure Superconductors. *Phys. Rev.*, 187:556–569, Nov 1969. doi: 10.1103/PhysRev.187.556. URL https://link.aps.org/doi/10.1103/PhysRev.187.556.

W. Belzig, C. Bruder, and A. L. Fauchère. Diamagnetic response of a normal-metal–superconductor proximity system at arbitrary impurity concentration. *Phys. Rev. B*, 58:14531–14540, Dec 1998. doi: 10.1103/PhysRevB.58.14531. URL https://link.aps.org/doi/10.1103/PhysRevB.58.14531.

W. Belzig, F. K. Wilhelm, C. Bruder, G. Schön, and A. D. Zaikin. Quasiclassical Green's function approach to mesoscopic superconductivity. *Superlattices and Microstructures*, 25(5):1251–1288, 1999. ISSN 0749-6036. doi: https://doi.org/10.1006/spmi.1999.0710. URL https://www.sciencedirect.com/science/article/pii/S0749603699907103.

J. Carlson, A. Pack, M. K. Transtrum, J. Lee, D. N. Seidman, D. B. Liarte, N. S. Sitaraman, A. Senanian, M. M. Kelley, J. P. Sethna, T. Arias, and S. Posen. Analysis of magnetic vortex dissipation in Sn-segregated boundaries in Nb$_3$Sn superconducting RF cavities. *Phys. Rev. B*, 103:024516, Jan 2021. doi: 10.1103/PhysRevB.103.024516. URL https://link.aps.org/doi/10.1103/PhysRevB.103.024516.

J.-J. Chang and D. J. Scalapino. Nonequilibrium superconductivity. *Journal of Low Temperature Physics*, 31(1):1–32, Apr 1978. ISSN 1573-7357. doi: 10.1007/BF00116228. URL https://doi.org/10.1007/BF00116228.

M. Checchin and A. Grassellino. Vortex Dynamics and Dissipation under High-Amplitude Microwave Drive. *arXiv: Superconductivity*, 2020.

M. Checchin, M. Martinello, A. Grassellino, S. Aderhold, S. K. Chandrasekaran, O. S. Melnychuk, S. Posen, A. Romanenko, and D. A. Sergatskov. Frequency dependence of trapped flux sensitivity in SRF cavities. *Applied Physics Letters*, 112(7):072601, 2018. doi: 10.1063/1.5016525. URL https://doi.org/10.1063/1.5016525.

B. Chiaro, A. Megrant, A. Dunsworth, Z. Chen, R. Barends, B. Campbell, Y. Chen, A. Fowler, I. C. Hoi, E. Jeffrey, J. Kelly, J. Mutus, C. Neill, P. J. J. O'Malley, C. Quintana, P. Roushan, D. Sank, A. Vainsencher, J. Wenner, T. C. White, and J. M. Martinis. Dielectric surface loss in superconducting resonators with flux-trapping holes. *Superconductor Science and Technology*, 29(10):104006, Aug 2016. doi: 10.1088/0953-2048/29/10/104006. URL https://doi.org/10.1088/0953-2048/29/10/104006.

G. Ciovati. Effect of low-temperature baking on the radio-frequency properties of niobium superconducting cavities for particle accelerators. *Journal of Applied Physics*, 96(3):1591–1600, 2004. doi: 10.1063/1.1767295. URL https://doi.org/10.1063/1.1767295.

P. de Gennes and P. Pincus. *Superconductivity of Metals and Alloys*. Advanced book classics. W.A. Benjamin, 1966. URL https://books.google.com/books?id=M8A8AAAAIAAJ.

S. Deyo, M. Kelley, N. Sitaraman, T. Oseroff, D. B. Liarte, T. Arias, M. Liepe, and J. P. Sethna. Dissipation by surface states in superconducting radio-frequency cavities. *Phys. Rev. B*, 106:104502, Sep 2022. doi: 10.1103/PhysRevB.106.104502. URL https://link.aps.org/doi/10.1103/PhysRevB.106.104502.

P. Dhakal. Nitrogen doping and infusion in SRF cavities: A review. *Physics Open*,

5:100034, 2020. ISSN 2666-0326. doi: https://doi.org/10.1016/j.physo.2020.100034. URL https://www.sciencedirect.com/science/article/pii/S2666032620300211.

R. C. Dynes, V. Narayanamurti, and J. P. Garno. Direct Measurement of Quasiparticle-Lifetime Broadening in a Strong-Coupled Superconductor. *Phys. Rev. Lett.*, 41:1509–1512, Nov 1978. doi: 10.1103/PhysRevLett.41.1509. URL https://link.aps.org/doi/10.1103/PhysRevLett.41.1509.

R. C. Dynes, J. P. Garno, G. B. Hertel, and T. P. Orlando. Tunneling Study of Superconductivity near the Metal-Insulator Transition. *Phys. Rev. Lett.*, 53: 2437–2440, Dec 1984. doi: 10.1103/PhysRevLett.53.2437. URL https://link.aps.org/doi/10.1103/PhysRevLett.53.2437.

G. Eilenberger. Transformation of Gorkov's equation for type II superconductors into transport-like equations. *Zeitschrift für Physik A Hadrons and nuclei*, 214(2):195–213, Apr 1968. ISSN 0939-7922. doi: 10.1007/BF01379803. URL https://doi.org/10.1007/BF01379803.

G. Eremeev. *Study of the High Field Q-slope Using Thermometry*. PhD thesis, Cornell University, 2008.

T. Gilani and D. Rabchuk. Electrical resistivity of gold thin film as a function of film thickness. *Canadian Journal of Physics*, 96(3):272–274, 2018. doi: 10.1139/cjp-2017-0484. URL https://doi.org/10.1139/cjp-2017-0484.

D. Gonnella. *The Fundamental Science of Nitrogen-Doping of Niobium Superconducting Cavities*. PhD thesis, Cornell University, 2016.

L. P. Gor'kov. Energy spectrum of superconductors. [Quantum field theory].

Sov. Phys. - JETP (Engl. Transl.); (United States), 7(3), 1 1958. URL https://www.osti.gov/biblio/7264948.

P. Goudket, T. Junginger, and B. P. Xiao. Devices for SRF material characterization. *Superconductor Science and Technology*, 30(1):013001, Nov 2016. doi: 10.1088/0953-2048/30/1/013001. URL https://doi.org/10.1088/0953-2048/30/1/013001.

A. Grassellino, A. Romanenko, D. Sergatskov, O. Melnychuk, Y. Trenikhina, A. Crawford, A. Rowe, M. Wong, T. Khabiboulline, and F. Barkov. Nitrogen and argon doping of niobium for superconducting radio frequency cavities: a pathway to highly efficient accelerating structures. *Superconductor Science and Technology*, 26(10):102001, Aug 2013. doi: 10.1088/0953-2048/26/10/102001. URL https://doi.org/10.1088/0953-2048/26/10/102001.

A. Grassellino, A. Romanenko, D. Bice, O. Melnychuk, A. Crawford, S. Chandrasekaran, Z. Sung, D. Sergatskov, M. Checchin, S. Posen, M. Martinello, and G. Wu. Accelerating fields up to 49 MV/m in TESLA-shape superconducting niobium cavities via 75C vacuum bake. *arXiv: Accelerator Physics*, 2018.

J. Guo, S. Tantawi, D. Martin, and C. Yoneda. A cryogenic RF material testing facility at SLAC. In *2010 International particle accelerator conference*, Kyoto, Japan, 2013.

A. Gurevich. Reduction of Dissipative Nonlinear Conductivity of Superconductors by Static and Microwave Magnetic Fields. *Phys. Rev. Lett.*, 113: 087001, Aug 2014. doi: 10.1103/PhysRevLett.113.087001. URL https://link.aps.org/doi/10.1103/PhysRevLett.113.087001.

A. Gurevich. Private communication, 2022.

A. Gurevich and G. Ciovati. Effect of vortex hotspots on the radio-frequency surface resistance of superconductors. *Phys. Rev. B*, 87:054502, Feb 2013. doi: 10.1103/PhysRevB.87.054502. URL https://link.aps.org/doi/10.1103/PhysRevB.87.054502.

A. Gurevich and T. Kubo. Surface impedance and optimum surface resistance of a superconductor with an imperfect surface. *Phys. Rev. B*, 96:184515, Nov 2017. doi: 10.1103/PhysRevB.96.184515. URL https://link.aps.org/doi/10.1103/PhysRevB.96.184515.

J. Halbritter. FORTRAN-program for the computation of the surface impedance of superconductors, Jun 1970. URL https://publikationen.bibliothek.kit.edu/270004230.

J. Halbritter. On the oxidation and on the superconductivity of niobium. *Applied Physics A*, 43(1):1–28, May 1987. ISSN 1432-0630. doi: 10.1007/BF00615201. URL https://doi.org/10.1007/BF00615201.

J. Halbritter. Granular superconductors and their intrinsic and extrinsic surface impedance. *Journal of Superconductivity*, 8(1):691–703, Dec 1995. doi: 10.1007/BF00727492. URL https://doi-org/10.1007/BF00727492.

D. Hall. *New Insights Into the Limitations on the Efficiency and Achievable Gradients in Nb$_3$Sn SRF Cavities*. PhD thesis, Cornell University, 2017.

D. L. Hall, M. Liepe, I. Madjarov, K. McDermott, and N. Valles. Development and Performance of a High Field TE-mode Sample Host Cavity. In *16th International Conference on Superconductivity*, Paris, France, 2013.

D. L. Hall, C. Burton, and M. Liepe. Sample Plate Studies Using a High Field

TE Cavity with thermometry Mapping System. In *27th International Linear Accelerator Conference*, Geneva, Switzerland, 2014a.

D. L. Hall, M. Liepe, D. Gonnella, and I. Madjarov. SRF Material Performance Studies Using a Sample Host cavity. In *5th International Particle Accelerator Conference*, Dresden, Germany, 2014b.

M. Hein. *High-Temperature-Superconductor Thin Films at Microwave Frequencies*. Springer Tracts in Modern Physics. Springer Berlin Heidelberg, 1999. ISBN 9783540656463. URL https://books.google.com/books?id=5MIDpYI1z20C.

M. A. Hein, R. J. Ormeno, and C. E. Gough. High-frequency electrodynamic response of strongly anisotropic clean normal and superconducting metals. *Phys. Rev. B*, 64:024529, Jun 2001. doi: 10.1103/PhysRevB.64.024529. URL https://link.aps.org/doi/10.1103/PhysRevB.64.024529.

J. Jackson. *Classical Electrodynamics*. Wiley, 2012. ISBN 9788126510948. URL https://books.google.com/books?id=8qHCZjJHRUgC.

T. Junginger. *Investigations of the surface resistance of super-conducting materials*. PhD thesis, University of Heidelberg, 2012.

S. Keckert. *Characterization of Nb_3Sn and multilayer thin films for SRF applications*. PhD thesis, University of Siegen, 2019.

S. Keckert, O. Kugeler, and J. Knobloch. Surface Resistance Characterization of Nb_3Sn Using the HZB Quadrupole Resonator. In *18th International Conference on RF Superconductivity*, Lanzhou, China, 2017.

S. Keckert, R. Kleindienst, O. Kugeler, D. Tikhonov, and J. Knobloch. Characterizing materials for superconducting radiofrequency applications—A com-

prehensive overview of the quadrupole resonator design and measurement capabilities. *Review of Scientific Instruments*, 92(6):064710, 2021. doi: 10.1063/5.0046971. URL https://doi.org/10.1063/5.0046971.

M. M. Kelley, N. S. Sitaraman, and T. A. Arias. Ab initio theory of the impact of grain boundaries and substitutional defects on superconducting Nb$_3$Sn. *Superconductor Science and Technology*, 34(1):015015, Dec 2020. doi: 10.1088/1361-6668/abc8ce. URL https://doi.org/10.1088/1361-6668/abc8ce.

C. Kittel. *Quantum Theory of Solids*. Wiley, 1963. ISBN 9780471825630. URL https://books.google.com/books?id=lAlRAAAAMAAJ.

R. Kleindienst. *Radio Frequency Characterization of Superconductors for Particle Accelerators*. PhD thesis, University of Siegen, 2017.

J. Knobloch. *Advanced Thermometry Studies of Superconducting RF Cavities*. PhD thesis, Cornell University, 1997.

N. Kopnin. *Theory of Nonequilibrium Superconductivity*. International Series of Monographs on Physics. Clarendon Press, 2001. ISBN 9780198507888. URL https://books.google.com/books?id=fYZb3D1V8rwC.

T. Kubo. Flux trapping in superconducting accelerating cavities during cooling down with a spatial temperature gradient. *Progress of Theoretical and Experimental Physics*, 2016, 01 2016. doi: 10.1093/ptep/ptw049.

T. Kubo and A. Gurevich. Field-dependent nonlinear surface resistance and its optimization by surface nanostructuring in superconductors. *Phys. Rev. B*, 100:064522, Aug 2019. doi: 10.1103/PhysRevB.100.064522. URL https://link.aps.org/doi/10.1103/PhysRevB.100.064522.

M. Y. Kuprianov and V. Lukichev. Influence of boundary transparency on the critical current of dirty SS'S structures. *Zh. Eksp. Teor. Fiz*, 94:149, 1988.

F. Lacy. Developing a theoretical relationship between electrical resistivity, temperature, and film thickness for conductors. *Nanoscale Research Letters*, 6(1):636, Dec 2011. ISSN 1556-276X. doi: 10.1186/1556-276X-6-636. URL https://doi.org/10.1186/1556-276X-6-636.

P. Lee. Theory of Soliids II. Lecture 10: Superconductors With Disorder, Spring 2009. URL https://ocw.mit.edu/courses/8-512-theory-of-solids-ii-spring-2009/.

A. J. Leggett. Theory of a Superfluid Fermi Liquid. I. General Formalism and Static Properties. *Phys. Rev.*, 140:A1869–A1888, Dec 1965. doi: 10.1103/PhysRev.140.A1869. URL https://link.aps.org/doi/10.1103/PhysRev.140.A1869.

C. J. Lehner, D. E. Oates, Y. M. Habib, G. Dresselhaus, and M. S. Dresselhaus. Modeling the microwave impedance of high-tc long josephson junctions. *Journal of Superconductivity*, 12(2):363–376, Apr 1999. ISSN 1572-9605. doi: 10.1023/A:1007705400222. URL https://doi.org/10.1023/A:1007705400222.

D. B. Liarte, D. Hall, P. N. Koufalis, A. Miyazaki, A. Senanian, M. Liepe, and J. P. Sethna. Vortex Dynamics and Losses Due to Pinning: Dissipation from Trapped Magnetic Flux in Resonant Superconducting Radio-Frequency Cavities. *Phys. Rev. Applied*, 10:054057, Nov 2018. doi: 10.1103/PhysRevApplied.10.054057. URL https://link.aps.org/doi/10.1103/PhysRevApplied.10.054057.

M. Liepe. *Superconducting Multicell Cavities for Linear Colliders*. PhD thesis, University of Hamburg, 2001.

D. Linden, T. Orlando, and W. Lyons. Modified two-fluid model for superconductor surface impedance calculation. *IEEE Transactions on Applied Superconductivity*, 4(3):136–142, 1994. doi: 10.1109/77.317828.

F. London, H. London, and F. A. Lindemann. The electromagnetic equations of the supraconductor. *Proceedings of the Royal Society of London. Series A - Mathematical and Physical Sciences*, 149(866):71–88, 1935. doi: 10.1098/rspa. 1935.0048. URL https://royalsocietypublishing.org/doi/abs/ 10.1098/rspa.1935.0048.

P. Mangin and R. Kahn. *Superconductivity: An introduction*. Springer International Publishing, 2016. ISBN 9783319505275. URL https://books. google.com/books?id=ogDGDQAAQBAJ.

M. Martinello, M. Checchin, A. Romanenko, A. Grassellino, S. Aderhold, S. K. Chandrasekeran, O. Melnychuk, S. Posen, and D. A. Sergatskov. Field-Enhanced Superconductivity in High-Frequency Niobium Accelerating Cavities. *Phys. Rev. Lett.*, 121:224801, Nov 2018. doi: 10.1103/PhysRevLett.121. 224801. URL https://link.aps.org/doi/10.1103/PhysRevLett. 121.224801.

D. C. Mattis and J. Bardeen. Theory of the Anomalous Skin Effect in Normal and Superconducting Metals. *Phys. Rev.*, 111:412–417, Jul 1958. doi: 10.1103/PhysRev.111.412. URL https://link.aps.org/doi/10.1103/ PhysRev.111.412.

A. A. McMillan, J. D. Graham, S. A. Willson, R. G. Farber, C. J. Thompson, and

S. J. Sibener. Persistence of the Nb(100) surface oxide reconstruction at elevated temperatures. *Superconductor Science and Technology*, 33(10):105012, Sep 2020. doi: 10.1088/1361-6668/abaec0. URL https://doi.org/10.1088/1361-6668/abaec0.

S. B. Nam. Theory of Electromagnetic Properties of Superconducting and Normal Systems. I. *Phys. Rev.*, 156:470–486, Apr 1967a. doi: 10.1103/PhysRev.156.470. URL https://link.aps.org/doi/10.1103/PhysRev.156.470.

S. B. Nam. Theory of Electromagnetic Properties of Strong-Coupling and Impure Superconductors. II. *Phys. Rev.*, 156:487–493, Apr 1967b. doi: 10.1103/PhysRev.156.487. URL https://link.aps.org/doi/10.1103/PhysRev.156.487.

B. Oripov, T. Bieler, G. Ciovati, S. Calatroni, P. Dhakal, T. Junginger, O. B. Malyshev, G. Terenziani, A.-M. Valente-Feliciano, R. Valizadeh, S. Wilde, and S. M. Anlage. High-Frequency Nonlinear Response of Superconducting Cavity-Grade Nb Surfaces. *Phys. Rev. Applied*, 11:064030, Jun 2019. doi: 10.1103/PhysRevApplied.11.064030. URL https://link.aps.org/doi/10.1103/PhysRevApplied.11.064030.

R. J. Ormeno, M. A. Hein, T. L. Barraclough, A. Sibley, C. E. Gough, Z. Q. Mao, S. Nishizaki, and Y. Maeno. Electrodynamic response of Sr_2RuO_4. *Phys. Rev. B*, 74:092504, Sep 2006. doi: 10.1103/PhysRevB.74.092504. URL https://link.aps.org/doi/10.1103/PhysRevB.74.092504.

T. Oseroff and M. Liepe. Improvements to the Cornell sample host system. In *19th International Conference on Superconductivity*, Dresden, Germany, 2019.

T. Oseroff, M. Liepe, and Z. Sun. Sample Test Systems for Next-Gen SRF Sur-

faces. In *2021 International Conference on Superconductivity*, Grand Rapids, Michigan, 2021.

H. Padamsee. 50 years of success for SRF accelerators—a review. *Superconductor Science and Technology*, 30(5):053003, Apr 2017. doi: 10.1088/1361-6668/aa6376. URL https://doi.org/10.1088/1361-6668/aa6376.

H. Padamsee, J. Knobloch, and T. Hays. *RF Superconductivity for Accelerators*. Wiley, 2008. ISBN 9783527408429. URL https://books.google.com/books?id=OO1AAQAAIAAJ.

M. S. Pambianchi. *Microwave Surface Impedance Investigation of the Superconducting Proximity Effect in Superconductor/Normal-Metal Bilayer Structures*. PhD thesis, University of Maryland, 1995.

M. S. Pambianchi, J. Mao, and S. M. Anlage. Magnetic screening in proximity-coupled superconductor/normal-metal bilayers. *Phys. Rev. B*, 50:13659–13663, Nov 1994. doi: 10.1103/PhysRevB.50.13659. URL https://link.aps.org/doi/10.1103/PhysRevB.50.13659.

M. S. Pambianchi, S. N. Mao, and S. M. Anlage. Microwave surface impedance of proximity-coupled Nb/Al bilayer films. *Phys. Rev. B*, 52:4477–4480, Aug 1995. doi: 10.1103/PhysRevB.52.4477. URL https://link.aps.org/doi/10.1103/PhysRevB.52.4477.

M. S. Pambianchi, L. Chen, and S. M. Anlage. Complex conductivity of proximity-superconducting Nb/Cu bilayers. *Phys. Rev. B*, 54:3508–3513, Aug 1996. doi: 10.1103/PhysRevB.54.3508. URL https://link.aps.org/doi/10.1103/PhysRevB.54.3508.

A. B. Pippard. Experimental analysis of the electronic structure of metals. *Reports on Progress in Physics*, 23(1):176–266, Jan 1960. doi: 10.1088/0034-4885/23/1/304. URL https://doi.org/10.1088/0034-4885/23/1/304.

R. Porter. *Advancing The Maximum Accelerating Gradient Of Niobium-3 Tin Superconducting Radio frequency Accelerator Cavities: Measurements, Dynamic Temperature Mapping, And Material Growth*. PhD thesis, Cornell University, 2021.

S. Posen and D. L. Hall. Nb_3Sn superconducting radio frequency cavities: fabrication, results, properties, and prospects. *Superconductor Science and Technology*, 30(3):033004, Jan 2017. doi: 10.1088/1361-6668/30/3/033004. URL https://doi.org/10.1088/1361-6668/30/3/033004.

S. Posen, A. Romanenko, A. Grassellino, O. Melnychuk, and D. Sergatskov. Ultralow Surface Resistance via Vacuum Heat Treatment of Superconducting Radio-Frequency Cavities. *Phys. Rev. Applied*, 13:014024, Jan 2020. doi: 10.1103/PhysRevApplied.13.014024. URL https://link.aps.org/doi/10.1103/PhysRevApplied.13.014024.

S. Posen, J. Lee, D. N. Seidman, A. Romanenko, B. Tennis, O. S. Melnychuk, and D. A. Sergatskov. Advances in Nb_3Sn superconducting radio frequency cavities towards first practical accelerator applications. *Superconductor Science and Technology*, 34(2):025007, Jan 2021. doi: 10.1088/1361-6668/abc7f7. URL https://doi.org/10.1088/1361-6668/abc7f7.

D. Pozar. *Microwave Engineering*. Addison-Wesley series in electrical and computer engineering. Addison-Wesley, 1990. ISBN 9780201504187. URL https://books.google.com/books?id=0XLFQgAACAAJ.

G. D. L. Semione, A. D. Pandey, S. Tober, J. Pfrommer, A. Poulain, J. Drnec,

216

G. Schütz, T. F. Keller, H. Noei, V. Vonk, B. Foster, and A. Stierle. Niobium near-surface composition during nitrogen infusion relevant for superconducting radio-frequency cavities. *Phys. Rev. Accel. Beams*, 22:103102, Oct 2019. doi: 10.1103/PhysRevAccelBeams.22.103102. URL https://link.aps.org/doi/10.1103/PhysRevAccelBeams.22.103102.

A. Sheikhzada and A. Gurevich. Dynamic transition of vortices into phase slips and generation of vortex-antivortex pairs in thin film Josephson junctions under dc and ac currents. *Phys. Rev. B*, 95:214507, Jun 2017. doi: 10.1103/PhysRevB.95.214507. URL https://link.aps.org/doi/10.1103/PhysRevB.95.214507.

Z. Sun, Z. Baraissov, C. A. Duke, T. Oseroff, D. K. Dare, D. A. Muller, and M. U. Liepe. Surface oxides and impurities on Nb and Nb_3Sn: a detailed XPS and STEM/EELS study (in preparation), 2022.

T. Tai. *Measuring Electromagnetic Properties of Superconductors in High and Localized RF Magnetic Field*. PhD thesis, University of Maryland, 2013.

M. Tinkham. *Introduction to Superconductivity*. Dover Books on Physics Series. Dover Publications, 2004. ISBN 9780486134727. URL https://books.google.com/books?id=VpUk3NfwDIkC.

J. P. Turneaure, J. Halbritter, and H. A. Schwettman. The surface impedance of superconductors and normal conductors: The Mattis-Bardeen theory. *Journal of Superconductivity*, 4(5):341–355, Oct 1991. ISSN 1572-9605. doi: 10.1007/BF00618215. URL https://doi.org/10.1007/BF00618215.

K. D. Usadel. Generalized Diffusion Equation for Superconducting Alloys.

Phys. Rev. Lett., 25:507–509, Aug 1970. doi: 10.1103/PhysRevLett.25.507. URL
https://link.aps.org/doi/10.1103/PhysRevLett.25.507.

A.-M. Valente-Feliciano. Superconducting RF materials other than bulk nio-
bium: a review. *Superconductor Science and Technology*, 29(11):113002, Sep
2016. doi: 10.1088/0953-2048/29/11/113002. URL https://doi.org/10.
1088/0953-2048/29/11/113002.

A.-M. Valente-Feliciano, C. Antoine, S. Anlage, G. Ciovati, J. Delayen, F. Gerigk,
A. Gurevich, T. Junginger, S. Keckert, G. Keppe, J. Knobloch, T. Kubo,
O. Kugeler, D. Manos, C. Pira, T. Proslier, U. Pudasaini, C. E. Reece, R. A.
Rimmer, G. J. Rosaz, T. Saeki, R. Vaglio, R. Valizadeh, H. Vennekate, W. V.
Delsolaro, M. Vogel, P. B. Welander, and M. Wenskat. Next-Generation Super-
conducting Technology based on Advanced Thin Film Technologies and In-
novative Materials for Accelerator Enhanced Performance and Energy Reach,
2022. URL https://arxiv.org/abs/2204.02536.

N. Valles. *Pushing the Frontiers of Superconducting Radio Frequency Science: From
the Temperature Dependence of the Superheating Field of Niobium to Higher-order
Mode Damping in Very High Quality Factor Accelerating Structures*. PhD thesis,
Cornell University, 2014.

P. J. Walsh and V. P. Tomaselli. Theory of microwave surface impedance in su-
perconductors and normal metals. *American Journal of Physics*, 58(7):644–650,
1990. doi: 10.1119/1.16425. URL https://doi.org/10.1119/1.16425.

B. Xiao, C. Reece, and M. Kelley. Superconducting surface impedance
under radiofrequency field. *Physica C: Superconductivity*, 490:26–31,
2013. ISSN 0921-4534. doi: https://doi.org/10.1016/j.physc.2013.04.

003. URL https://www.sciencedirect.com/science/article/pii/S0921453413001718.

Y. Xie. *Development of Superconducting RF Sample Host Cavities and Study of Pit-Induced Cavity Quench*. PhD thesis, Cornell University, 2012.

S. Zhao, D. J. Goldie, S. Withington, and C. N. Thomas. Exploring the performance of thin-film superconducting multilayers as kinetic inductance detectors for low-frequency detection. *Superconductor Science and Technology*, 31(1):015007, Nov 2017. doi: 10.1088/1361-6668/aa94b7. URL https://doi.org/10.1088/1361-6668/aa94b7.

W. Zimmermann, E. Brandt, M. Bauer, E. Seider, and L. Genzel. Optical conductivity of BCS superconductors with arbitrary purity. *Physica C: Superconductivity*, 183(1):99–104, 1991. ISSN 0921-4534. doi: https://doi.org/10.1016/0921-4534(91)90771-P. URL https://www.sciencedirect.com/science/article/pii/092145349190771P.